NTNU

Norwegian University of
Science and Technology

Estimation of Design Snow Loads on Offshore Structures in the Barents Sea

Bjørnar Berge Lie

MSc in Physics
Submission date: May 2016
Supervisor: Jon Andreas Støvneng, IFY
Co-supervisor: Sigurd Teigen, Statoil

Norwegian University of Science and Technology
Department of Physics

Abstract

Snow accumulating on offshore structures can reduce freeboard and stability, block equipment and valves, and reduce operability of the platform or ship. It is thus important to evaluate snow conditions before starting long term operations. However, offshore snow condtitions in the Barents Sea are largely unquantified.

The present study investigates snow loads on offshore structures in the Barents Sea. We have implemented a model to establish time series of snow loads using a 10-day snowfall model or an energy balance model, with or without snow transport by wind. Methods to estimate extreme value statistics have also been applied, specifically using the generalized extreme value distribution and the peak-over-threshold method. These models have been applied with meteorological data from NORA10 hindcast grid points covering the entire Barents Sea to provide estimates of extreme snow loads. The results for a 10-day snowfall model without drift show 100-year return levels of snow load to be 70 kg/m^2 (0.68 kPa) to 120 kg/m^2 (1.18 kPa) in the area opened to petroleum activity in the Norwegian sector of the Barents Sea. Indication of a declining trend in the extreme values has also been found in the southern Barents Sea. The hindcast archive NORA10 was validated against observations to evaluate uncertainties in the hindcast. NORA10 shows a wet bias at all locations, but the distribution of extreme precipitation is similar to the observations. Due to undercatch of snow in the observations, it is likely that NORA10 underestimates extreme precipitation.

Samandrag

Snø som samlar seg på strukturar til havs kan redusere tilgjengeleg lastekapasitet og stabilitet, hindre tilkomst og handtering av operasjonelt utstyr og senke produktiviteten til skipet eller platforma. Det er derfor viktig å undersøke snøforhald i eit område før konstruksjonar blir sett i langvarig drift. Trass i dette, er snølaster i Barentshavet lite studert i den opne litteraturen.

Denne studien granskar snølaster på konstruksjoner offshore i Barentshavet. Vi har implementert metodar for å rekne ut tidsseriar for snølast ved bruk av enten 10-dagars snøsum eller ein energibalasemodell. Ein modell for snødrev har òg blitt implementert. Vi har brukt to statistiske metodar for å estimere ekstreme snølaster, nærare bestemt Generalized extreme value (GEV) distribusjon og peak-over-threshold metoden. Desse metodane har blitt brukt med hindcast-data frå NORA10 til å rekne ut ekstreme snølaster i heile Barentshavet. Resultata viser at for ein 10-dagars snøsum utan snødrev er returnverdien for 100-års gjenntaksinterval mellom 70 kg/m^2 (0.68 kPa) til 120 kg/m^2 (1.18 kPa) i området som er opna for petroleumsaktivitet i den norske sektoren av Barentshavet. Det vart også funne indikasjon på ein minkande

trend for ekstreme snølastar i den sørlege delen av Barentshavet. NORA10 vart også samanlikna med meteorologiske observasjonar for å evaluere uvissa i hindcast-dataa. NORA10 har fleire dagar med nedbør enn observert, men distribusjonen til ekstrem nedbør er liknande i dei to datasetta. Grunna oppfangningssvikt av nedbør, og spesielt av nedbør som snø, er det likevel truleg at NORA10 underestimerer ekstrem nedbør.

Table of Contents

List of Tables

List of Figures

Symbols

Symbol	Variable	Dimension
ϵ_m	Emissivity of the sky	-
ϵ_s	Emissivity of snow	-
c	Cloud cover fraction	-
$c_{p,air}$	Specific heat capacity of air	J kg^{-1} K^{-1}
c_H, c_E	Exchange coefficient for turbulent and evaporative heat flux	-
$e(T)$	Water vapour pressure	Pa
f_d	Number of time steps in 24 hours	-
h	Hour of the day	hour
L	Length of fetch for wind drift	m
l_f	latent heat of fusion of water	J kg^{-1}
M	Rate of melting of the snow pack	kg m^{-2} s^{-1}
Ψ	Net sky transmissivity	–
p	Air pressure at the surface	Pa
Q	Net heat flux to the snow surface	J m^{-2} s^{-1}
$q(T)$	Specific humidity	kg kg^{-1}
ρ_a	Density of air	kg m^{-3}
S_a	Total solar irradiance at top of the atmosphere	W m^{-2}
S^i	Snow load in time step i	kg m^{-2}
R^i	Precipitation during time step i	mm. water equivalent
T_a	Air temperature at 2 m	°C
T_s	Temperatire of the snow surface	°C
T_t	Threshold temperature for precipitation falling as snow	°C
Tr	Snow transport rate by drift	kg m^{-1} s^{-1}
U_{10}	Wind speed at 10 m	m s^{-1}
θ_S	Solar zenith angle	rad
δ	Solar declination angle	rad
ϕ	Local latitude	rad
ϕ_T	Latitude of the tropic of cancer	rad
τ	Hour angle	rad

1 Introduction

According to the U.S. Geological Survey (Gautier et al., 2009), areas north of the Arctic Circle account for 13 percent of undiscovered oil resources and 30 percent of undiscovered natural gas, most of this offshore. On the Norwegian Continental shelf, the Norwegian Petroleum Directorate estimates that the Barents Sea contains 48 % of the country's undiscovered petroleum resources. In the newly opened area Barents South-East alone, there are estimated undiscovered resources of 300 million Sm^3 oil equivalent (P50 estimate) (NPD, 2016). Even though moving petroleum activity further north can potentially give access to large resources it also introduces different challenges compared to exploration and production of hydrocarbons at lower latitudes. Colder climate, icebergs and sea ice, are only some among many new challenges. Of the new challenges, the present study will focus on extreme snow loads on offshore structures in the Barents Sea.

The Barents Sea has been open to petroleum activities since 1979, with the first well drilled in 1980. Since then, only two fields have been developed and started production (Snøhvit and Goliat). The next possible field development is Johan Castberg, which is located 150 km from Goliat and nearly 240 km from mainland Norway. Before starting field development, it is important to investigate the meteorological conditions in the area. However, there is less available data for the Barents Sea than further south. Syversen et al. (2015) investigated knowledge gaps of meteorological conditions in the Barents sea, and found that heavy snowfall and snow accumulation offshore was a poorly understood problem which needed further investigations.

Snow accumulating on a structure will add weight and reduce the freeboard of floating platforms (Ryerson, 2011). In most cases, the load will shift the center of mass upward and can reduce the stability of the structure. On a semi-submersible like the Transocean Barents drilling rig, with a deck area of 120 m by 80 m, a 0.3 m deep snow cover with density 100 kg/m^3 will add 290 ton of extra weight. Heavy snowfall can also interrupt helicopter transport by reducing visibility and can affect evacuation (Syversen et al., 2015). Dry snow will not stick well to any vertical surfaces. However, wet snow, freezing rain, and water droplets in fog can stick to a surface, freeze and accumulate as ice, efficiently blocking equipment and valves, reducing operability of the platform or ship and adding weight. This ice accreted from fresh water sources is called atmospheric icing.

When designing ships or platforms for cold climate regions it is thus necessary to estimate the extra loads and dangers from snow and ice. This is a requirement in

the international standard for Arctic offshore structures (ISO 19906, 2010). However, there are few available studies on snow in an offshore environment. Most of earlier efforts on atmospheric icing and snow loads have focused on land applications, like power lines (Makkonen, 1989; Nygaard et al., 2014; Makkonen, 2000) and rooftops. Some work has been done on marine icing (Overland et al., 1986; Kulyakhtin, 2014; Hansen and Teigen, 2015), but extreme snow loads offshore are largely unknown. The current NORSOK N-003 (2007) standards[1] simply recommends a characteristic snow load of 0.5 kPa ($\approx$ 50 kg/m^2) for snow loads on the entire Norwegian continental shelf, unless more detailed meteorological information is available. The standard is under revision, and new recommendations for the Barents Sea will possibly be to use a 7-day snowfall sum to estimate snow loads (Eik, 2016, Personal communication).

A structure should be designed not only to withstand daily environmental actions, but also extremes which can occur during its lifetime. According to regulations, characteristic environmental actions on offshore structures are defined by annual exceedance probabilities of 10^{-2} and 10^{-4} (NORSOK N-003, 2007), which roughly translates to loads which can be expected to occur every 100 and 10 000 years. To determine the characteristic actions, extreme value statistics has to be used, preferably by the use of different statistical methods to evaluate the sensitivity of the result. Classical extreme value theory assumes temporal stationarity of the process under study, i.e. the model parameters do not change over time. This might not be a valid assumption for climatic time series which often are non-stationary (Cooley, 2009; Katz, 2010). An approach to solve this problem is to use time as a covariate in classical extreme theory to model the temporal change of parameters leading to non-stationary extreme value theory (Coles, 2001, Ch. 6). This allows us to estimate time evolution of extremes within the extreme value theory. The approach has been used for climate data such as wind speed (Hundecha et al., 2008), and precipitation (Beguería et al., 2011), however to the authors' knowledge, only one study has used the method on snow (Marty and Blanchet, 2012).

One of the largest difficulties encountered when trying to estimate snow and ice loads is to obtain accurate meteorological data (Makkonen, 2000). Even for simple snow load calculations, accurate precipitation and temperature time series are necessary. The density of weather stations is also very low in the Arctic, and mostly limited to coastal areas or islands, like Bjørnøya and Hopen in the Barents Sea. A possibility is to use output from hindcast archives or reanalysis data like the Norwegian Reanalysis Archive (NORA10) hindcast (Reistad et al., 2011) or ERA-interim reanalysis (Dee et al., 2011). Output from these models are widely used in studies of observed variability in the Arctic atmospheric circulation (Serreze and Barry, 2005). These models estimate the state of the atmosphere as well as various fluxes, like precipitation, radiation, and evaporation, through assimilation of observations. The simulated atmospheric state might differ from the true state due to difficulties in determining the true initial- and boundary conditions and through limitations in the model physics, resolution, and parameterizations. Studies have found good agreement between NORA10 wind fields and observations, with a root-mean-square value of 2.46 m/s and negligi-

[1]The Norsok standards are developed by the Norwegian petroleum industry to ensure adequate safety, value adding and cost effectiveness for petroleum industry developments and operations.

ble bias (Reistad et al., 2011), but uncertainties in precipitation from the hindcast is not very well understood and needs to be investigated further (Syversen et al., 2015).

The present study is investigating snow loads on offshore structures in the Barents Sea. The scope is limited to characteristic snow load and a simple model of wind drift is also applied. Atmospheric and marine icing is not covered in the present study. The aim of the study is to characterize extreme snow conditions in the Barents Sea. This has been done in four steps. First, we investigated precipitation in the NORA10 hindcast, and compared it with observed precipitation to validate the accuracy of the hindcast. Then we studied the duration of snow events and the properties of the x-day snowfall model to select a proper number of accumulation days. Next, a case study of snow load on a helicopter deck was carried out. The goal of the case study is to present the statistical methods, and compare the two extreme value distributions used in the present study. Also the effects of wind drift on the extreme snow loads are investigated. The methods introduced in the case study are also applied on a basin wide grid to estimate extreme snow loads in the Barents Sea.

2 Data

The data applied in this study consist of atmospheric hindcast data from NORA10 and meteorological observations from the Norwegian Meteorological Institute. The variables used were air temperature 2 m above the surface, wind speed at 10 m above the surface, relative humidity and precipitation. The energy balance melt model also uses the cloud cover fraction.

2.1 NORA10 Hindcast

Due to the relative sparseness of observational meteorological data in the Arctic, hindcast data is an attractive source of information and has been used in many studies, e.g. Hamilton et al. (2015); Teigen et al. (2015); Sagerup (2015); Syversen et al. (2015). NORA10 (Reistad et al., 2011) is a dynamic downscaling of the reanalysis ERA-40 (Dee et al., 2011) using the numerical weather prediction model HIRLAM and is produced by MET Norway. The hindcast covers the areas of the North Sea, Norwegian Sea and the Barents Sea. The spatial resolution is around 10 km with data for every 3 hour interval starting from September 1, 1957 and it is continuously being updated. In the present study, the period of NORA10 data studied is from September 1, 1957 to June 30, 2015. If not otherwise noted, this is the period of interest. In the comparison with observations, four blocks of 3 hour intervals in the NORA10 data were grouped together to match the 12 hour resolution of the observations. A year is defined to start on July 1. A yearly maximum is then the maximum value between July 1 and June 30, 365 days later. A winter is defined as the half year between November 1st and May 1st.

In the present study two specific locations will be used for a case study, and to provide examples during the discussion. The two locations are the position of the oil field Johan Castberg and a grid point in the southeastern Barents Sea (see Figure 2.1). Johan Castberg is an oil discovery in the Barents Sea at 72.49° N, 20.33° E, which has not been developed yet, but contains large volumes of proven hydrocarbon reserves. Currently, a ship shaped floating production storage and offloading (FPSO) concept is considered. The decision to start further development is expected to be taken fall 2016. The southeastern Barents Sea is a newly opened part of the Barents Sea to petroleum activity. Multiple sectors of this area are promising for oil and gas discoveries. One of these sectors was chosen for this study and a NORA10 grid point in the middle of

the sector was selected. The grid point is at the location 73.99° N and 35.62° E. This gridpoint will be called Barents South-East in further discussions.

2.2 Observations

For a validation of the NORA10 model data, we used observations from the weather stations on Hopen, Bjørnøya and Fruholmen, operated by the Norwegian Meteorological Institute (eKlima (2016)). See Table 2.1 for information on the stations, and Fig. 2.1 for a map of the area. 12 hour accumulated precipitation and 24 hour accumulated precipitation were available and covered the whole period of interest except for Fruholmen, where the precipitation measurements ended in 2003, and thus for this station we used the period 1957 to 2003. It was found that the 12-hour precipitation had the least amount of missing data points for the period of interest, and hence this was used for validation of NORA10.

Bjørnøya is located approximately at the midpoint between mainland Norway and Spitsbergen. The meteorological station at Bjørnøya is placed on the northern side of the island and has not been moved since July 1947 (Steffensen et al., 1996). The surrounding area has sparse vegetation and no trees. The tallest mountain on Bjørnøya is 535 m, but the surrounding hills around the station are less than 90 m. Strong winds, often in combination with drifting snow makes precipitation measurements difficult. The precipitation gauge was moved 82 m to the east in June 1969 and this may have caused non-homogeneity in the data series, but no significant difference between the distribution of precipitation before and after the move was found.

The island of Hopen is located 220 km to the southeast of Spitsbergen. The weather station is at the east side of the island, around 7 km from the south edge. The island is surrounded by sea ice on average around 9 months of the year (Steffensen et al., 1996), although because of retreating sea ice, this number is probably less today. To the northeast and southwest there are mountains up to 300 m in altitude close to the station, which affects the wind measurements (Steffensen et al., 1996). The station has not moved since 1945, but several buildings have been built and removed, which can have affected the homogeneity of the precipitation measurements. Based on station reports, blowing snow was a large problem before 1997. To reduce the problem, the precipitation gauge was moved (Hanssen-Bauer, 2016, Personal communication). This has created an inhomogeneity in 1997, and the precipitation measurements are significantly smaller after it moved.

Fruholmen Fyr has precipitation observations between June 1954 and April 2005. The station is located on a small island off the coast of northern Norway. The station has not been moved during the period (Johnsen, 2016, Personal communication). In 1955 and 1956 there are reported several events with sea spray from waves reaching the precipitation gauge, which has increased the observed precipitation. This is possibly also a problem in later years, but it is not mentioned later (eKlima, 2016)

Observations from the stations on Bjørnøya and Hopen were used to validate NORA10 because of the locations in the middle of the western part of the Barents Sea. Bjørnøya is also close to the area opened for petroleum activity and the data

should be somewhat representative for the conditions at sea. The location of Fruholmen Fyr is close to the LNG terminal on Melkøya and the surrounding sea will see increasing activity with further development of fields in the Barents Sea.

Table 2.1: Meteorological stations used for validation

Station name	Station Number	Altitude	Location
Hopen	99720	6 m	76.51° N 25.01° E
Bjørnøya	99710	16 m	74.52° N 19.01° E
Fruholmen Fyr	94500	13 m	71.09° N 23.98° E

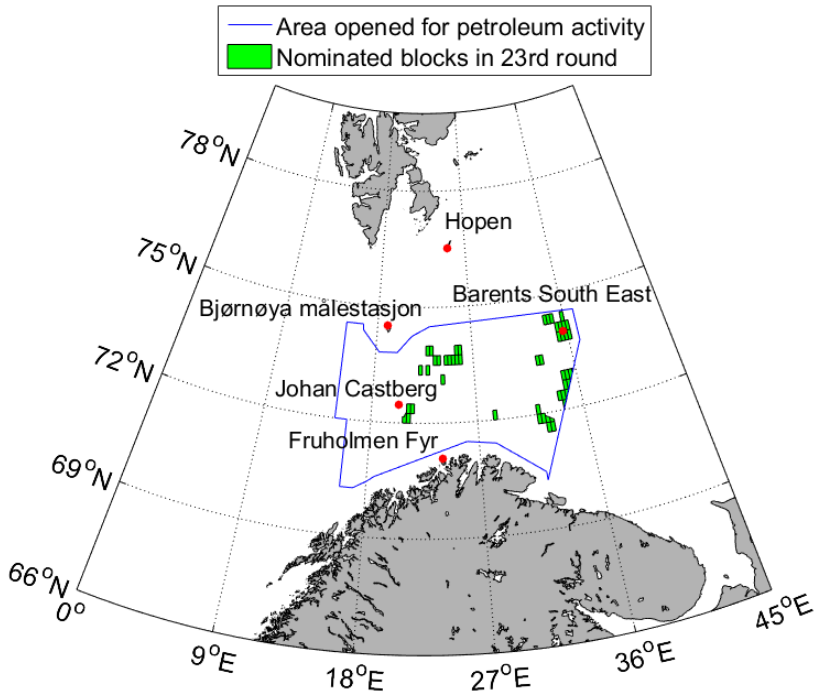

Figure 2.1: A map showing the location of Hopen, Bjørnøya, Johan Castberg, Barents South East and Fruholmen Fyr. The southern part of Svalbard can be seen in the top of the map while the Cap of the North (northern Norway, Sweden, Finland and the Kola peninsula) shown in the bottom.

3 Theory and Method

3.1 Physical oceanography and meteorology of the Barents Sea

The large scale air currents over the northern Atlantic Ocean is driven by a low pressure area over Iceland and a high pressure area over Greenland. The prevailing winds are westerly or southwesterly, bringing warm air masses towards the Svalbard area (Førland et al., 1997). During winter, the region around Iceland extending into the Barents Sea is a region of frequent cyclogenesis (Serreze and Barry, 2005), with a main storm track going northeast of Iceland and into the Barents Sea. On average, four to six cyclones per month are observed in the Norwegian-Barents-Kara sea (Førland et al., 1997). Further north the prevailing winds are easterly and northeasterly bringing cold air masses into the area. Variation between the extension of the two air masses originating from southwest and northeast causes great fluctuations in winter conditions.

Polar lows are also common in the Barents Sea, especially in the western part. On average, 12 to 15 polar lows are observed in the Barents Sea annually (Syversen et al., 2015). Polar lows are small, intense maritime mesocyclones, typically with a diameter of 100 km to 500 km (Serreze and Barry, 2005). During a polar low, high wind speed can develop rapidly, and is often followed by high precipitation rates. Polar lows mainly develop when cold air from the ice edge flows over warmer waters leading to convection and instability of the air masses.

The Barents Sea is a shelf sea with a relativity shallow depth of less than 300 m, except for a few areas with deeper waters. The sea is constricted by Svalbard and Franz Josef land to the north, Novaya Zemlya to the east, the Kola peninsula in the south and the shelf edge towards the Norwegian Sea in the west. In addition to the economical importance, the Barents sea plays an important role in the Arctic climate system and is closely linked to large air-ice-ocean variability in the area (Smedsrud et al., 2013).

The water in the Barents sea includes three principle water masses (Loeng, 1991)

- Warm, salty Atlantic waters
- Cold, less saline Arctic waters

- Warm, less saline coastal waters

The northward flowing Norwegian Atlantic Current splits at around 70° N, with one branch following northward towards Svalbard and eventually ending in the Arctic Ocean, while the other branch flowing into the Barents Sea, bringing warm (3.5 to 6.5 °C) and high salinity (>35.0) water into the shelf sea (Loeng, 1991; Maslowski et al., 2004). The influx of Arctic water comes from the area between Svalbard and Novaya Zemlya and flows southward in the Barents Sea. One part flows along the eastern slope of Spitsbergenbanken all the way down to Bjørnøya. Its interaction with the Atlantic water marks the Arctic Polar Front. The warm Atlantic water is responsible for high temperature gradients between the water temperature and air temperature, which is a driving mechanism in creating polar lows.

The north of the Barents Sea is mostly covered by sea ice, while sea ice intrusion in the southern part is a rare event. The annual extent is highly variable, with a mean minimum extent in the Barents sea at around 80° N and a mean maximum extent at around 75° N (Turner et al., 2013). The sea ice largely influences the air temperatures, and thus also precipitation type, leading to large variability because of varying position of the ice edge.

Figure 3.1 shows mean annual precipitation and mean temperatures estimated from NORA10. The annual total precipitation has a northeasterly gradient with the highest values off the coast of northern Norway and the lowest values on the east coast of Svalbard. The annual precipitation in the Barents Sea is 700 mm/year to 1000 mm/year, which is somewhat higher that the annual precipitation reported in Serreze and Barry (2005). They analyzed precipitation data from multiple sources to produce a contour map of annual precipitation in the Arctic and found the value for the Barents Sea to around 600 mm/year. North of 75° N, the mean temperatures are under 0 °C. In the very eastern parts of the Barenets Sea, the mean temperatures are under 0 °C all the way to the Russian coastline.

3.2 Snow model

All snow loads in the present study are given in units kg/m^2. In the literature, snow loads on structures are often given in kPa ($\approx$ 0.01 kg/m^2). We have chosen to use kg/m^2 because of the direct connection to total snow loads on a structure, however it is trivial to convert between the different units.

Accumulation of snow

Since precipitation type is not included in the data used, a method to distinguish when the precipitation falls as snow or rain is needed. This is a difficult problem, with the type of precipitation changing with varying and interacting environmental conditions in a storm (Thériault et al., 2006). NORA10 has data for temperature and humidity at different altitude levels, but we choose to simplify to only consider the temperature 2 m above ground.

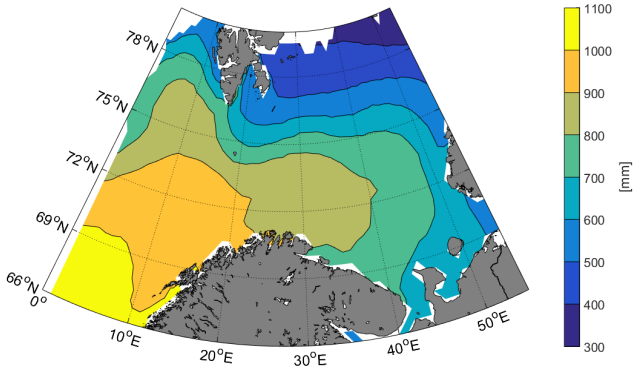

(a) Mean yearly accumulated precipitation (mm water equivalent).

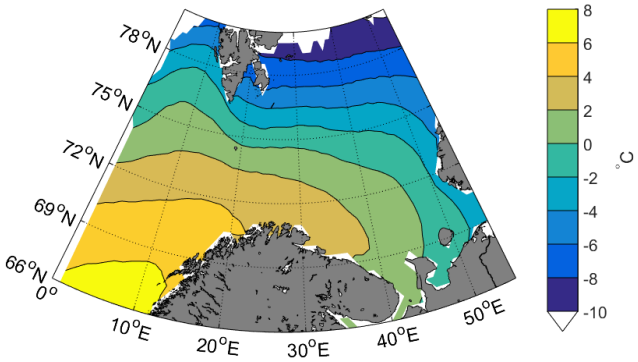

(b) Mean temperature

Figure 3.1: Mean yearly precipitation (**a**) in the Barents Sea and mean temperatures (**b**) from 1957 to 2015. Data from NORA10.

Matsuo et al. (1981) analyzed precipitation type for different meteorological conditions at three locations in Japan. They found a strong relationship between precipitation type and both relative humidity and temperature at ground level, but with some deviation between the stations. In the limited dataset the temperature threshold for which only rain was observed varied from 2.0 °C to 3.3 °C depending on the location and humidity. The threshold temperature where only snow was observed varied from 0.1 °C to 3.0 °C at the different locations. In between these thresholds the precipitation fell sometimes as snow and sometimes as rain. The overlap of the two intervals is due to different locations observing different tresholds. E.g., one location only observed snow under 0.1 °C and rain over 2.0 °C, while another location only observed snow under 3.0 °C and rain over 3.3 °C.

The data from Matsuo et al. (1981) provides evidence for precipitation falling as snow is dependent on humidity, but it is uncertain how the data relates to other climatological regimes. Because of this, a simple model which neglects dependence on humidity is chosen in the present study. All precipitation that falls when the 2 m

air temperature is lower than a threshold temperature will fall as snow. For higher temperatures the precipitation is assumed to be liquid.

In the Norwegian Arctic, Førland and Hanssen-Bauer (2002) found that the type of precipitation as a function of temperature varied for the different station in the study (Bjørnøya, Svalbard Airport, Longyearbyen, Ny-Ålesund and Jan Mayen). For air temperatures between 1 °C to 1.9 °C at Bjørnøya, the precipitation fell as sleet or snow 19 % of the time. When the temperatures were above 2 °C, the precipitation fell as snow and sleet in less than 2.5 % of the time. At the Spitsbergen stations, the fraction of solid precipitation is in general higher than at Bjørnøya, but the latter station is belived to better represent the offshore conditions in the Barents Sea.

Based on the data from Matsuo et al. (1981) and Førland and Hanssen-Bauer (2002), a threshold temperature of $T_t = 1.5$ °C is used, so all precipitation that falls when the temperature is below 1.5 °C accumulates as snow. This is a conservative choice as the fraction of solid precipitation is less than 1 at this temperature. Precipitation from rain is ignored in the model. Rain falling on snow can increase the melting of the snow-pack, but it can also increase the loads by filling pores in the snow and increasing the density of the snow pack. These effects are however not considered in the present study.

A melt model is then used to remove the snow. The melt model can range from the very simple, like a x-day snowfall model, to a complex energy balance model requiring many meteorological parameters as input.

3.2.1 x-day snowfall model

In the x-day snowfall model, the snow load is just the sum of snow accumulation the last x days. That is, snow falling on a certain day will stay on the ground for x days, then it will be removed. The model is very simple and the only parameters needed are temperature and precipitation.

For applications like snow loads on roofs and avalanche studies, heavy snow loads within a few days is of more interest than accumulating snow over a longer period and the x-day snowfall model is often chosen (Changnon and Changnon, 2007; Marty and Blanchet, 2012). The model has also been used in various studies offshore. When developing recommended snow loads in NORSOK N-003 (2007) a 2-day accumulation period was used. The NORSOK standard is currently in revision and it is considered to use different accumulation periods for different latitudes, using a week long accumulation period in the Barents Sea (Eik, 2016, Personal communication). The snow load from the model can be viewed as an operational snow load where we assume an offshore facility has access to snow removing equipment and will actively remove snow once weather conditions permit working on deck.

There is currently no standard choice of number of accumulation days, and it is often chosen arbitrarily or using vague arguments. Changnon and Changnon (2007) use 2-day snowfall to study heavy snowfall storms in the United States, and argues that snow from 2-day snowstorms are the cause of 70 % of all total snowfall in the United States. It is uncertain if this is also the case in an offshore environment in general and the Barents Sea in particular. On a large offshore structure it might not

be feasible to remove all the snow within two storm events. Another concern is the accuracy of the input data to the model. Hindcast data is the most common way to investigate snow loads in the Barents Sea because of the sparse observations. Reistad et al. (2011) showed that NORA10 can predict the wind field fairly reliably, however, the precipitation rate is not as accurate. With a too short accumulation period there is a risk that uncertainties in the hindcast dominates our results, and the total snow loads are underestimated or overestimated. The x-day snowfall model and choice of number of accumulation days are studied in detail in Chapter 4.2. Based on this a 10-day accumulation period is used in the rest of the present study.

3.2.2 Energy balance melt model

The net energy flux Q to the top layer of the snow pack can be written as

$$Q = Q_{sh} + Q_{lo} + Q_{se} + Q_{la} + Q_c, \tag{3.1}$$

where the following notation has been introduced:

Q_{sh} Short wave radiation

Q_{lo} Long wave radiation

Q_{se} Sensible heat

Q_{la} Latent heat

Q_c Conductive heat through the snow

The snow will start melting if the energy flux to the snow surface is positive. Ignoring the heat capacity of the snow, melt rate M (kg m^{-2}s^{-1}), is

$$M = Q/l_f, \tag{3.2}$$

where l_f ($= 3.34 \times 10^5$ J/kg; Engineering Toolbox (2016)) is the latent heat of fusion. There is a number of different heat flux parameterizations available. In this thesis, the parameterization is based on the recommended parameterization for heat fluxes over the Arctic Ocean from Simonsen and Haugan (1996). Further, any conductive heat flux through the snow, which can originate from e.g. indoor heating, is neglected. Because snow has a low thermal conductivity, heat from a warm floor will be negligible for a thick snow pack.

Shortwave radiation

Shortwave radiation is solar insolation which penetrates the atmosphere and reaches the snow surface. The model for shortwave radiation is from Liston and Elder (2006) and it considers cloud cover fraction and diffuse and direct solar radiation. The model has been implemented assuming a horizontal surface, but it is straightforward to expand the model to consider surface topology as done in Liston and Elder (2006).

Incoming shortwave radiation striking the surface, Q_{sh} (W m^{-2}), is given by

$$Q_{sh} = S_a(\Psi_{dir} + \Psi_{dif})\cos(\theta_s). \tag{3.3}$$

Total solar irradiance at the top of the atmosphere normal to the solar beam is given by S_a (=1370 W m^{-2}; Kyle et al. (1985)). Ψ_{dir} and Ψ_{dif} are the direct and diffusive net sky transmissivities, respectively, while θ_s is the solar zenith angle which is

$$\cos(\theta_s) = \sin(\delta)\cos(\phi) + \cos(\delta)\cos(\phi)\cos(\tau).$$

Here δ is the solar declination angle, ϕ is the local latitude, and τ is the hour angle. The solar declination angle can be approximated by

$$\delta = \phi_T \cos\left(2\pi\frac{d - d_r}{d_y}\right),$$

where ϕ_T is the latitude of the tropic of cancer (23.5° N), d is the current day of the year, d_r is the day of the summer solstice, and d_y is the average number of days in a year. Further, the hour angle τ is calculated by

$$\tau = \pi\left(\frac{h}{12} - 1\right),$$

where h is the hour of the day.

The net sky transmissivities are given by

$$\Psi_{dir} = (0.6 - 0.2\cos(\theta_s))(1 - c),$$

for the direct transmissivity, and

$$\Psi_{dif} = (0.3 - 0.1\cos(\theta_s))c,$$

for the diffusive transmissivity, where c is the cloud cover fraction.

Net longwave radiation

Net longwave radiation is the sum of energy radiating from the earth due to its heat, and energy from infrared radiation to the earth from the atmosphere. We used the same parameterization of the net longwave radiation as Simonsen and Haugan (1996). The outward longwave radiation is simply calculated by Stefan-Boltzaman's law. The incoming longwave radiation from the sky will vary with attitude and atmospheric conditions (Liston and Elder, 2006). Any change in elevation is relatively small for a structure at sea, and can be neglected. Then, according to Simonsen and Haugan (1996), the emissivity e_m of the sky for polar conditions can be modeled as

$$\epsilon_m = 0.7829(1 + 00.2232c^{2.75}), \tag{3.4}$$

where c is the unitless cloud cover fraction. The net longwave radiation is then

$$Q_{lo} = \sigma(\epsilon_m(T_a + 273.15)^4 - \epsilon_s(T_s + 273.15)^4), \tag{3.5}$$

with σ as Stefan-Boltzmann's constant, ϵ_s ($= 0.95$;Liston and Elder (2006)) is the emissivity of snow and T_s and T_a is the snow surface and air temperature in Celsius. The snow surface temperature is assumed to be equal to the minimum of the air temperature and the melting point of snow.

Turbulent heat fluxes

Turbulent heat fluxes comes from transport of heat (sensible) and moisture (latent) due to convection. The turbulent heat fluxes are taken from Parkinson and Washington (1979). The sensible heat flux is defined by

$$Q_{se} = \rho_a c_{p,air} c_H U_{10}(T_a - T_s) \tag{3.6}$$

where ρ_a is the density of air, $c_{p,air}$ is the heat capacity of air, c_H is an exchange coefficient and U_{10} is the wind speed.

The latent heat flux can be computed as

$$Q_{la} = \rho_a L_w c_E U_{10}(q(T_a) - q(T_s)), \tag{3.7}$$

where L_w is the latent heat of sublimation (=2.8×10^6 J/kg) and c_E is the exchange coefficient for latent heat. $q(T)$ is the specific humidity over an ice surface and expressed as (Gill, 1982, Appendix 4)

$$q(T) = \frac{0.622e(T)}{p - 0.378e(T)} \tag{3.8}$$

and the function $e(T)$ is water vapor pressure. The symbol p represents the air pressure at the surface. We assume that the water vapor pressure at the snow surface is saturated. The vapor pressure in the air is calculated from relative humidity, $rh = e(T_a)/e_s(T_a)$, where rh is relative humidity and $e_s(T)$ is the saturated water vapor pressure which in air can be expressed as (Gill, 1982)

$$e_s(T_a) = 10\wedge\left[\frac{0.7859 + 0.03477T_a}{1.0 + 0.00412T_a} + 2\right] \tag{3.9}$$

The heat exchange coefficients can vary with wind speed and atmospheric conditions, but to find a relationship is not straightforward. For snow covered ice Maykut (1982) found a constant exchange coefficient of 1.75×10^{-3} for both the sensible and latent heat exchange coefficient, and this value is also used in the present study. Large and Pond (1982) estimated that both coefficients had a value around 1.1×10^{-3} for open water conditions. This value was later confirmed by experiments done by Smith et al. (1996) who did not find any dependence on wind speed in the range studied (5 to 22 m/s).

3.2.3 Snow drift

Snow transport by wind and subsequent redistribution of snow can significantly reduce the load on exposed parts of a structure while increasing the load on lee sides. In

the Barents Sea, events with snowfall and zero wind speeds are rare (Sagerup, 2015), and snow transport by wind can be significant. Snow drift is usually distinguished between snow grains being transported in creep, saltation or suspension mode (Lehning et al., 2008). Creep is classified as grains rolling over the surface and this mode has the smallest contribution to the mass flux of the three modes. Saltation takes place in the layer close the snow surface, usually within 5 m. In this mode, snow grains take on ballistic trajectories and crash into the surface where they either rebound with the surface or can eject more snow particles subjected to drift. This is the mode which contributes the most to the mass flux of the drifting snow. In the suspension mode the grains can be lifted high above the ground and drifted over many hundred meters before either sublimating or falling back to the ground.

Because the saltation process provides most of the mass flux during snow transport, many studies have tried to find empirical relations of transport rate based on measurements and observations (Budd et al., 1966; Takeuchi, 1980; Pomeroy and Gray, 1990; Tabler, 1994). Recently, methods using computational fluid dynamics (CFD) and numerical models have been developed to estimate drifting snow (Sundsbø, 1997; Lehning et al., 2008; Tominaga et al., 2011), which take into account aerodynamics, and microscopic processes like particle-bed collisions, particle motion and particle-wind feedback.

Threshold wind speed and driftable snow

Threshold wind speed for snow drift is defined as the minimum wind speed which can initiate or sustain snowdrift. The threshold wind speed is important in snowdrift as it defines the interval in which wind drift will occur (Li and Pomeroy, 1997).

Several investigators have studied the relation between threshold wind speed and physical properties of the snow cover (Budd et al., 1966; Pomeroy and Gray, 1990; Li and Pomeroy, 1997), and they agree that the snow cover resistance determining the threshold wind speed is related to particle bonding, cohesion and kinetic resistance to transport.

Snow particle bonding and snow pack density tends to increase with time. An important mechanism contributing to this is metamorphism which changes the structure of the snow over time. Metamorphism can be caused by a high temperature gradient in the snow pack. Due to the higher saturation vapor pressure in the warm part of the snow pack, water vapor can diffuse from this part to the cold part, where it condenses and grows crystals. Metamorphism also occurs in temperature uniform snow packs. This is due to higher water vapor pressure at a convex surface than a concave surface, and vapor will therefore move from convex parts of a snow crystal to concave surfaces of the crystal, leading to rounding and sintering of the crystal (Li and Pomeroy, 1997). The result from either type of metamorphism is generally densification of the snow surface and an increased number of bonds, which strengthens the surface over time. How fast this happens depends on the conditions, but DeGaetano and O'Rourke (2004) showed that most drifting events occur within one day after the last snowfall, and only an insignificant number of events occurred later than three days since the last snow fall.

Cohesive forces in snow is related to viscous forces in a thin liquid water film on the snow crystal surface under warm conditions (Li and Pomeroy, 1997). The cohesive forces increase with higher temperatures, but Nakaya and Matsumoto (1954) did an experiment confirming a liquid layer on the surface of ice crystals even at temperatures below $0\ ^\circ\mathrm{C}$. Hosler et al. (1957) showed a strong increase in cohesive forces with higher temperature, most likely caused by increased thickness of the thin liquid layer with temperature. Hosler et al. also showed a strong correlation between cohesion and water vapor pressure.

The physical processes which determine the snow surface's resistance to wind erosion are very complex, which makes modeling the threshold wind speed and snow transport on a completely physical basis very difficult. Field data have thus been necessary to make empirical estimates of the threshold value. Li and Pomeroy (1997) did a comprehensive study of the relation of the threshold wind speed to temperature and found that the threshold wind speed followed a cubic polynomial of temperature, however the variation in the observations was very large. The majority of the observed threshold wind speeds for dry snow were in the range 4 to 11 m/s, having an average of 7.7 m/s. Tabler (1994) suggests fluffy snow starts moving at 20 km/h (5.6 m/s), but usually snow ceases to blow for wind speeds lower than 24 km/h (6.7 m/s).

Based on physical consideration and data from Li and Pomeroy (1997) and DeGaetano and O'Rourke (2004), the snow is assumed to be unable to drift under the following conditions:

- After an air temperature increase above $0\ ^\circ\mathrm{C}$;
- During any time step when the wind speed is less than 4.5 m/s
- Any snow that is older than 3 days.

These assumptions are made to provide an upper boundary to the amount of snow drift. In Chapter 5.7, we evaluate the sensitivity of 100 year return levels of snow load to different temperature criterion, threshold wind speeds and snow free periods.

Transport rate

Several studies have tried to find empirical formulas connecting snow transport rate and wind speed and many of them give widely different results for the same wind speed. A selection of the formulas are shown in Table 3.1 and estimated snow transport is plotted in Figure 3.2

As seen in Figure 3.2 there is large disagreements between the models. Takeuchi (1980) attributes the large variations to different snow conditions and development of the snowdrift. Hence, as most empirical models use data from alpine or inland environments, or even from the Antarctic continent, it is uncertain which formula is most applicable in an offshore environment. Common for all models, though, is that transport rate is very sensitive to wind speed. In model 2 (Tabler, 1994), for example, doubling of the wind speed gives a 14-fold increase in transport rate. This means that the wind speed has to be accurately determined and that the height at which the wind speed is measured will have a significant impact on the result. If a wind speed

Table 3.1: Emperical formulas for snow transport by drift Tr (kg m^{-1} s^{-1}). Subscripts on Tr denotes the altitude interval for the snow transport. E.g. Tr_{0-5} is the total snow transport up to 5 m above the snow pack surface. The wind-speed is given in a height of 10 m.

$No.$	Study	Formula
1	Budd et al. (1966) [a]	$\log Tr_{0-300} = -5.7266 + 0.0887\,U_{10}$
2	Tabler (1994)	$Tr_{0-5} = U_{10}^{3.8}/233847$
3	Takeuchi (1980) [b]	
	a. For old firm snow	$Tr_{0-2} = 1.03 \cdot 10^{-4}(U_{10})^{2.7}$
	b. For settled dry snow	$Tr_{0-2} = 1.05 \cdot 10^{-6}(U_{10})^{4.16}$
4	Pomeroy and Gray (1990) [c]	$Tr_{sal} = \frac{U_{10}^{1.295}}{2118} - \frac{1}{17.37U_{10}^{1.295}}$

[a] Derived from equation for Tr with units [g/(m s)] to units [kg/(m s)]

[b] Derived from equation $Tr_{0-2} = 2 \cdot 10^{-4}U_1^{2.7}$ and $Tr_{0-2} = 2.9 \cdot 10^{-6}U_{10}^{4.16}$ assuming $z_0 = 0.246$ mm and $U_* = 0.0377U_{10}$, using a logarithmic wind profile

[c] Tr_{sal} is the snow transport of the entire saltation mode, excluding creep and suspension

measured at 2 m is used when the empirical formula was fitted to wind speeds at 10 m, the transport rate will be underestimated as usually the wind speed has a logarithmic profile with increasing speed with altitude.

The transport rate of blowing snow used in this study is taken from Tabler (1994) and is

$$Tr = \frac{U_{10}^{3.8}}{233847}. \tag{3.10}$$

This relationship has shown good agreement with observational data over multiple seasons (Tabler, 1991, 1994) which indicates that it is applicable for a range of meteorological conditions. It has also been successfully used in an independent study (DeGaetano and O'Rourke, 2004). Equation 3.10 assumes a fully developed wind field. In a field study, Takeuchi (1980) found that a 150 m to 300 m fetch is necessary to develop a saturated state. This implies a modification to Equation 3.10 is needed to account for a non-developed wind field for shorter structures. Following the method used in DeGaetano and O'Rourke (2004), a fetch of length 225 m was assumed to be necessary for a saturated state to develop. For fetches shorter than 225 m (typically the case for an offshore structure) an adjustment based on the square-root of the fetch was proposed,

$$Tr' = Tr\sqrt{\frac{L}{225}}, \tag{3.11}$$

where Tr' is the adjusted transport rate, L (m) is the length of the fetch, and Tr is the transport rate from Equation 3.10.

3.2.4 Numerical method to estimate time series of snow load

An algorithm to calculate time series of snow loads using the methods described was implemented. As input, meteorological data from NORA10 with observations every 3 hours were used. Flow charts of the algorithms are shown in Appendix A.

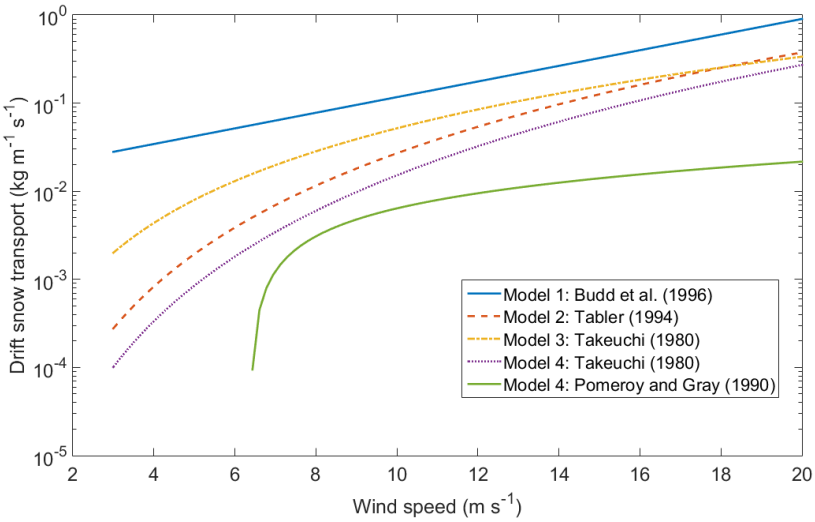

Figure 3.2: Empirical relationships of wind speed and drift snow transport according to the different models in Table 3.1

The algorithm can use either the energy balance model or the x-day snowfall model and with drift turned on or off. The implementation of the drift model has to be handled a little differently for the two melt models for reasons which will be discussed in the next section. The following notation and assumptions will be used when discussing the implementation

- At $t = 0$ there is no snow load
- x is the number of days in the x-day snowfall model
- Superscript indicates time step
- f_d is the number of time steps in 24 hours
- S^i is the snow load in time step i
- R^i is the accumulated precipitation during time step i
- T_t is the threshold temperature for precipitation falling as snow ($= 1.5$ °C)
- D^i is the amount of snow drift in time step i.

The snow load has units kg/m^2.

Implementation of x-day snowfall model

The first x days of the time series there is no melting, and the snow load in time step i is simply

$$S^i = \begin{cases} S^{i-1} + R^i \rho_w, & \text{for } T_a^i < T_t \\ S^{i-1}, & \text{otherwise} \end{cases}$$

After day x, the snow falling in the time step x days before the current time step has to be removed. That is, with xf_d as the number of time steps in x days, the snow load in time step i will be

$$S^i = \begin{cases} S^{i-1} + R^i \rho_w - R^{i-xf_d}, & \text{for } T_a^i < T_t \text{ and } T_a^{i-f_d x} < T_t \\ S^{i-1} + R^i \rho_w, & \text{for } T_a^i < T_t \text{ and } T_a^{i-f_d x} \geq T_t \\ S^{i-1} - R^{i-xf_d}, & \text{for } T_a^i \geq T_t \text{ and } T_a^{i-f_d x} < T_t \\ S^{i-1}, & \text{for } T_a^i \geq T_t \text{ and } T_a^{i-f_d x} \geq T_t \end{cases} \tag{3.12}$$

This means the algorithm adds any new snow that falls in the current time step, and removes the snow which fell in the time step x-days ago. It is implemented this way for efficiency. In every time step the program must at maximum do 6 comparisons and two additions. This is computationally cheaper than the alternative to sum up all the snow which fell the last x days, and makes it easier to implement drifting snow.

When adding the possibility of wind drift, there is a chance that the snow which fell x-days ago already drifted off, in which case the algorithm should not remove that snow. Hence, we need a check of how much of the snow which fell x-days ago drifted away. According to the assumptions, the snow can only drift during the first three days after it fell. Next, if the temperature is larger than $0\ ^\circ\mathrm{C}$ in a time step, the snow is 'locked off' and cannot drift any more. We also need to consider that new snow that falls on top of the old snow must be drifted away before the older snow can drift away. Then we can calculate s^k which is the amount of snow which fell in time step k and later drifted away[1]. The snow load in time step i can then be adjusted to

$$S^i = \begin{cases} S^{i-1} + R^i \rho_w - (R^{i-xf_d} - s^{i-xf_d}), & \text{for } T_a^i < T_t \text{ and } T_a^i < T_t \\ S^{i-1} + R^i \rho_w, & \text{for } T_a^i < T_t \text{ and } T_a^i \geq T_t \\ S^{i-1} - (R^{i-xf_d} - s^{i-xf_d}), & \text{for } T_a^i \geq T_t \text{ and } T_a^i < T_t \\ S^{i-1}, & \text{for } T_a^i \geq T_t \text{ and } T_a^i \geq T_t \end{cases} \tag{3.13}$$

Implementation of the energy balance model

To estimate the snow load in time step i, the algorithm has to calculate the energy fluxes in Equation 3.1. If all the net heat flux is positive the snow melt is calculated with 3.2, else it is set to zero. The snow load in time step i can then be computed as

[1] Not to be confused with D^k, which is the sum of snow drift in time step k.

$$S^i = \begin{cases} S^{i-1} + R^i\rho_w - M^i\Delta t, & \text{for } T_a^i < T_t \\ S^{i-1} - M^i\Delta t, & \text{otherwise} \end{cases},$$

where Δt is the number of seconds in the time step (1080 s for a 3 hour time step). Precipitation when the temperature is lower than $T_t = 1.5\ ^\circ\mathrm{C}$ falls as snow. If snow drift is turned on the algorithm will have to check how much snow is available to drift. This is decided based on the assumptions in Chapter 3.2.3. Then the snow transported off the platform can be estimated from Equation 3.11.

3.3 Statistical Modeling of Extreme Values

Generalized Extreme Value Model

The objective of extreme value analysis is to quantify the stochastic behavior of a process at unusually large - or small - levels (Coles, 2001). We will first look at a model focused on the statistical behavior of block maxima, that is

$$Z_n = \max\{X_1, ..., X_n\} \tag{3.14}$$

where $X_1, ..., X_n$ is a sequence of independent random variables having a common distribution F, which might be unknown. If n corresponds to the number of observations in a year, Z_n is the annual maximum. It can be shown that as $n \to \infty$ the probability that the block maxima is less than a value z is

$$\Pr\{Z_n \leq z\} \approx G(z) \tag{3.15}$$

where G is a member of the so called *generalized extreme value* (GEV) family of distributions,

$$G(z) = \exp\left\{-\left[1 + \xi\left(\frac{z-\mu}{\sigma}\right)\right]^{-1/\xi}\right\}, \tag{3.16}$$

defined on $\{z : 1+\xi(z-\mu)/\sigma > 0\}$, where $-\infty < \mu < \inf$ (location parameter), $\sigma > 0$ (scale parameter) and $-\infty < \xi < \infty$ (shape parameter). This family corresponds to a Fréchet or Weibull distribution for $\xi > 0$ and $\xi < 0$, respectively. The subset where $\xi = 0$ is interpreted as the limit of Equation 3.16 as $\xi \to 0$, leading to a Gumbel family distribution function.

This distribution can then be used to model the extremes of a series of independent observations $X_1, X_2, ...$ in the following way. We block the data into sequences of length n, and find the maxima of each block leading to a series of block maxima, $Z_{n,1}, Z_{n,2}...$, to which we can fit the GEV distribution. If we choose n to be the number of observations in a year, Z_n from Equation 3.15 would be the annual maxima, and we can find the annual maxima distribution by inverting Equation 3.16, yielding

$$z_p = \begin{cases} \mu - \frac{\sigma}{\xi}\left[1 - [-\ln(1-p)]^{-\xi}\right], & \text{for } \xi \neq 0 \\ \mu - \sigma\ln\{-\ln(1-p)\}, & \text{for } \xi = 0 \end{cases} \tag{3.17}$$

where $G(z_p) = 1 - p$. Hence the annual maximum has a probability p of exceeding the value z_p in any given year. In other words, z_p is the *return level* associated with the *return period* $1/p$. An interesting point is that if $\xi < 0$, the return level is bounded at $\mu - \sigma/\xi$ for $p \to 0$. If $\xi \geq 0$ the return level has no finite bound. A formal proof of the correctness of this distribution can be found in (Coles, 2001, Ch. 3).

To fit a dataset to the GEV distribution we can use maximum likelihood estimation. For $\xi \neq 0$, the log-likelihood for the GEV parameters is

$$l(\mu, \sigma, \xi) = -m \ln \sigma - (1 - 1/\xi) \sum_{i=1}^{m} \ln \left[1 + \xi \left(\frac{z_i - \mu}{\sigma} \right) \right] \times \sum_{i=1}^{m} \left[1 + \xi \left(\frac{z_i - \mu}{\sigma} \right) \right]^{-1/\xi} \tag{3.18}$$

Maximization of Equation 3.18 with respect to μ, σ, ξ leads to the maximum likelihood estimate with respect to the GEV family. There is no analytical solution, but it is easy to find an estimate numerically for any given dataset of z_i. If $\xi = 0$ we need to use the appropriate limit as $\xi \to 0$ of Equation 3.18, which will result in a Gumbel log-likelihood.

If the dataset available contains more data than the block maxima, this method is a wasteful method in the sense that many of the data points available are not used when doing inference on the return levels. E.g. in a particular year there may be several extreme snow events with higher snow loads than the maximum snow load in another year, but since the method only chooses the maxima in each block, the other extreme snow events in the block are thrown away.

In the derivation of the GEV model we assumed the observations $X_1, ..., X_n$ were a sequence of independent variables. This is however often not a valid assumption for physical data series. A time series of snow loads will definitely be dependent since the snow in time step i will contribute to the snow load in time step $i + 1$ unless the snow has completely melted. The annual maxima can however often be assumed to be independent; the maximum snow load in a particular winter is independent of the maximum snow load in the preceding winter. It can then be shown that even if the individual observations X_i are dependent, $Z_{n,m}$ will follow a GEV distribution as long as the block maxima, $Z_{n,m}$, are independent (see (Coles, 2001, Ch. 5)). This implies that dependence in data can often be ignored, as far as the modeling of block maxima is concerned, given that the dependence only spans a short time scale compared to the length of a block. This significantly strengthens the case for using the GEV family as a model for annual maxima.

Threshold model

Modeling of block maxima as described in the last subsection is a wasteful method if we have more data than only the maxima in each block. Another approach is to regard extreme events as those that exceed a certain threshold, u. Let $X_1, X_2, ...$ be a sequence of independent random variables with common distribution F. We are then

interested in the conditional probability

$$\Pr\{X > u + y \mid X > u\}, \quad y > 0. \tag{3.19}$$

If we define Z_n as in Equation 3.14 and $\Pr\{Z_n < z\}$ follows a GEV distribution as in Equation 3.16, it is possible to show that for large enough u, the distribution of $(X - u)$, conditional on $X > u$, is approximately

$$H(y) = 1 - \left(1 + \frac{\xi y}{\sigma}\right)^{-1/\xi}, \tag{3.20}$$

see (Coles, 2001, Ch. 4) for a justification. The family of distributions given by Equation 3.20 is called the *generalized Pareto family*. The method to use the generalized Pareto family to model excess over a threshold is often called the peak-over-threshold method. In the present study, the shortened name *threshold model* will be used.

This yields the following method to estimate extreme values from a set of datapoints, $x_1, ..., x_n$, with less loss of data than the GEV method. Extreme events are defined as events $\{x_i : x_i > u\}$ exceeding a threshold u. We label these events $x_{(1)}, ..., x_{(k)}$, where k is the number of extreme events, and the threshold excesses by $y_j = x_{(j)} - u$. Following the earlier argument, the distribution of these excesses can be approximated by a generalized Pareto distribution. The parameters can be estimated using maximum likelihood. The log-likelihood is derived from Equation 3.20 as

$$l(\sigma, \xi) = -k \ln \sigma - (1 + 1/\xi) \sum_{i=1}^{k} \ln(1 + \xi y_i/\sigma), \tag{3.21}$$

provided $(1 + \xi y_i/\sigma) > 0$ for all i. Numerical techniques can then be used to maximize the log-likelihood function. This gives us an estimate for the model parameters σ and ξ.

That is, for $x > u$

$$\Pr\{X > x \mid X > u\} = \left[1 + \xi \left(\frac{x - u}{\sigma}\right)\right]^{-1/\xi}. \tag{3.22}$$

Further, we have

$$\Pr\{X > x\} = \nu_u \left[1 + \xi \left(\frac{x - u}{\sigma}\right)\right]^{-1/\xi}, \tag{3.23}$$

where $\nu_u = \Pr\{X > u\}$. From this we can find the level x_m that is exceeded on average once every m observations as

$$\nu_u \left[1 + \xi \left(\frac{x_m - u}{\sigma}\right)\right]^{-1/\xi} = \frac{1}{m}. \tag{3.24}$$

Which we can solve for x_m,

$$x_m = u + \frac{\sigma}{\xi} \left[(m\nu_u)^{\xi} - 1\right]. \tag{3.25}$$

This is the *m-observation return level*. Often we want an N-year return level which is expected to be exceeded once every N years. Assume there are on average n_y observations every year, which means the N-year return level correspond to the $m = Nn_y$ observation return level. From Equation 3.25 it is easy to see that the N-year return level becomes

$$z_N = u + \frac{\sigma}{\xi}\left[(Nn_y\nu_u)^{\xi} - 1\right]. \tag{3.26}$$

To estimate ν_u, the probability of an observation to exceed the threshold, an estimator is

$$\nu_u = \frac{k}{n}, \tag{3.27}$$

the sample proportion of observations exceeding u.

In this derivation we have again defined the observations $x_1, ..., x_n$ as independent events. In cases where this is not a valid assumption we have to be more careful than for the GEV case. A solution is to decluster the data, which correspond to filtering the dependent observations to obtain a set of data which are approximately independent. The method can be summed up as

1. Use an empirical rule to decluster the data.
2. Identify the maximum excess in each cluster.
3. Fit the generalized Pareto distribution to the excess cluster maxima.

The method to decluster the data can range from the very simple to more sophisticated models. To the authors' knowledge, declustering of data has never been applied to snow events and a new method had to be developed. With inspiration from Vaudrey (1987), who studied sea ice ridges, the following algorithm was developed.

A new snow event is defined to start when an observation is r times higher than the minimum observation since the last event, where r is chosen from $r \geq 1$. This is to filter out small fluctuations and to make sure the new event is not too close to be independent from the last event. If r is too small we risk to choose a new event where a large proportion of the observed snow in reality fell during the last event. However if r is chosen too large, we risk missing snow events and thereby losing valuable data. A snow event is then defined to end when the observations fall below α times the maximum value of the snow event, where $0 < \alpha \leq 1$. A backward search from the maximum snow load can then be done to check how long it took to accumulate 80 % of the snow load.

Figure 3.3 shows an example of the declustering algorithm used on a year of snow load data from the Barents Sea. The algorithm performs well and finds both the largest peaks and the smaller snow events, but there are some snow events that did not get selected. The choice of α and r can bias the selection of events to both large and small values of snow load, and we have to take care picking appropriate values.

Non-stationary GEV and model Testing

Non-stationary time series have characteristics that change systematically over time. Non-stationarity often arise from seasonal changes, or can be due to long-term climate

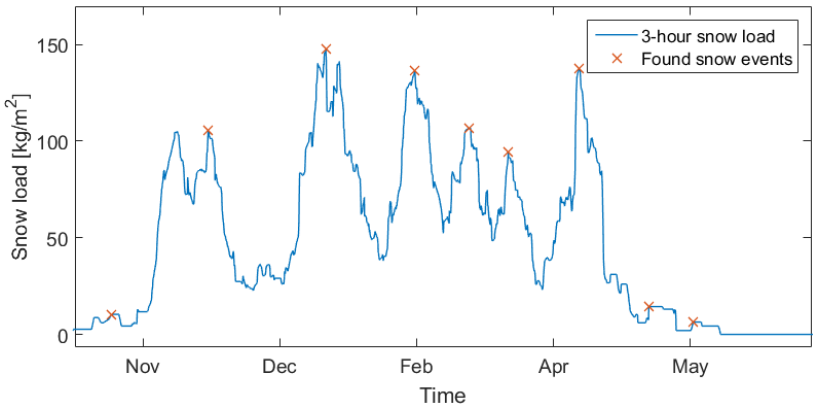

Figure 3.3: Example of the performance of declustering algorithm using $\alpha = 0.5$ and $r = 1.5$. The crosses are the maxima in each snow event while the blue line is snow load data used as input.

trends. The stationary GEV model is applicable to cases with some dependence of the observations, however, it was assumed that there was no long term dependence and thus a new approach is needed to model non-stationary time series.

As an example, lets look at a dataset with annual snow load maxima where the basic level has changed linearly over the observation period, but the extreme distribution is otherwise constant. If the location parameter is allowed to change in time as

$$\mu(t) = \beta_1 + \beta_2 t,$$

for some parameters β_1 and β_2, it follows that a suitable model for Z_t, the extreme snow load in year t is

$$Z_t \sim \text{GEV}(\mu(t), \sigma, \xi), \tag{3.28}$$

where $\text{GEV}(\mu, \sigma, \xi)$ denotes a GEV distribution with parameters μ, σ, and ξ. In this case β_2 would be the change in extreme snow load per year.

Non-stationarity in the variance is also possible. This can for example be modeled as

$$\sigma = \exp(\alpha_1 + \alpha_2 t),$$

where the exponential function ensures the variance parameter always stays positive for all values of t. The uncertainties in estimating the shape parameter ξ is generally so large that it is unrealistic trying to model non-stationarity in this parameter (Coles, 2001).

In general, it is possible to model non-stationarity in a parameter as

$$\theta = h(X^T \beta), \tag{3.29}$$

where θ denotes either μ, σ, or ξ, h is some specified function, X is a model vector and β a vector of parameters to be estimated. The T denotes the transposed of the

vector. Returning to the previous example, σ can now be written on the form

$$\sigma(t) = \exp\left\{[1, t]\begin{bmatrix}\alpha_1 \\ \alpha_2\end{bmatrix}\right\}.$$

Writing the non-stationarity on the form as in Equation 3.29 simplifies the implementation of the method, and makes it possible to write a computer code that takes in a general X and h and estimates the corresponding distribution of the data.

When using maximum likelihood to estimate the distribution parameters as in Equation 3.18, it is easy to make changes to the model structure. Let a non-stationary GEV (NSGEV) describe the distribution of Z_t for $t = 1, 2, ..., n$

$$Z_t \sim \text{GEV}(\mu(t), \sigma(t), \xi(t). \tag{3.30}$$

where each of the $\mu(t)$, $\sigma(t)$ and $\xi(t)$ has an expression on the form of 3.29. Letting β denote the entire parameter space, the log-likelihood is simply then

$$l(\beta) = -\sum_{t=1}^{n}\left\{\ln\left(\sigma(t)\right) + (1 + 1/\xi(t))\ln\left[1 + \xi(t)\left(\frac{z_t - \mu(t)}{\sigma(t)}\right)\right] + \left[1 + \xi(t)\left(\frac{z_t - \mu(t)}{\sigma(t)}\right)\right]^{-1/\xi(t)}\right\}, \tag{3.31}$$

given that $\xi \neq 0$ and

$$1 + \xi(t)\frac{z_t - \mu(t)}{\sigma(t)} > 0, \text{ for } t = 1, 2, ..., n.$$

For the case $\xi(t) = 0$ it is necessary to use the appropriate limiting form as $\xi(t) \to 0$, similarly to what was done in the case of the stationary GEV. Equation 3.31 can easily be maximized numerically with a computer software, yielding an estimate of β.

Three different non-stationary GEV (NSGEV) models (see Table 3.2) describe changes in the data, in addition to a stationary GEV (SGEV). In Model 1, the location parameter μ, was allowed to vary in time, while the scale and shape parameter were set to constants. This represents a trend in the location, i.e. magnitude, of the extreme events. A positive β_2 indicates an increasing trend, while a negative β_2 indicates a decreasing trend. Model 2 represents a trend in the scale, or spread, of the extreme events. A positive α_2 indicates an increasing trend, and a negative α_2 indicate a decreasing trend. Increasing spread of extremes will lead to higher return values and decreasing trends in the spread will lead to lower return values with time. Model 3 represents trend in both the location and the scale of extreme events. This model is the most flexible, however it also have the most parameters to estimate.

From the four models (one SGEV and three NSGEV) considered, the corresponding distributions are estimated from the yearly maxima of snow load by maximum likelihood as described earlier in this chapter. The Akaike information criterion AIC (Akaike, 1974) is used to decide which of the NSGEV models gives the best fit to the data with a minimum number of estimated parameters. The AIC is defined by

$$AIC_m = 2k_m - 2l_m \tag{3.32}$$

where k_m is the number of estimated parameters of the model, and l_m is the maximized log-likelihood. AIC compromises a good fit (high likelihood) and low complexity (low number of parameters). It is important to point out that the models tested have to be fitted to the same dataset and thus we can not use AIC to compare a GEV model against a threshold model.

For each of the three NSGEV models, a AIC value is computed and the model with the lowest AIC value is selected. Then a likelihood ratio test at level 90 % is used to test whether or not the selected model performs significantly better than the SGEV model. The likelihood ratio test uses the test statistic

$$D = 2\left\{l_i(M_i) - l_0(M_0)\right\}, \tag{3.33}$$

where $l_i(M_i)$ and $l_0(M_0)$ are the maximized log-likelihood of model of model M_i (the selected NSGEV model) and model M_0 (the SGEV model) respectively. Large values of D indicates that M_i explains significantly more of the variation in the data than M_0. How large D has to be before we prefer model M_i to M_0 is decided by the distribution of the test statistic. Specifically it can be shown (see (Coles, 2001, Ch. 2 and Ch. 6)) that model M_0 is rejected by a test at the α-level of significance if $D > c_\alpha$, where c_α is the $(1-\alpha)$ quantile of the χ^2_k distribution, and k is the difference in dimensionality between M_i and M_0.

Table 3.2: The 4 different GEV models applied to the annual maxima of snow loads. t is the index of the year, ranging from 1 to 58. Thus, the first year in the time series, 1957, correspond to $t = 1$, while the last year, 2015, corresponds to $t = 58$.

	Location μ	Scale σ	Shape ξ
Model 0:	const.	const.	const.
Model 1:	$\beta_1 + \beta_2 t$	const.	const.
Model 2:	const.	$\alpha_1 + \alpha_2 t$	const.
Model 3:	$\beta_1 + \beta_2 t$	$\alpha_1 + \alpha_2 t$	const.

4 Results

4.1 Validation of NORA10

In the present validation of NORA10, we used data from the meteorological stations at Hopen, Bjørnøya and Fruholmen Fyr. Observational data of precipitation is compared to precipitation in NORA10, with emphasis on extreme precipitation events, rather than averages, to investigate how applicable extreme snow events from NORA10 are.

Scatter plots of observed precipitation and model precipitation from NORA10 are shown in Figure 4.1. The ability of the hindcast to predict the correct precipitation in a given time step is not very high. There is a very weak correlation between observed precipitation and data from NORA10, more distinct at Bjørnøya than at Fruholmen Fyr and Hopen, with correlation coefficients of 0.62, 0.55 and 0.54 respectively. Many of the highest precipitation events observed are only estimated as small events by NORA10, and vice versa. If we look more closely at the time series, comparing the two datasets, we see that the hindcast often manages to capture the timing of the precipitation, but misses on the actual value, as shown in the excerpt from the time series at Bjørnøya shown in Figure 4.2.

Figure 4.3 shows histograms of 12-hour precipitation from the time period 1957 to 2015. The frequency of dry periods is shown as an arrow on the y-axis. At all locations the hindcast overestimates the number of wet days. The ratios of wet 12 hour periods to dry 12 hour periods are 0.65 and 0.76 for observations and NORA10 respectively at Hopen, 0.70 and 0.89 for observations and NORA10 at Bjørnøya, and 0.61 and 0.76 for observations and NORA10 at Fruholmen Fyr. We can see this effect in Fig. 4.2 where in the period from September to February, NORA10 only predicts some dry days in the beginning of September, while the observations show there were multiple days with no precipitation during the period. Further, the hindcast overestimates the frequencies at middle precipitation intensities (0.5 mm to 10 mm). For higher precipitation rates, NORA10 has a very similar distribution at all locations. At Hopen, there have been 11 observations with intensity higher than 24 mm/12 h, which is the maximum intensity estimated by NORA10 at the location. At Bjørnøya and Fruholmen fyr the hindcast predicts the frequency and magnitudes of extremes very well as seen. However, at Bjørnøya the most extreme event observed is 38 mm/12 h while the most extreme precipitation rate from the hindcast is 27 mm/12 h.

To investigate any seasonal discrepancies between NORA10 and the observations,

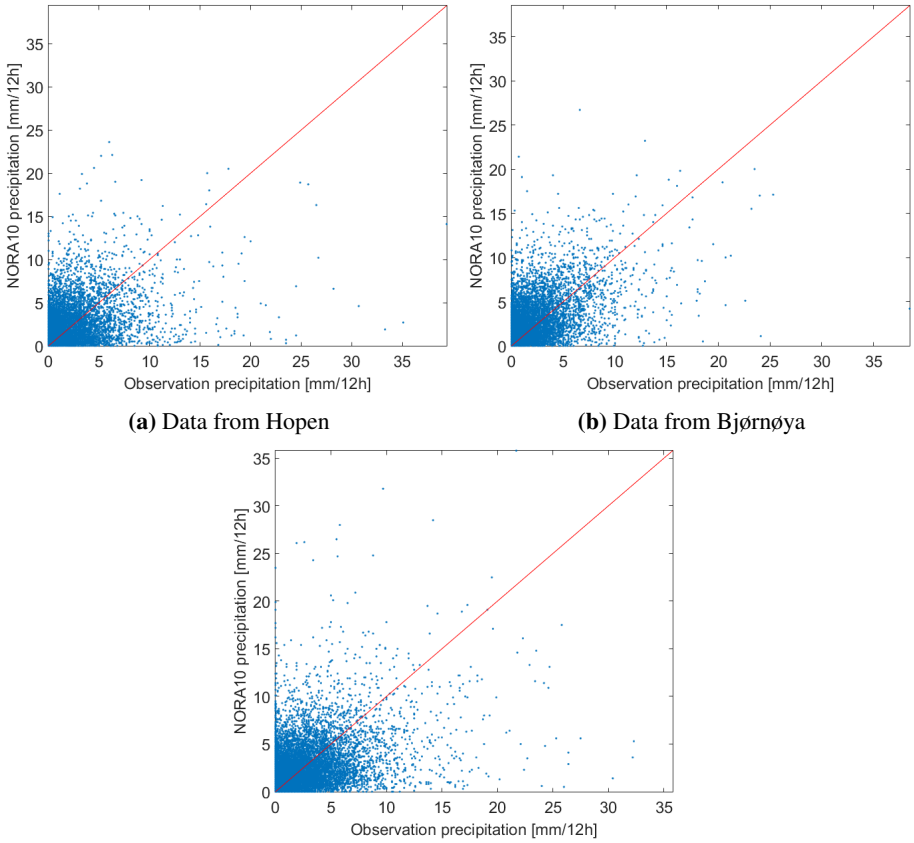

(a) Data from Hopen

(b) Data from Bjørnøya

(c) Data from Fruholmen fyr

Figure 4.1: Scatter plot of 12 hour accumulated precipitation from NORA10 data and observations from E-klima. Data from Hopen (**a**), Bjørnøya (**b**) and Fruholmen Fyr (**c**) is used.

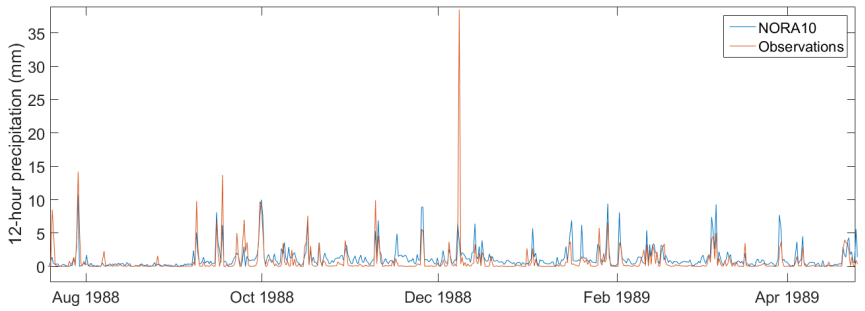

Figure 4.2: Excerpt of the time series of the precipitation of NORA10 and observations at Bjørnøya during the winter of 1988/1989. The largest peak in December is the most extreme precipitation event observed at the station in the dataset used (1957 to 2015). During the event the air temperature was around -2 °C.

we found the mean precipitation for every day of the year during the period studied. The results for the three locations are plotted in Figure 4.4. Precipitation in the hindcast shows different bias at the locations and for the seasons. At Fruholmen, NORA10 shows negligible bias compared to the observations throughout the year. At Bjørnøya, however, NORA10 shows a wet bias of 1 mm/day to 1.5 mm/day during the winter months, which corresponds to NORA10 having 70 % to 110 % larger mean daily precipitation than the observed precipitation. In the summer, however, there is good agreement of between NORA10 and the observations. At Hopen, NORA10 shows a small wet bias throughout the year, with the exception of the middle of September to December, when the bias is much larger (up to 70 %).

4.2 Analysis of the x-day snowfall model

To investigate the sensitivity of extreme snow loads to the choice of the number of accumulation days, we ran the model with a range of days from 1 to 30, and calculated the corresponding 100-year extreme snow load value. This was done at the locations of Fruholmen Fyr, Johan Castberg, Bjørnøya and Hopen. All locations showed similar linear trends (increase of (3.9, 3.5 3.4, 3.3) kg m^2 d^{-1} respectively for the linear fit) with increasing 100-year snow load value with increasing accumulation period. As an example, the plot from Johan Castberg is shown in Figure 4.5. Interestingly, the increase in load per extra day of accumulation was very similar across the different locations, even though the 100-year values are different. At all locations the increase was approximately 3.5 kgm^2 d^{-1}. This means that using a 3 day accumulation period instead of 10 days will reduce the estimated 100-year snow load with 24 kg/m^2, which constitutes a 30 % decrease at Johan Castberg. The results from an analysis using the x-day snowfall model will therefore be quite sensitive to the choice of accumulation period.

To compare the snow loads estimated by the x-day model with a physically based

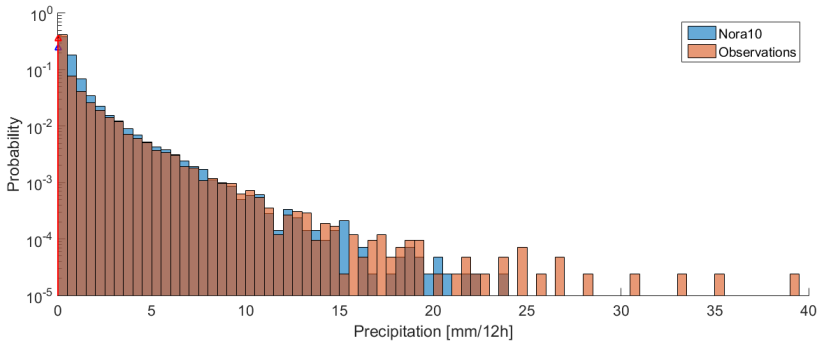

(a) Data from Hopen

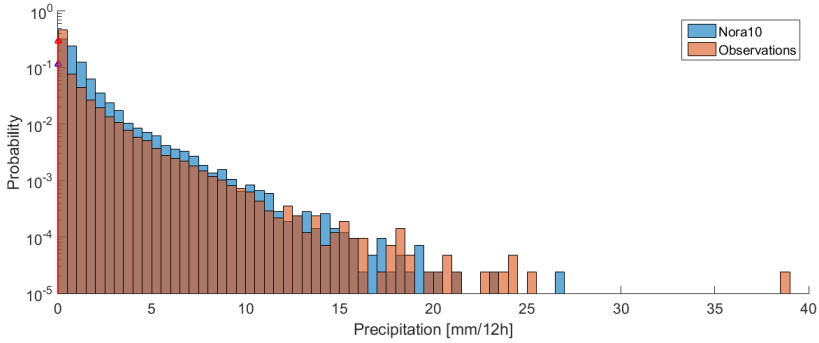

(b) Data from Bjørnøya

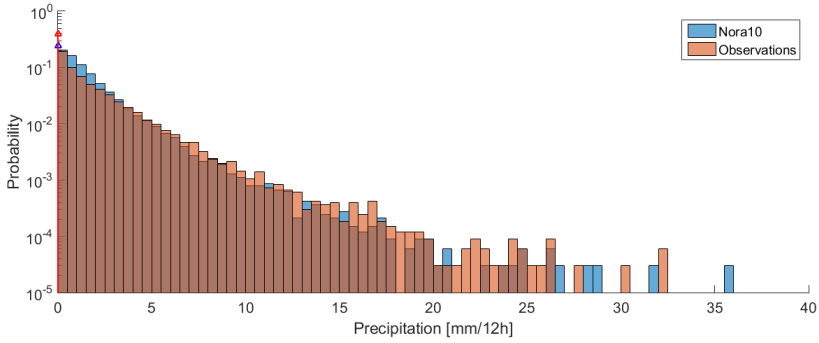

(c) Data from Fruholmen fyr

Figure 4.3: Histogram of 12 h accumulated precipitation at Hopen (**a**), Bjørnøya Meterological station (**b**) and at Fruholmen Fyr (**c**).The corresponding NORA10 grid point was found using nearest-neighbor method. The y-axis has a logarithmic scale, and the histogram is scaled as a probability density.

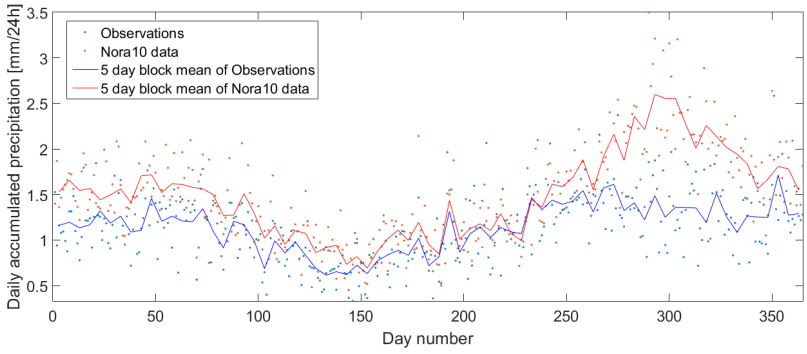

(a) Data from Hopen

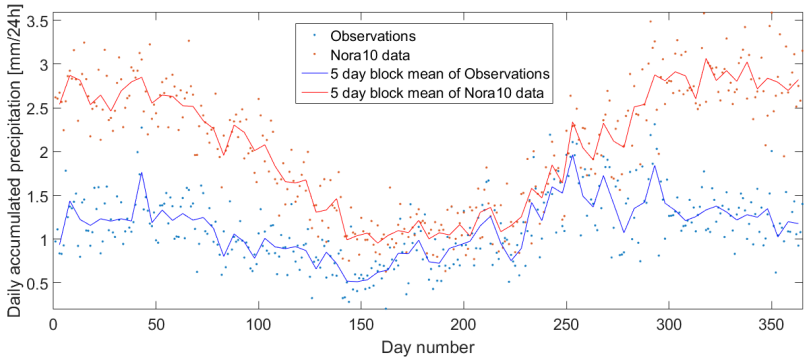

(b) Data from Bjørnøya

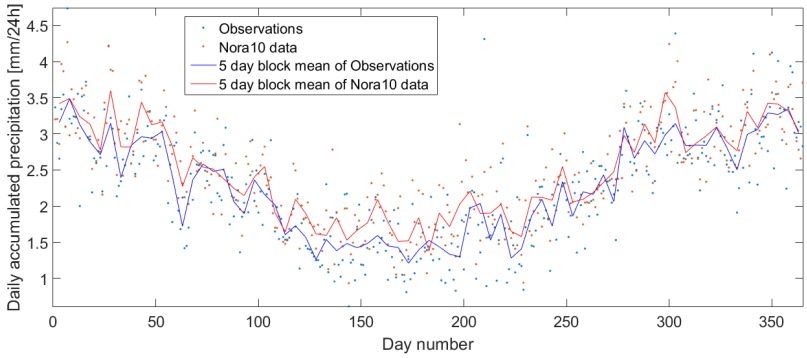

(c) Data from Fruholmen fyr

Figure 4.4: Mean daily precipitation during the observation period in mm/day. Data from Hopen (**a**), Bjørnøya (**b**) and Fruholmen Fyr (**c**) is used.

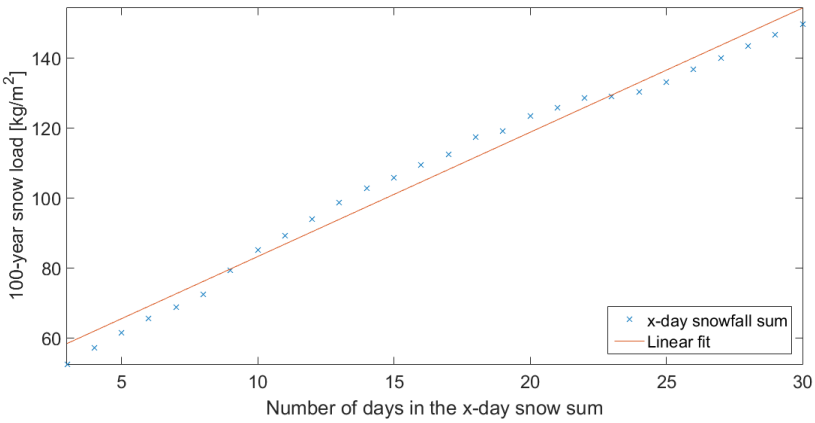

Figure 4.5: 100-year snow load from the x-day snowfall model as a function of number of accumulation days. A SGEV distribution has been used to estimate the 100-year return levels. Meteorological data are from the Johan Castberg location.

model, the energy balance model described in Chapter 3.2.2 was used to estimate snow loads. We also used the energy balance with the wind drift model assuming a platform length of 30 m to gauge the effects of wind on the snow loads. At Johan Castberg the yearly maxima from this model together with yearly maxima from the 15-day snowfall- and 5-day snowfall model are plotted in Figure 4.6. The 15-day snowfall model yields similar results as the energy balance model, however there is more variability in the estimated yearly maxima using the energy balance model.

The wind drift, however, greatly reduces the yearly maximum snow loads, and the 5-day snowfall sum shows a much larger agreement than the 15-day snowfall sum with the snow loads from the energy balance model with wind drift. Some of the large year-to-year variation seen with the energy balance model is also not present when using the snow drift model. This means that the x-day snowfall model is able to better capture the characteristics of the maximum yearly snow load of the energy balance model with wind drift than without.

Comparing 100-year return levels for snow load from the different models, also yields similar results at different locations. A summary is shown in Table 4.1. The table shows 100-year snow loads estimated by a SGEV model from computed snow loads at different locations, and with different models. The energy balance model shows the highest snow loads at Barents South-East and Bjørnøya, and the lowest 100-year return levels at Johan Castberg. This trend is not clear when combining the snow drift model with the energy balance model, then the return levels are highest at Fruholmen Fyr. For the x-day snowfall models, the yearly maxima stays about constant for all the studied locations, and none of the x-day models estimates similar return levels as the energy balance model at all locations. The 5-day snowfall model estimates lower 100-year return level at Fruholmen and Barents South-East compared to the energy balance with drift.

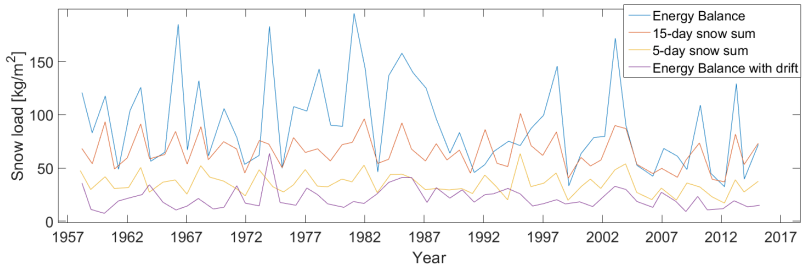

Figure 4.6: Yearly maxima of snow load using different melting models at the Johan Castberg location.

Table 4.1: Summary of the mean of 100-year return levels of snow loads at different location using the energy balance model (EB) with and without drift, and 15, 10 and 3-day snowfall sum without drift. All values are in kg/m^2 and the SGEV model has been used for extreme statistics.

	Fruholmen	Johan Castberg	Bjørnøya	Barents South-East
EB	328	245	382	383
EB, with drift	99	58	48	74
15-day snowfall	93	106	92	97
10-day snowfall	72	85	73	74
5-day snowfall	55	61	54	54

It was suspected that the large snow loads further north in the Barents Sea (e.g. at Barents South-East) were due to very little melting during the winter, and thus accumulation over a very long period. During November to March there is essentially no incoming shortwave radiation, and the longwave radiation is usually negative. We therefore studied the time required to accumulate the high snow loads of the energy balance model.

Snow events from the time series of snow load using the energy balance model without drifting snow were found by using the declustering algorithm described in Chapter 3.3. The duration of an event was then defined as the time to accumulate the last 80 % of the event's maximum snow load. The investigations showed that the extreme snow loads use a long time to accumulate, as seen in Figure 4.7a. All the events, except two, larger than 100 kg/m^2 took longer than 19 days to accumulate. The event with the longest duration took over 170 days to accumulate to maximum snow load. The maximum snow load of an event is approximately proportional to the duration of an event. This suggests that the intensity of a single storm is less important than accumulation over a longer time period.

We used the wind drift model described in Section 3.2.3, assuming a completely flat platform of length 30 m, together with the energy balance model to see how the duration of events changed if wind drift is included. The results are plotted in Figure 4.7b. There is no longer a very clear trend for larger events to accumulate for a longer duration, and the largest event at Fruholmen Fyr used only 17 days to accumu-

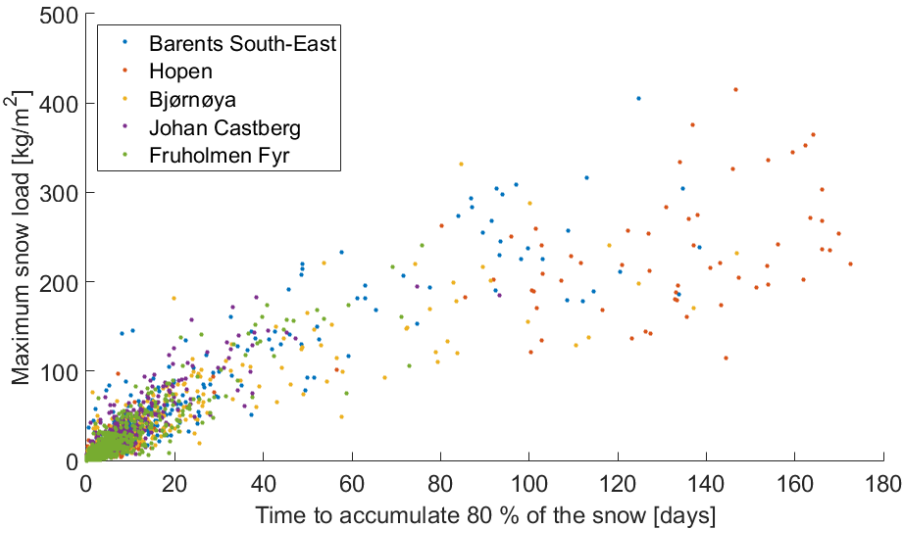

(a) Time to accumulate without wind drift

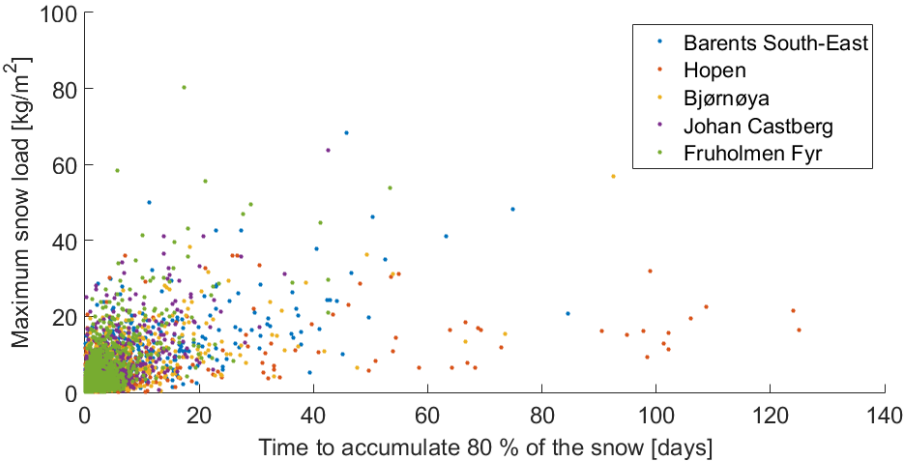

(b) Time to accumulate with wind drift

Figure 4.7: The duration of snow events estimated by the energy balance method at the Johan Castberg location. (**a**) shows the result without accounting for wind drift and (**b**) shows the results with wind drift. The duration is here defined as the number of days the event used to accumulate the last 80 % of the snow (from 20 % of maximum snow load to maximum).

late. Still, many of the yearly maxima occur within a shorter time span, and many of the extreme events accumulate within a week.

4.3 Using the 10-day snowfall sum and extreme statistics to estimate snow loads

In this part we present the results from a case study where we used the methods described in Chapter 3 to calculate time series of snow load, and statistical 100-year values. The locations of Barents South-East and Johan Castberg were chosen for the study and are shown on the map in Figure 2.1.

In the case study, we used the SGEV method and the threshold method to calculate return levels. As input, snow loads from a 10-day snowfall sum model were used, both with and without the drift model described in Chapter 3.2.3. The main objective is to investigate extreme snow loads at the locations and estimate 100 and 10 000 year return values of snow load. A comparison between the GEV model and the threshold model for extreme values is also of interest, to see if one of the models performs better. Then, to investigate any trends in the extreme distribution, we used a non-stationary GEV model as described in Chapter 3.3.

We assumed a square, flat helicopter deck with length of 30 m in the study, further assumptions are

- The helicopter deck is always on the windward side of the platform
- No influence or sheltering from the rest of the structure
- No snow transport from other parts of the platform
- All other assumptions made in the snow drift model and x-day snowfall models

The assumption are reasonable if the helicopter deck is part of a ship-shaped platform, as a ship often tries to keep the bow against the waves, which is likely to also be close to the predominant wind.

4.3.1 Johan Castberg

The time series of snow loads calculated using the 10-day snowfall model and NORA10 from the grid point at Johan Castberg as input, are plotted in Figure 4.8. Maximum snow load was 82 kg/m^2 (74 ton total load on the helicpoter deck) and the mean of the yearly maxima was 51 kg/m^2 (46 ton) with a standard deviation of 12 kg/m^2.

Return Levels without snowdrift

From Figure 4.8 it looks like there might be a slight trend of lower annual snow maxima after 1990. For simplification and comparison between the GEV and threshold model, we assume the yearly maxima can be modeled as independent observations from the GEV distribution.

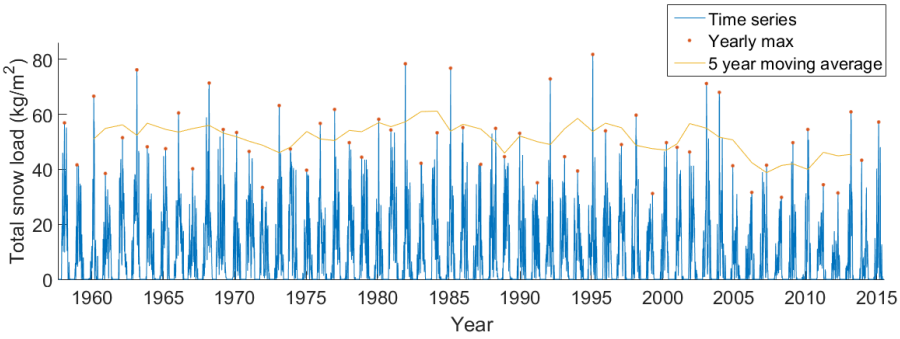

(a) Snow loads without snow drift

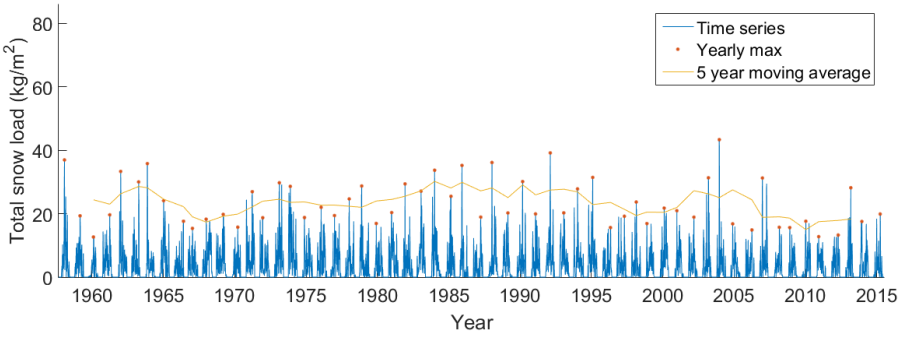

(b) Snow load with snow drift

Figure 4.8: Time series of snow loads at Johan Castberg, with annual maxima plotted as dots. Data from NORA10 were used as input in a 10-day snowfall model to estimate the loads. (**a**) is estimated without the snow drift model, while (**b**) is estimated with snow drift. The y-scale is equal in the two plots for comparison.

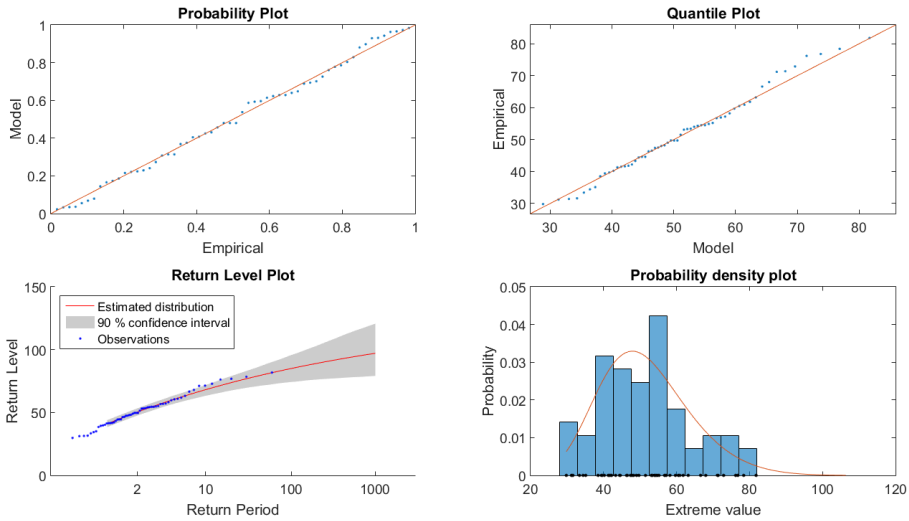

Figure 4.9: Diagnostic plots for SGEV fit to annual maxima of snow loads at Johan Castberg. Snow loads have been estimated using the 10-day snowfall model without snowdrift.

The maximum-likelihood estimates of the NGEV model are

$$(\hat{\mu}, \hat{\sigma}, \hat{\xi}) = (46.3, 11.2, -0.14),$$

where the units of μ and σ are in kg/m^2, ξ is dimensionless. Bootstrap confidence intervals with the percentile method yields 90 % confidence intervals of [44.3, 48.6] for μ, [9.6 12.5] for σ and [-0.27, -0.03] for ξ. The negative ξ parameter indicates that the estimated extreme distribution is bounded with a maximum value of $\mu - \sigma/\xi = 140$ kg/m^2. The estimated 100 and 10 000 year return levels of snow load are 85 kg/m^2 and 106 kg/m^2, respectively. This corresponds to a total snow load on the helicopter deck of 77 ton and 95 ton, or 28 cm and 35 cm snow thickness assuming a snow density of 300 kg/m^3.

Various diagnostic plots to assess the estimated fit are shown in Figure 4.9. The plots do not give any evidence for us to mistrust the fit. The SGEV model fits the data at both lower quantiles, which is seen in the probability plot, and at higher quantiles (quantile plot). The variation of the data from the estimated distribution is within the expected sampling variation as seen in the return level plot. The 90 % confidence interval in this plot shows the 90 % range in return levels when drawing samples from the estimated distribution. Even though the plots cannot be used to prove that the data follows a SGEV model, they do increase the trust in the model. The return level plot shows how the return level is curved because of the negative ξ parameter and the return level will asymptotically go towards the maximum values for higher return periods.

Then the threshold model was used to calculate extreme snow loads. The declustering algorithm described in section 3.3 yielded 533 snow events with a mean of

Table 4.2: Summary of the different estimated values using the GEV distribution and threshold method at Johan Castberg. Snow load estimated with the 10-day snowfall model.

	Without snowdrift		With snowdrift	
	GEV	Threshold	GEV	Threshold
100-year value (kg/m^2)	85	82	50	43
10 000-year value (kg/m^2)	106	93	93	58
ξ-parameter	-0.14	-0.24	0.07	-0.10
Upper bound (kg/m^2)	140	100	-	84

22.8 kg/m^2 and a standard deviation of 17.0 kg/m^2. Using a threshold of 30.5 kg/m^2 (equivalent of the 70th percentile) the data was fitted to the generalized Pareto distribution. The maximum-likelihood estimates with σ in kg/m^2 were

$$(\hat{\sigma}, \hat{\xi}) = (16.5, -0.24),$$

again with $\xi < 0$ indicating a bounded distribution with maximum value of $u - \sigma/\xi = 100$ kg/m^2, where u is the selected threshold. Diagnostic plots for the fit are plotted in Figure 4.10. None of the plots indicate that the model does not fit the data. Neither the probability plot nor the quantile plot discovers any large deviance from the distribution in the data. The 10 largest events are somewhat higher than what is expected from the estimated distribution, as seen in the quantile plot, but this can be explained by sampling variability as seen in the return level plot. The 100-year value of snow load was calculated from Equation 3.25 to 82 kg/m^2 and the 10 000-year value of snow load is 93 kg/m^2. This corresponds to a total snow load on the helicopter deck of 73 ton and 83 ton, respectively. A summary of estimated values at Johan Castberg can be found in Table 4.2. As seen, the estimated return values are very similar which increases the trust in both methods. The 10 000 year values differ by only around 10 %, which is not much, given the large extrapolation.

Return levels with snowdrift

To further investigate the condtions at Johan Castberg, we included the snowdrift model covered in Chapter 3.2.3. As discussed in the chapter, there are great uncertainties in the model, but it can gives us qualitative information on how snow drift affects the extreme snow loads.

As seen in Figure 4.8, using the snow drift model drastically reduces the snow load. The maximum snow load in the period was 43 kg/m^2,which is 48 % lower than the maximum snow load without snowdrift. The mean of the yearly maxima is 23 kg/m^2 with a standard deviation of 7.4 kg/m^2. The maximum-likelihood estimates of the parameters of the SGEV distribution are

$$(\hat{\mu}, \hat{\sigma}, \hat{\xi}) = (19.8, 5.6, 0.07), \tag{4.1}$$

where μ and σ are in units of kg/m^2. 90 % confidence intervals calculated with the percentile bootstrap method are [18.9, 20.9] for μ, [4.7, 6.3] for σ and [-0.09, 0.20]

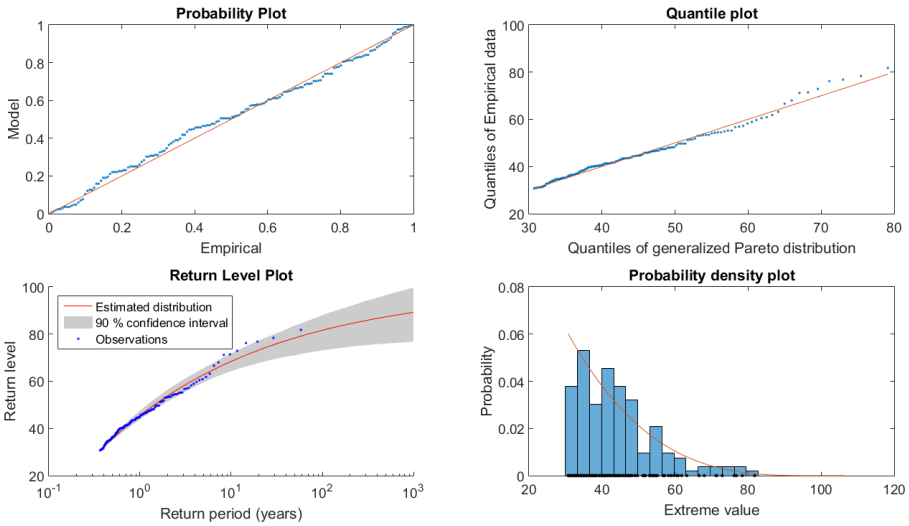

Figure 4.10: Diagnostic plots for threshold model fit to the threshold excess at Johan Castberg using a threshold of 30.7 kg/m^2. The 10-day snowfall model without snowdrift has been used to estimate snow loads.

for ξ. The ξ parameter is very close to zero, indicating that the yearly maxima of snow load with the snowdrift model is following a distribution close to the Gumbel distribution.

Figure 4.11 shows various diagnostic plots for the SGEV model fit to the data. The plots show that there are some variations between the model and the yearly maxima, however, this can be explained by sampling variability. The 100 and 10 000 year return values are 50 kg/m^2 and 93 kg/m^2, respectively.

Then the threshold model was used with the time series of snow load with snowdrift as input. Using the declustering algorithm we found 878 events, with a mean of 8.2 kg/m^2 and a standard deviation of 7 kg/m^2. A threshold of 10.32 kg/m^2 was used and the excess were fitted to a generalized Pareto distribution. The maximum-likelihood estimates for the parameters are

$$(\sigma, \xi) = (7.1, -0.10), \tag{4.2}$$

where σ is in kg/m^2. The negative ξ parameter suggests a bound distribution in contrast to the SGEV model which estimated an unbound distribution. The 100 and 10 000 year values are 43 kg/m^2 and 58 kg/m^2.

Trends in the extreme snow loads

From Figure 4.8 it looks like there might be a slight trend of lower annual snow maxima with less variation after 1995. The variation was modeled with the models in Table 3.2. The corresponding log-likelihoods and Akaike information criterion (AIC)

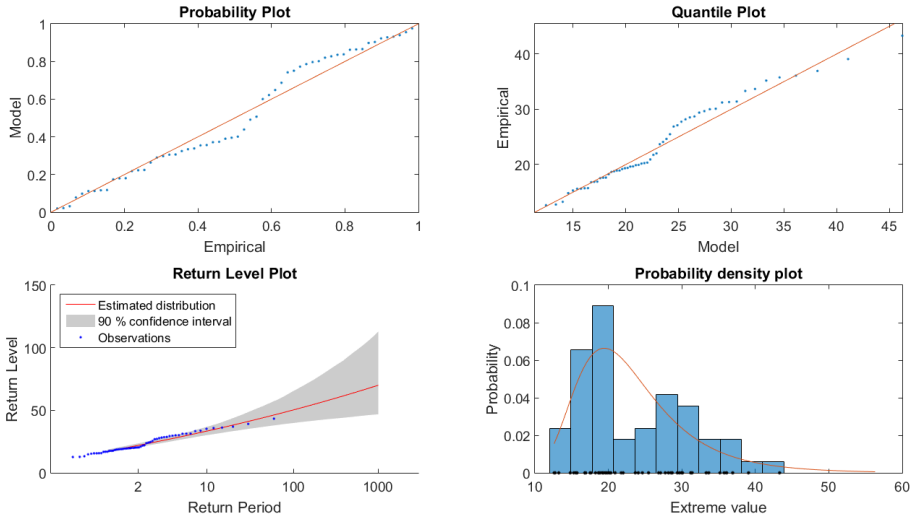

Figure 4.11: Diagnostic plots for the SGEV model fit to the yearly maximum snow loads at Johan Castberg using the 10 day snowfall sum model including snowdrift.

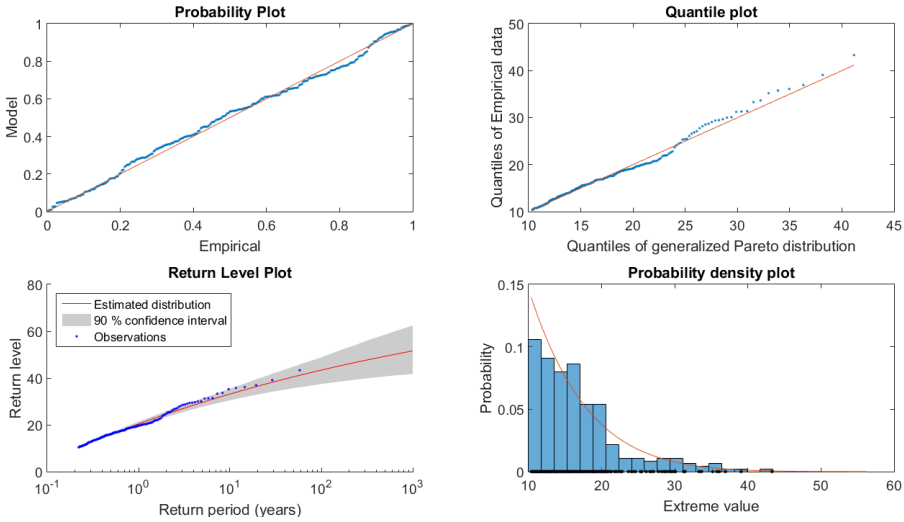

Figure 4.12: Diagnostic plots for threshold model fit to the threshold excess at Johan Castberg using a threshold of 10.32 kg/m^2. The 10-day snowfall model with snowdrift have been used to estimate snow loads.

Table 4.3: Yearly maximum snow loads from Johan Castberg has been fitted to the models in Table 3.2. The table shows estimated log-likelihood of the models with corresponding AIC.

	Log-likelihood	AIC
Model 1:	-220.18	448.36
Model 2:	-221.38	450.77
Model 3:	-220.07	450.14

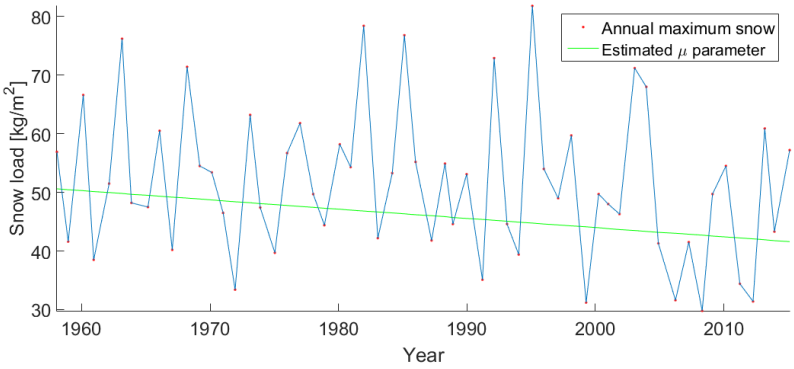

Figure 4.13: Plot of estimated yearly maximum snow loads at Johan Castber using a 10-day snowfall model. Also shown in the plot is the fitted μ-parameter of the NSGEV Model 1, assuming a linear trend in the location parameter $\mu = \beta_1 + \beta_2 t$

are shown in Table 4.3. Model 1[1] is the minimum AIC estimate and chosen as the best NSGEV model. The deviance statistic of Model 1 against the stationary (all parameters are constant) Model 0 is $D = 3.29$ which is larger than the needed χ^2_1 quantile (2.7) needed to indicate a significant trend at an $\alpha = 90$ % level, but not at an $\alpha = 95$ % level. The test thus provides some evidence for a linear trend in the location parameter with time. To investigate the trend, Model 1 is studied further.

The maximum-likelihood estimates of Model 1 are

$$(\hat{\beta_1}, \hat{\beta_2}, \hat{\sigma}, \hat{\xi}) = (51, -0.16, 10.6, -0.08),$$

where $\beta_2 = -0.16$ kg m^{-2} a^{-1} indicates a trend in the return level of -0.16 kg/m^2 per year. The yearly maximum snow loads and the fitted μ-parameter are shown in Figure 4.13. Equation 3.17 shows that return levels will decrease with the same rate as μ if σ and ξ are constants. Using a percentile bootstrap method, approximate 90 % confidence intervals for the parameters are $[47, 55]$ for β_1, $[-0.27, -0.04]$ for β_2, $[8.9, 11.8]$ for σ and $[-0.23, 0.04]$ for ξ. $\xi < 0$, which indicates a bounded distribution, however the value is very small and the 90 % confidence interval spans 0, so it is not possible to draw a conclusion on the shape of the distribution.

[1]Model 1 assumes a linear trend in the location parameter $\mu = \beta_1 + \beta_2 t$, while the scale paramter σ and the shape parameter ξ are not varying in time.

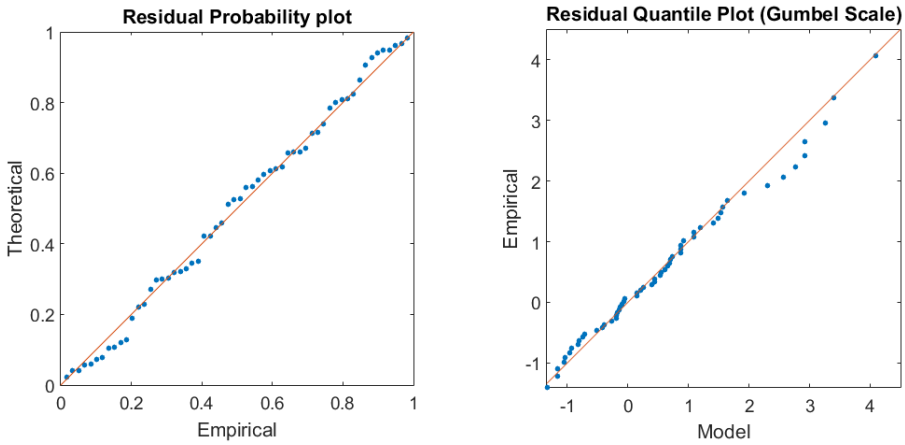

Figure 4.14: Diagnostic plots for the non-stationary GEV fit to the annual maxima of snow loads at Johan Castberg. Model 1 from Table 3.2 was used, assuming a linear trend in the location parameter, $\mu = \beta_1 + \beta_2 t$

Further, diagnostic plots for the fit are plotted in Figure 4.14. The probability plot and quantile plot mostly indicate a good fit of the model, but with some deviations at higher percentiles. However the deviation can be explained by sampling variation and does not lead to doubt of the validity of the model. The 100-year value of snow load at the end of the period [2] was calculated by Eq. 3.17 to 74 kg/m^2 and the 10 000-year value was calculated to 100 kg/m^2. This is a reduction of 18 % compared to the 100-year return value from the beginning of the time series ($t = 0$).

4.3.2 Barents South-East

Barents South-East was then used in the case study. The location of the NORA10 grid point is in the newly opened part of the southeastern Barents Sea and can be seen in Figure 2.1. The time series of estimated loads are plotted in Figure 4.15. The maximum estimated snow load without drift in the period was 68.5 kg/m^2 on the helicopter deck, which corresponds to a total snow load of 62 tons and a snow thickness of 23 cm, assuming a density of 300 kg/m^2. The mean of the yearly maxima was 49 kg/m^2 (44 tons), with a standard deviation of 10 kg/m^2. The maximum estimated snow load while using the drift model was 53 kg/m^2 (48 ton). The mean of the yearly maxima was 24 kg/m^2, with a standard deviation of 8.5 kg/m^2.

Return levels without snowdrift

There is a slight trend in the data with lower snow loads in the 2000s. Trends according to the models in Table 3.2 were tested for and found insignificant. A stationary

[2] Year 2015, $t = 58$

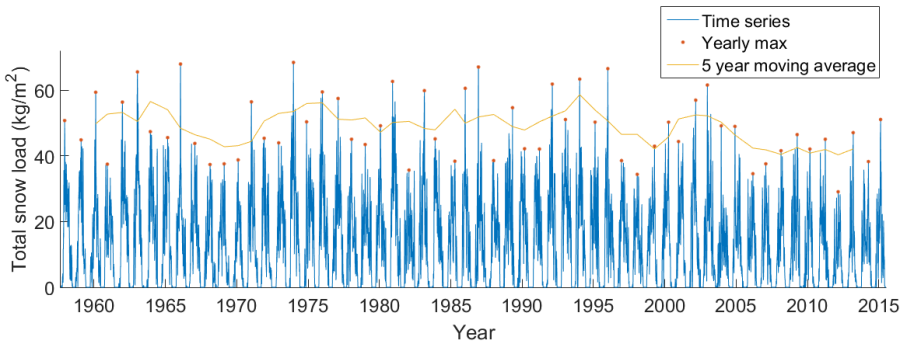

(a) Snow load without drifting snow

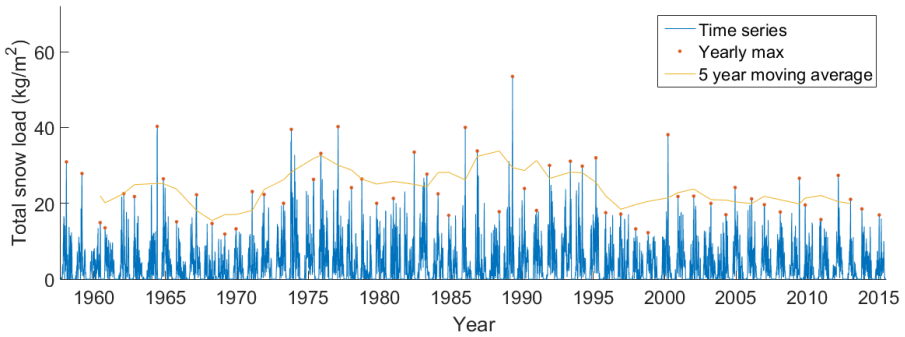

(b) Snow load with drifting snow

Figure 4.15: Time series of snow loads at Barents South East, with annual maxima plotted as dots. Data from NORA10 were used as input in a 10-day snowfall sum model to estimate the loads. In (**a**) the snow was not allowed to drift, while in (**b**) the drift model in Section 3.2.3 was used

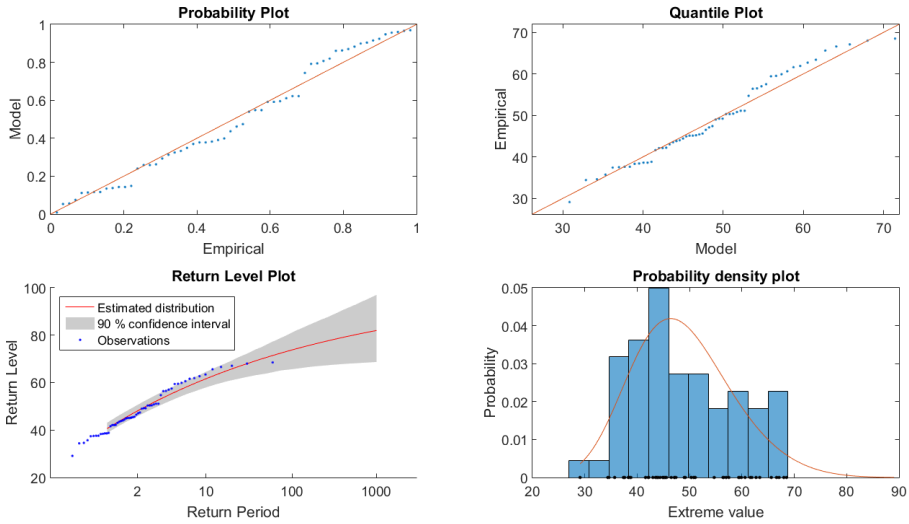

Figure 4.16: Diagnostic plots for GEV fit to the annual maxima snow loads at Barents South-East. The 10-day snowfall model was used without snowdrift

GEV model was thus used to model the extreme distribution. The maximum log-likelihood yields

$$(\hat{\mu}, \hat{\sigma}, \hat{\xi}) = (44.8, 8.9, -0.16), \tag{4.3}$$

where μ and σ has units kg/m^2. Estimated 90 % confidence intervals are [43.3, 46.7] for μ, [7.5, 10.0] for σ and [-0.30, -0.05] for ξ. The estimated ξ parameter is negative indicating a bounded distribution with a maximum value of $\mu - \sigma/\xi = 100$ kg/m^2. Diagnostic plots are shown in Figure 4.16. The data show a decent agreement with the GEV model when taking sampling variability into account. Estimated return values are obtained by Eq. 3.17. The 100 and 10 000 year return values are 74 kg/m^2 and 88 kg/m^2, respectively. A summary of the estimated parameters can be seen in Table 4.4.

Then we used the threshold model to estimate extreme values to compare with the results of the SGEV model. The declustering algorithm described in section 3.3 yielded 555 snow events with a mean of 23 kg/m^2 and a standard deviation of 16.3 kg/m^2. Using a threshold of 33 kg/m^2 (equivalent of the 70th percentile) the data was fitted to the generalized Pareto distribution. The maximum-likelihood estimates were

$$(\hat{\sigma}, \hat{\xi}) = (13.2, -0.28),$$

again with $\xi < 0$ indicating a bounded distribution with maximum value of $u - \sigma/\xi = 81$ kg/m^2, where u is the selected threshold. Diagnostic plots for the fit are plotted in Figure 4.17. None of the plots indicate that the model does not fit the data. The 100-year value of snow load was calculated from Equation. 3.25 to 71 kg/m^2 and the 10,000-year value of snow load was calculated to 78 kg/m^2. At Barents South-East

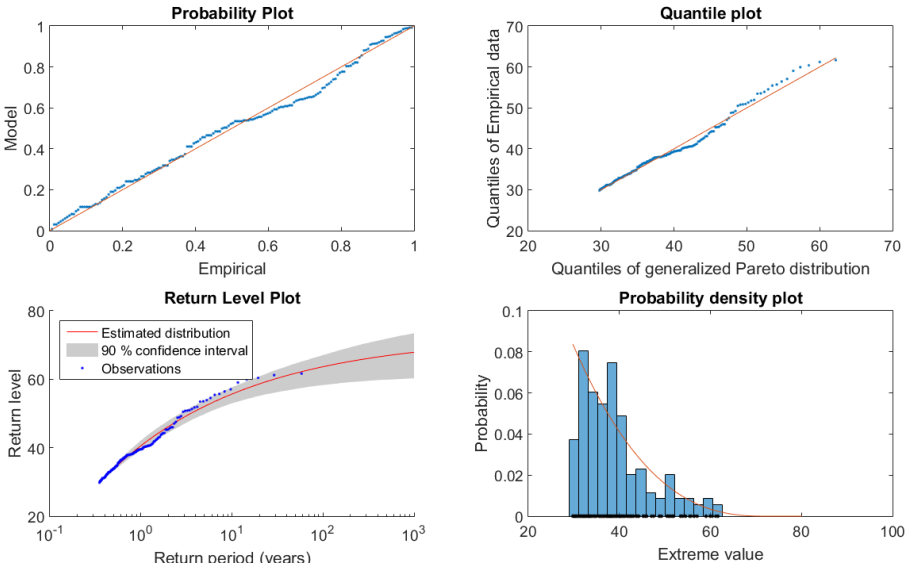

Figure 4.17: Diagnostic plots for threshold model fit to the threshold excess at Barents South East using a threshold of 33 kg/m^2. Time series of snow load estimated using the 10-day snowfall model without snowdrift.

the SGEV model and the threshold model predicts very similar return levels, although at both locations the latter model predicts smaller return levels than the SGEV model. Worth noting is that the return levels of snow load are smaller at Barents South-East than Johan Castberg.

Return values with wind drift

To extend the results, the drift model was used in combination with the 10-day snowfall sum model to estimate the effects drifting snow has on the extreme snow loads. First the SGEV model was used to model the yearly maxima of snow load, followed by the threshold model. The main results are presented in Table 4.4.

From Figure 4.15b it appears that the variation and magnitude of the yearly max-

Table 4.4: Summary of the different estimated values using the GEV distribution and threshold method at Barents South-East.

	Without snowdrift		With snowdrift	
	GEV	Threshold	GEV	Threshold
100-year value (kg/m^2)	74	71	54	48
10 000-year value (kg/m^2)	88	78	102	70
ξ-parameter	-0.16	-0.28	0.077	-0.04
Upper bound (kg/m^2)	100	81	-	162

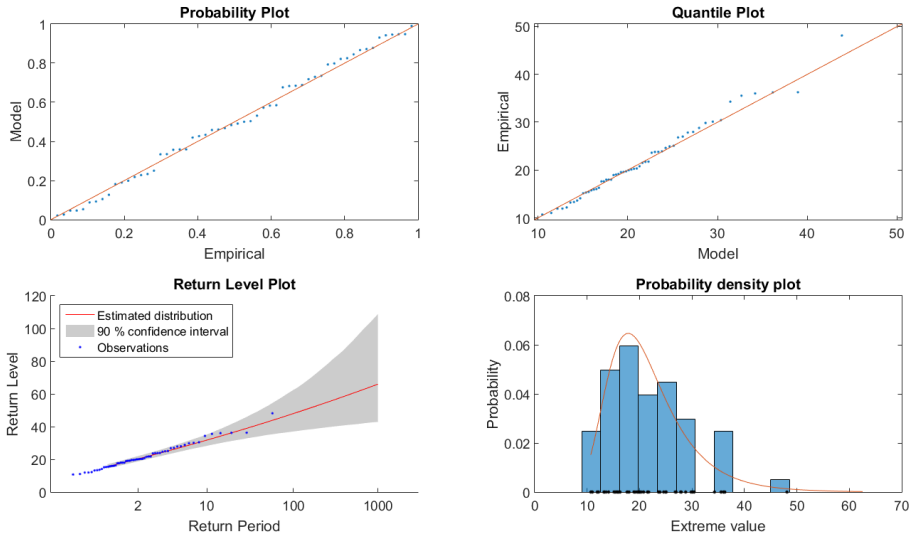

Figure 4.18: Diagnostic plots for GEV fit to the annual maxima snow loads with a drift model at Barents South East.

ima has stayed constant during the period. To test for this, we fitted the data to the four models in Table 3.2. The test showed that there was no significant trend in the distribution, and hence a SGEV is used. Maximization of the log-likelihood yields

$$(\hat{\mu}, \hat{\sigma}, \hat{\xi}) = (19.9, 6.12, 0.077). \tag{4.4}$$

90 % confidence intervals found with a parametric bootstrap method are $(18.74, 21.15)$ for μ, $(5.2, 6.9)$ for σ and $(-0.06, 0.21)$ for ξ. The shape paramter ξ is positive indicating a non-bounded distribution, however the value is so small it is hard to draw a conclusion. Various diagnostic plots are shown in Figure 4.18. The model fits the data well. We can see some deviation between the model and the data at the largest values in the quantile plot. However, when accounting for sampling variability this error is small. Thus the diagnostic plots does not rise any doubt about the validity of the fit.

The 100 and 10 000 year return values for snow load when including snow drift are 53.7 kg/m^2 and 102 kg/m^2. Note the positive ξ value which gives an unbounded distribution, compared to the estimated bounded distribution of extreme snow loads without drift. This causes the 10 000 year return value with snow drift to be larger than without snow drift!

We also used the threshold model to estimate extreme snow loads with wind drift. The declustering algorithm yielded 1512 events with a mean of 5.8 kg/m^2. We used a threshold of 7.8 kg/m^2 (corresponding to the 70th percentile) and fitted the excess to the generalized Pareto distribution. The maximized-loglikelihood estimation of the parameters were

$$(\sigma, \xi) = (7.0, -0.04), \tag{4.5}$$

where σ is in units kg/m^2. The ξ-parameter is negative indicating a bound distribution, in contrast to the fitted SGEV distribution. The parameter value is very close to zero, yielding a high bound on the distribution with a largest possible return level from the fitted distribution of 162 kg/m^2. The 100 and 10 000 year values are 48 kg/m^2 and 70 kg/m^2, respectively.

Meteorological conditions prior to extreme snow events

Wind roses of the wind during the 10 days prior to every yearly maxima is plotted in Figure 4.19. Figure 4.19a and Figure 4.19c shows the wind prior to yearly maxima *without* the drift model at Barents South-East and Johan Castberg respectively, while Figure 4.19b and Figure 4.19d shows the wind prior to yearly maxima *with* the drift model at Barents South-East and Johan Castberg, respectively.

At Barents South-East, direction of the wind before yearly maxima is very different with the snow drift model than without blowing snow. Without snow drift, there is a strong tendency for the winds to blow from north-northeast before the extreme snow events, while the winds come from southeast if we include snow drift. The wind speed is not very different in the two cases; the fraction of high wind speeds (>10 m/s) to lower wind speeds is comparable in the two plots.

At Johan Castberg, the difference between the cases with snow drift and without snow drift is not as large as at Barents South-East. Without wind drift, the wind blows usually from the northeast and there is an insignificant amount of wind coming from the sector between south and west. When using the drift model, the wind blows more often from the south, but the major wind direction is still from the northeast.

The yearly maxima when including drifting snow happens under different conditions as seen in wind-rose plots. To further study this, we investigated in what month the yearly maxima occurred, with the results plotted in Table 4.5. The month to have the most frequent yearly maxima when neglecting snow drift is January and February for Barents South-East and Johan Castberg respectively. When including the effects of snow drift the most frequent month to have a yearly maxima is December and January, for Barents South-East and Johan Castberg, respectively. Without snow drift the yearly maxima occurs in the months December, January and February in 3 of 4 years at Barents South-Easts, and 2 of 3 at Johan Castberg, and no yearly maxima occure between May and November for either station. When including snowdrift, the date of the yearly maxima spread more evenly, and even June has 7 % of the maxima at Barents South-East.

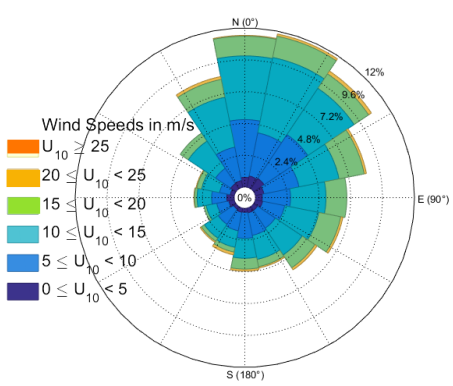

(a) Barents South-East *without* drifting snow

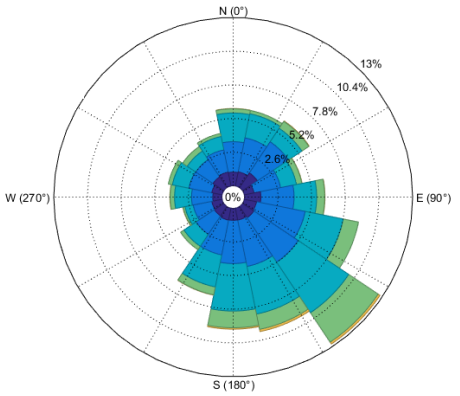

(b) Barents South-East *with* with drifting snow

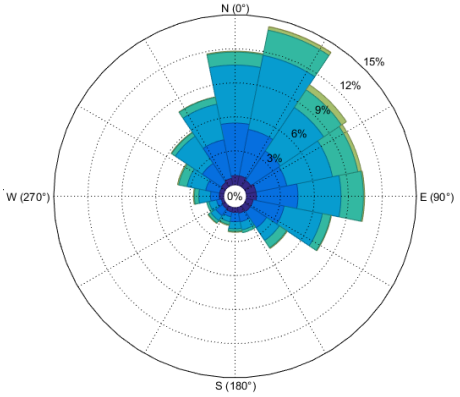

(c) Johan Castberg *without* drifting snow

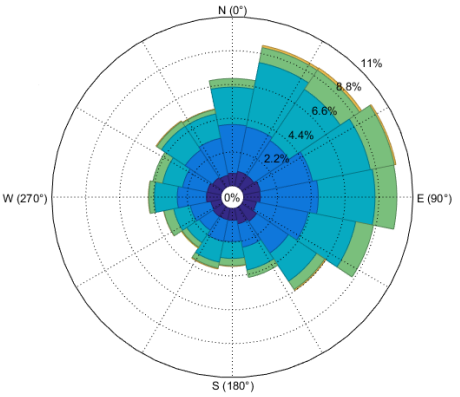

(d) Johan Castberg *with* drifting snow

Figure 4.19: Wind roses of the wind during the 10 day accumulation period prior to each of the yearly maxima at Barents South-East (**a** and **b**) and at Johan Castberg (**c** and **d**). The left column (**a** and **c**) is of the period prior to the yearly maxima without snow drift and the right column (**b** and **d**) shows the wind prior to the yearly maxima when the snow is allowed to drift away. Same scale on the wind speed in all subfigures.

Table 4.5: Frequency of what month the estimated yearly maxima of snow load occur at Barents South East and Johan Castberg. The months not shown in the table has zero yearly maxima.

	Frequency of yearly maxima (%)			
	Barents South-East		Johan Castberg	
	No drift	With drift	No drift	With drift
January	28	14	17	26
February	22	12	28	15
March	12	12	12	21
April	10	7	12	5
May	0	7	0	3
June	0	7	0	0
October	0	12	0	0
November	5	14	10	12
December	22	15	21	17

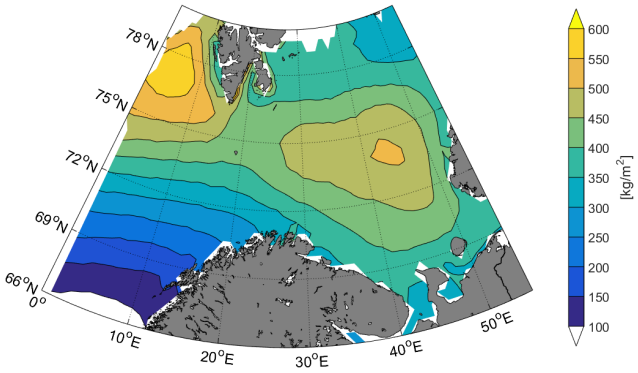

Figure 4.20: Mean yearly snow in the Barents Sea. Data from NORA10 and assuming all precipitation that falls when temperatures are less than 1.5 °C is solid.

4.4 Snow conditions in the Barents Sea

A threshold temperature for precipitation to fall as snow of 1.5 °C was used on precipitation from NORA10. Mean annual snowfall from this is plotted in Figure 4.20. The annual snow loads are highest in the eastern part of the Barents Sea and on the off the west coast of Svalbard. Even though there is more precipitation at lower latitudes as seen in Figure 3.1, the temperatures are lower further north, leading to a higher solid-to-liquid ratio of precipitation. Thus, the largest snow loads are in the area with the right combination of high precipitation and low temperatures.

Time series of snow loads were calculated with the 10-day snowfall model on a grid with resolution 0.5° by 1° in latitude and longitude, respectively[3]. Means of the yearly maximum snow loads are plotted in Figure 4.21a. The loads show a saddle-

[3]Which corresponds approximately to a 50 km by 35 km gird

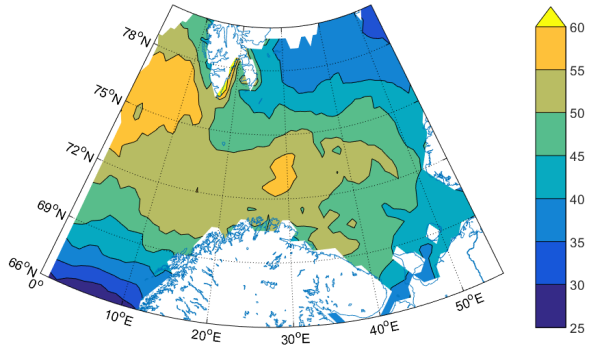

(a) The mean of the yearly maxima snow loads.

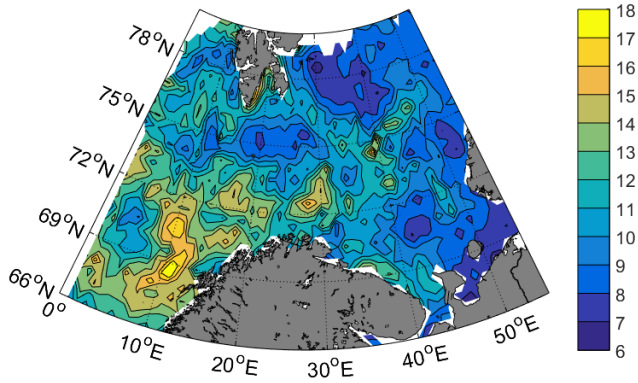

(b) Standard deviation of the yearly maxima

Figure 4.21: The mean (**a**) and standard deviation (**b**) of the yearly maxima calculated by the 10-day snowfall model without snow drift. Values in kg/m^2.

like shape, with lower snow loads in the south and northeast, and higher values in a band going through the middle of the Barents Sea. There are two local maxima with yearly maximum snow loads around 55 kg/m^2, one around 72° N 30° E and the other around 75° N 5° E. The pattern is qualitative similar to the pattern of annual snow fall in Figure 4.20, but the high loads are translated to the southwest.

The standard deviation of the yearly maxima are shown in Figure 4.21b. The spatial pattern of the standard deviation is more chaotic than the mean, but generally the yearly maxima show a northeasterly gradient, with the highest variation in the southwest of the Barents Sea. This is important as it will drive higher return levels in the southern part of the Barents Sea, even though the means of the yearly maxima are relatively low there.

Both the GEV model and the threshold method were used to calculate extreme snow loads at the gridpoints in the Barents Sea and used to produce the contour maps of snow load in Figure 4.22. The threshold model and the GEV model produce very similar results. Except for some points, the difference between the 100-year return

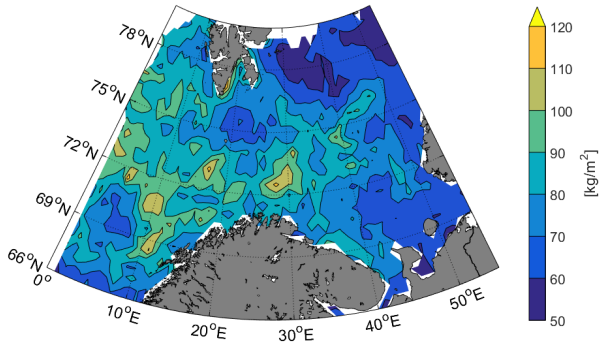

(a) Values from the GEV distribution

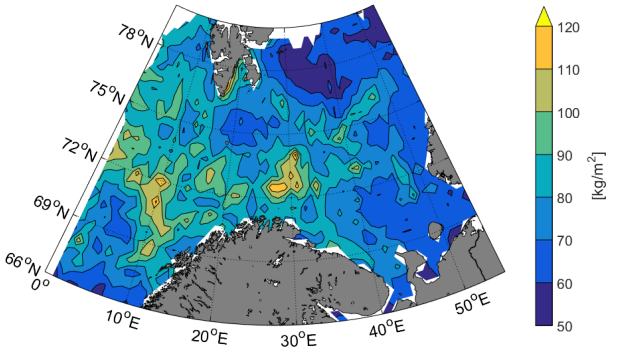

(b) Values from the threshold model

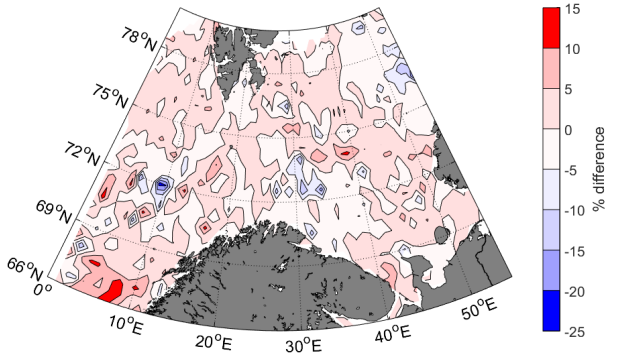

(c) Difference between GEV and threshold.

Figure 4.22: 100-year return values of snow load (kg/m^2) using the GEV distribution (**a**) and the threshold model (**b**). The 10-day snowfall model without snowdrift has been used to create time series of snow load. (**c**) shows how much larger in percent the 100-year values from the GEV method are compared to the threshold method.

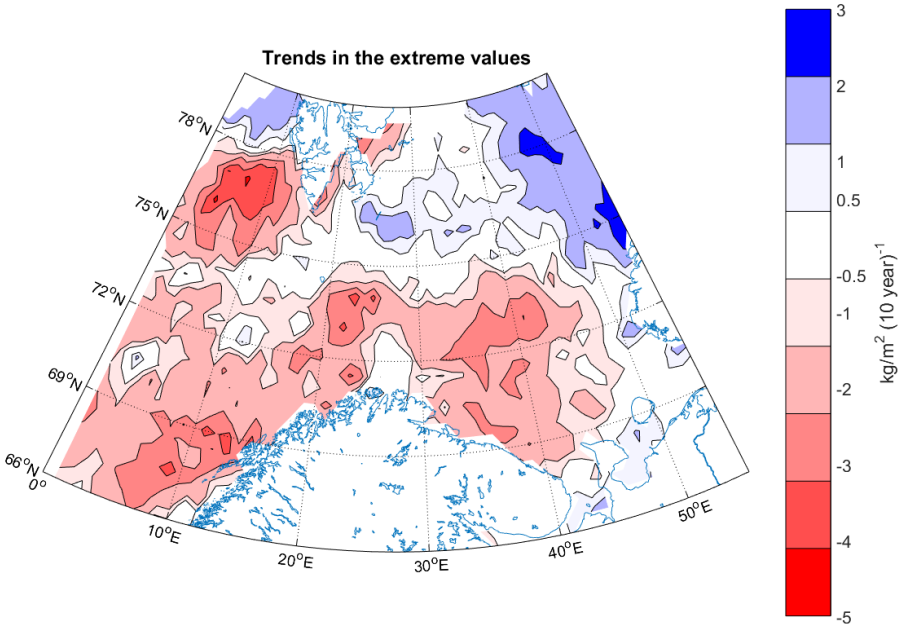

Figure 4.23: Trends in the estimated μ-parameter of the NSGEV model. A linear trend in μ was assumed, and the parameters were then estimated using maximum likelihood. Yearly maxima from the 10-day snowfall model without snow drift

value from the two statistical models is between ± 5 %. The highest 100-year return values of snow load is about 120 kg/m^2 at 72.5° N 28° E and the lowest values are just over 50 kg/m^2 in the area between Svalbard and Franz Josef Land. There is a band of higher loads at 72 °N, with decreasing loads further south. An interesting point is that the lowest values are found up north at 76 °N off the east coast of Svalbard. This is due to the fact that there is less precipitation in this area resulting in a lower snow load, even though the solid to liquid precipitation rate is higher here. The plot of the 100-year return value shows similar, but not the same, spatial variation as the mean of the yearly maxima. The 100-year return value is also strongly dependent on the variation and skewness of the yearly maxima. Thus, some of the highest extreme snow loads are estimated along the Norwegian coast between 68° N and 72° N, even though the mean of the yearly maxima here are about the same as in the eastern Barents Sea, where the 100-year values are lower.

The northeastern boundary of the area with higher (>90 kg/m^2) 100-year return values follows approximately the position of the ice edge during winter, which extends southwards towards Bjørnøya from the northeast. This is also the location of the Arctic Polar Front between Atlantic and Arctic waters.

Using the methods in Chapter 3.3 we estimated trends in extreme values at every grid point (see Figure 4.23). The southern part of the Barents Sea has seen a decrease in the location parameter of the GEV distribution of around -3 to -5 kg/m^2 per decade.

This corresponds to about a 20 % to 30 % decrease in return levels during the investigated period (1957 to 2015). Also, an area on the west coast of Svalbard has seen a very large decrease in return values during the period of -4 to -5 kg/m^2 per decade. In the northern part, east of Svalbard, the trends have been flat or slightly increasing. Areas with the largest return values have also seen the largest decrease in the μ parameter.

Figure 4.24 shows wind roses of the wind during the 10 days prior to the yearly maxima, both without the snow drift model and with the snow drift model. Without snow drift, the wind shows a strong tendency to come from the north to northeast prior to a yearly maximum west of 35° E. East of 35° E there are some events for which the wind blows from the south, but the east-west component is still small. In the days prior to a yearly maximum when using the snow drift model, the northern component of the wind is very much reduced. Instead the wind blows mainly from the east in the area west of 35° E, but with a southerly component. In the southwestern parts of the Barents Sea, the winds almost never blows from the south prior to a yearly maxima either with or without snow drift, and the direction of the wind is very similar.

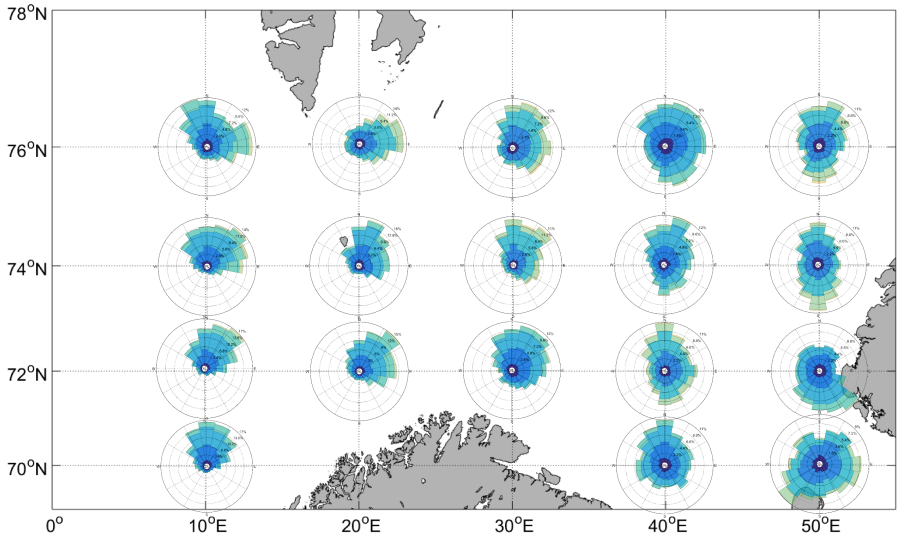

(a) No wind drift

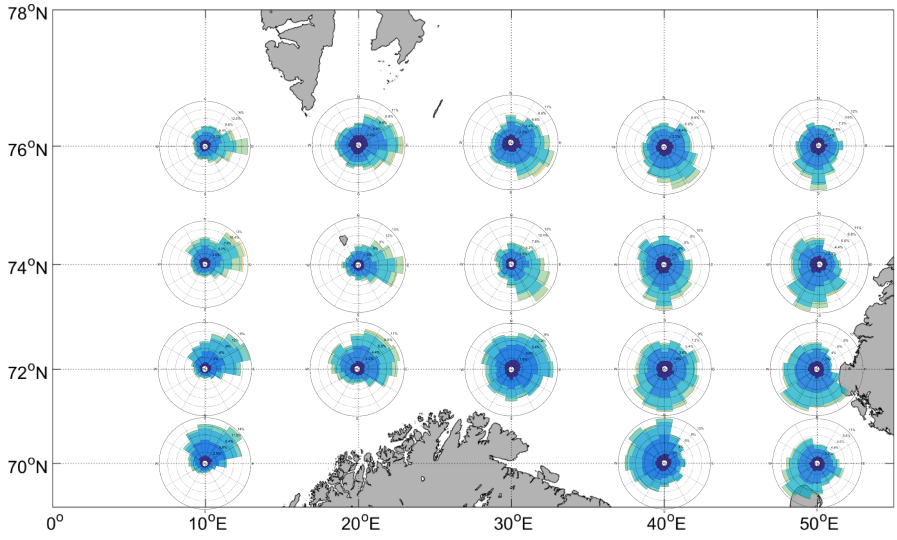

(b) With wind drift

Figure 4.24: Wind roses of the wind 10 days prior to the yearly maximum snow loads estimated by the 10-day snowfall model without snow drift (**a**) and with snow drift (**b**)

5 Discussion

5.1 Uncertainties in meteorological observations

The NORA10 hindcast has been validated against meteorological observation, and it is thus necessary to understand the uncertainties in the observations to properly investigate any bias in the hindcast. There are many difficulties related to meteorological observations in the Arctic. A sparse station network makes correction of inhomogeneities and errors difficult (Nordli et al., 1996), and for example can icing and wet snow cause malfunctioning of measuring equipment. The combination of snow, open tundra and high wind speeds makes precipitation the most difficult weather variable to measure in the Norwegian Arctic (Førland and Hanssen-Bauer, 2002). Drifting snow can impair the measurements, e.g. the gauge at Hopen caught 190 mm of "precipitation" due to drifting snow during three days in January 1995 (Førland et al., 1997). Events purely caused by drifting snow are corrected for through the Norwegian Meteorological Institute's quality control, however during events with a mix of true precipitation and drifting snow it is difficult to distinguish the proportion of precipitation and blowing snow.

Undercatch is another element which introduces errors in the measurements, especially for solid precipitation. Undercatch happens when aerodynamic effects pushes precipitation away from the measuring bucket, and thereby reducing the measured precipitation. The mean values of daily precipitation at Bjørnøya shown in Fig. 4.4 might indicate that the observations have an undercatch of snow; when the precipitation falls as rain, NORA10 matches the observations well, and when the precipitation falls as snow, the mean values of NORA10 shows a wet bias. This is not observed at Fruholmen Fyr, however, here NORA10 shows constant dry bias throughout the year. Hanssen-Bauer et al. (1996) studied undercatch on Svalbard and developed empirical formulas to correct for undercatch, however the formulas are not valid for wind speeds higher than 7 m/s. To estimate possible undercatch in the observations, we instead used the formulation in Wolff et al. (2013), who used experiments from the mountains on the Norwegian mainland to establish formulas to correct for undercatch as a function of wind speed and temperature. The formula fits reasonably well with the undercatch formulas established by Hanssen-Bauer et al. (1996) for wind speeds less than 7 m/s. The formula in Wolff et al. (2013) is valid at least up to 15 to 20 m/s.

The true precipitation is estimated to

$$R_t = R_m \left[\left\{ 0.82 - \frac{0.81e^{\left(\frac{T_a-0.66}{1.07}\right)}}{1+e^{\left(\frac{T_a-0.66}{1.07}\right)}} \right\} e^{-\left(\frac{U_{10}}{4.24}\right)^{1.81}} + \frac{0.81e^{\left(\frac{T_a-0.66}{1.07}\right)}}{1+e^{\left(\frac{T_a-0.66}{1.07}\right)}} + 0.18 \right]^{-1} \tag{5.1}$$

where R_t is assumed true precipitation, R_m is measured precipitation (with undercatch), T_a is air temperature, and U_{10} is the wind speed at 10 m. Mean daily precipitation with corrected values for Hopen, Bjørnøya and Fruholmen fyr are shown in Figure 5.1. The NORA10 hindcast fits the corrected observed precipitation much better at Bjørnøya, however the observations at Hopen and Fruholmen Fyr show a very large winter precipitation. At Fruholmen Fyr the mean temperature during winter is in the range -2 °C to 2 °C, which is the range where precipitation can fall as both snow and rain and are thus prone to the most variation of the undercatch. The correction formulation are based on mean undercatch of observations, and if there are more events with rain falling at low temperature at Fruholmen, the correction formula will overestimate the true precipitation. At Hopen, the winters are colder, and we expect the correction formulas to be better here than at Fruholmen Fyr. Still, the mean winter precipitation is higher for the observations than NORA10. Wind drift accumulating as snow was a known problem at this station, and the precipitation gauge was moved in 1997 to reduce the problem (Hanssen-Bauer, 2016, Personal communication). The precipitation significantly decreased after this, and the hindcast and the corrected observations have similar mean daily precipitation in the period from 1998 to today as seen in Figure 5.2. Time series of yearly mean also shows a jump of 30 % after 1997 compared to before 1997 (not shown). This is reason to believe drifting snow have had an significant affect on winter precipitation at Hopen. The observations still have higher mean than NORA10 in the spring, but values in November and December are very similar.

Without corrections for undercatch, we found in Chapter 4.1 a relatively good agreement between the tail of the 12-hour distribution of NORA10 and the observations. If the observations are corrected for undercatch, the tail of the observed precipitation distribution becomes much thicker with several events higher than 80 mm/12 hours at both Bjørnøya and Hopen. These values are unreasonably high, and can be due to observations having a too large correction factor. This can happen because of rain falling at low temperatures. This was tested for by only looking at precipitation at temperatures lower than -4 °C. Still there was a considerable number of extreme precipitation events. Another source of error is that the 12-hour average temperature and wind speed are not always representative for the conditions during the actual precipitation event.

There is reason to believe there is undercatch of the precipitation measurements at Bjørnøya and Hopen, especially for solid precipitation. Thus, the distribution of observed precipitation shown in Figure 4.3 is probably underestimating the true precipitation. By how much is unclear, as there are several other uncertainties related to measured precipitation which are not easily corrected. Still, if NORA10 fits the uncorrected precipitation data, it is likely that the hindcast has too thin tails of the distribution of precipitation, and possibly underestimate the frequency and magnitude

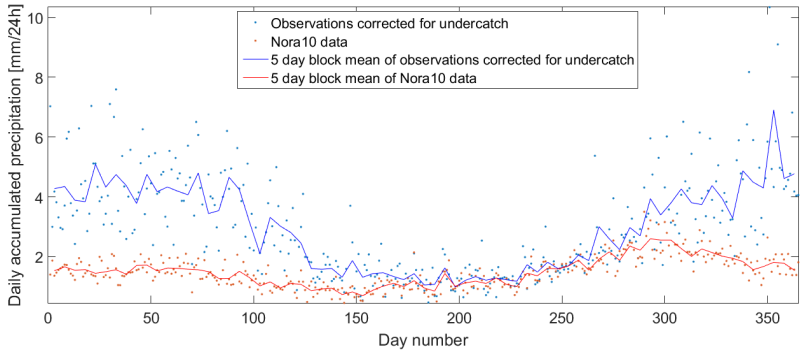

(a) Data from Hopen (1957-2015)

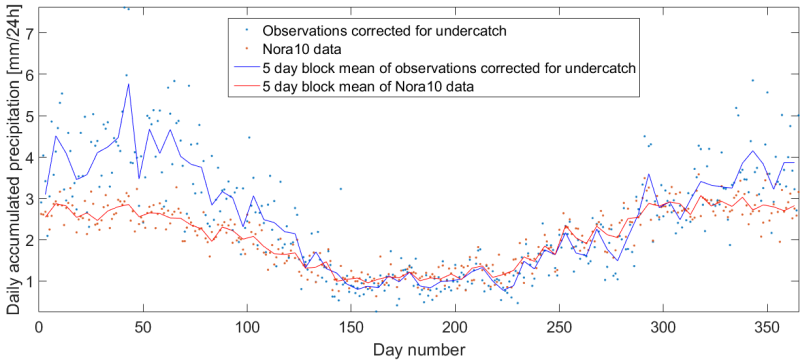

(b) Data from Bjørnøya (1957-2015))

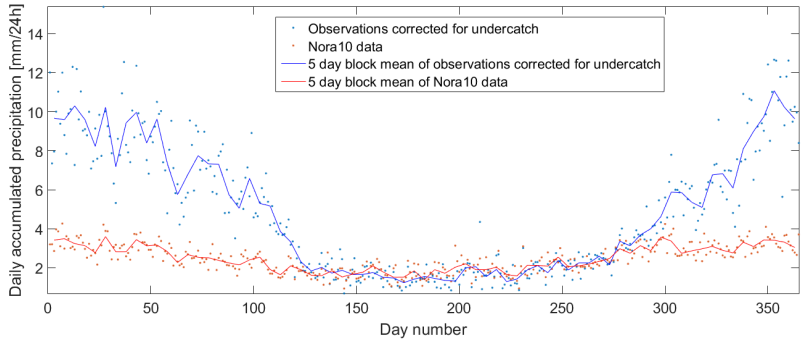

(c) Data from Fruholmen fyr (1957-2005)

Figure 5.1: Mean daily precipitation during the observation period in mm/day corrected with the formulation of Wolff et al. (2013) . Data from Hopen (**a**), Bjørnøya (**b**) and Fruholmen Fyr (**c**) is used.

of extreme events.

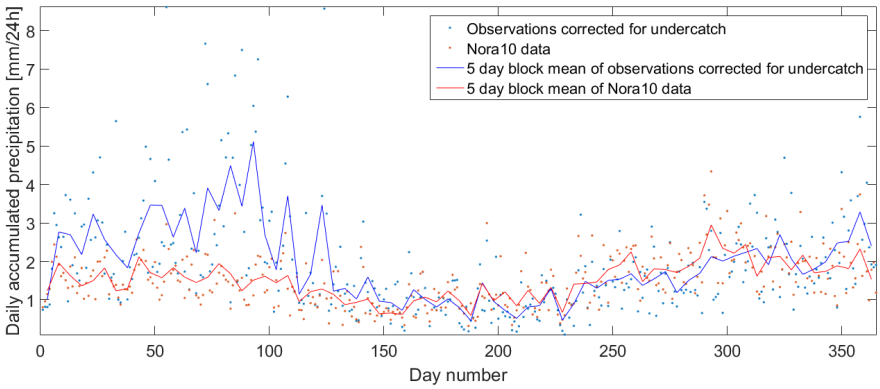

Figure 5.2: Mean daily precipitation from Hopen in the period (1998 2015) in mm/day corrected with the formulation of Wolff et al. (2013)

5.2 Hindcast bias

A scatter plot of the precipitation in NORA10 and the observed precipitation gives an indication of how well NORA10 is able to capture the true precipitation. As seen in Figure 4.1, the hindcast does not do an impressive job at estimating the precipitation in a given time step. The most intense precipitation rates in the observations were only minor events in the hindcast, and vice versa. This also means that the precipitation data from NORA10 is not very well suited to investigate a particular historical snow event. This is not, however, critical when trying to estimate return values; as long as NORA10 displays the same behavior, that is, same variability, magnitude, frequency and statistics of events, as the true conditions, it is still applicable to use data from NORA10 in the analysis.

The histograms in Fig. 4.3 show that the distribution of precipitation is similar for NORA10 and the observations. NORA10 tends to overestimate the proportion of lower precipitation rates (0.5 to 10 mm/12h) and underestimates the proportion of higher precipitation rates. NORA10 also has a higher number of wet days. We have to keep in mind that NORA10 is model data which estimates the precipitation within a grid cell, while the observations are precipitation at a specific point. The precipitation is hence, 'smeared' out in the model, which gives more frequent small precipitation events in NORA10 compared to the observations, but also can underestimate the intensity of high point precipitation.

This continuous precipitation of NORA10 compared to the probable real precipitation on a structure, will bias the calculated snow load and return levels using NORA10. To investigate how large the effect of the wet bias is, we calculated 10-day snowfall sums and 10-day precipitation using observational data and NORA10 to

Table 5.1: Estimated 100-year return values using the SGEV distribution. The 10-day snowfall model was used to estimate snow loads with uncorrected observations (Obs) and NORA10 data as input. All values are in kg/m^2.

	Fruholmen Fyr	Bjørnøya	Hopen
Obs (kg/m^2)	111	62	112
NORA10 (kg/m^2)	83	74	78

estimate 100-year return levels of snow load. Histograms of the 10 day precipitation are shown in Figure 5.3. The observations have a much larger frequency of events in the range 0 mm to 10 mm of 10 days accumulated precipitation at all locations, while NORA10 overestimates the number of events around 15 mm to 40 mm. This can be explained by the high number of low intensity events in NORA10; a continuous rainfall of 2 mm per day will accumulate to 20 mm in 10 days. These values, however, are too small to affect the extreme value distribution and the hindcast can still be applicable to estimate large events as only yearly maxima affect the GEV distribution.

NORA10 underestimates the extreme 10 day precipitation at Hopen and Fruholmen. At Bjørnøya however, the hindcast overestimates the 10 day precipitation. This strongly influences the return levels, which are shown in Table 5.1. The 100-year return levels are about 40 % larger for the observations than NORA10 at Hopen and Fruholmen Fyr while at Bjørnøya the return level for the observations are 16 % smaller than NORA10. This shows how sensitive the extreme values are to both the shape of distribution of the yearly maxima and to the variation. At both Fruholmen Fyr and Hopen, the magnitude of the most extreme events are similar for NORA10 and the observations, except for two outliers in the observations. However, the observed distribution of 10 day precipitation has a flatter tail than the tail of the NORA10 distribution of 10 day precipitation. The result is a much higher 100-year return level from the observations than NORA10 even though they have similar yearly maxima.

This analysis indicates that the distribution of precipitation in NORA10 will underestimate extreme precipitation events, however the uncertainties of observed extreme precipitation are too high to be able to predict how much. This is a reason to be conservative when using the hindcast to estimate extreme snow loads.

5.3 Duration of extreme snow events and choice of accumulation period

As seen in Fig. 4.6, the 15-day snowfall model predicts similar yearly maximum snow loads as the energy balance model; during winters when the energy balance model predicts low snow loads, the x-day snowfall sum also mostly predicts lower snow loads. The choice of accumulation days is important, and the x-day model needs to accumulate snow for over 15 to have similar yearly maxima as the energy balance model predicts. The variation of yearly maxima is however much higher for the energy balance model, and this also leads to much higher estimated 100-year snow load

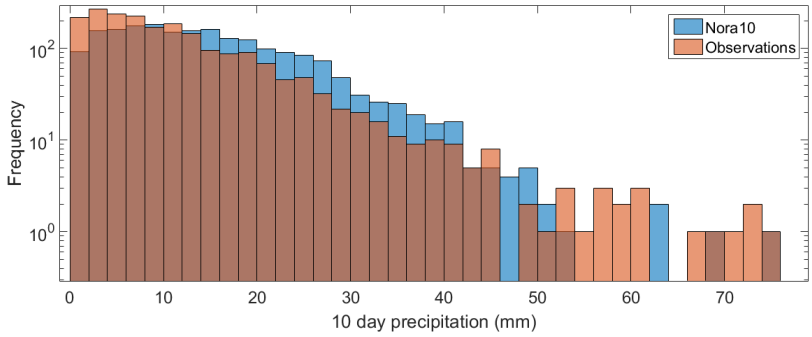

(a) Data from Hopen

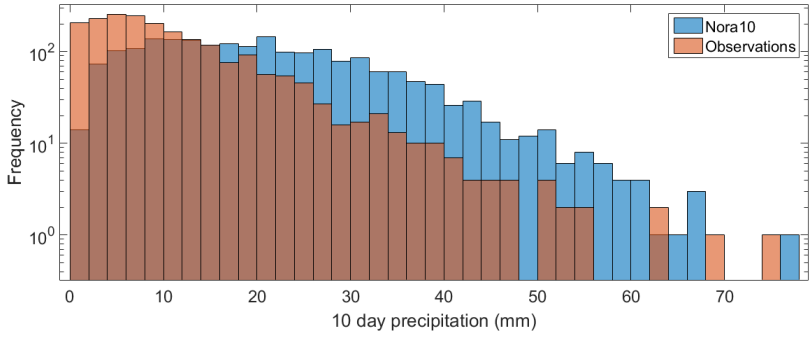

(b) Data from Bjørnøya

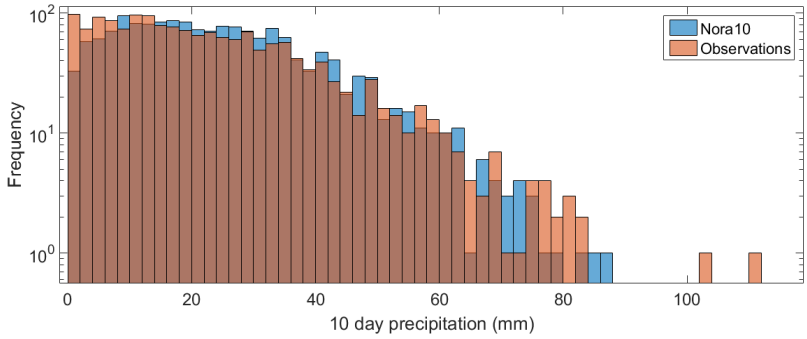

(c) Data from Fruholmen fyr

Figure 5.3: Histogram of 10 day accumulated precipitation at Hopen (**a**), Bjørnøya Meterological station (**b**) and at Fruholmen Fyr (**c**). The y-axis has a logarithmic scale, and the histogram is scaled to show the number of events during the period of study.

(245 kg/m^2 for the energy balance, and 106 kg/m^2 for the 15-day snowfall sum at Johan Castberg). The energy balance model estimate larger snow loads because it does not have an upper limit to the number of days it is possible to accumulate snow, which clearly the x-day snowfall sum has. As an example, if a location has a cold spell with negative temperatures for a month, very little of the snow would melt away. This results in a maximum snow load that would be close to the 30-day snowfall sum. This can be seen in Fig. 4.7a, where many of the most extreme events accumulated over 20 days at Johan Castberg and for over three months at Hopen and Barents South-East.

The real snow loads accumulating on a platform will not be this large because wind will blow away some snow. However, the results show that the conditions in the Barents Sea can allow for extended periods without any significant melting, and snow can accumulate to large loads on sheltered parts of a structure if not moved operationally. Waiting for snow on a shielded roof to melt might not be an option and operational measures should be available to remove snow from these areas. When designing an offshore structure in the Barents Sea, snow accumulation during downtime of snow removing mechanisms should thus be accounted for.

Including the effect of drifting snow has a significant impact on the results. We can see in Fig. 4.7b that the duration of a snow event is drastically reduced when the snow is allowed to drift off the platform. This is expected as the wind drift will only reduce the total amount of snow. The plot suggests that if we include drifting snow, the snow from single storms will be dominating the design loads of a structure, in contrast to accumulation over a month or two. This has the consequence that to be able to accurately estimate the true snow loads in the Barents Sea, any model needs input data which can resolve single storm events, like polar lows.

The yearly maxima from the 5-day snowfall model match well the maxima from the energy balance model with wind drift. The 5-day snowfall model has less variance than the energy balance with wind drift, which makes it underestimate return levels at some locations. This suggests that to be conservative, a 10-day snowfall model can be used to estimate extreme snow loads on exposed parts of a structure, however the wind drift model needs validation in an offshore environment to investigate if the transport rates are accurate.

In this analysis we assumed a flat helicopter deck with no influences from other parts of the structure. This is a non-conservative assumption for total snow loads the the platform as a real structure can have leeward zones like gabble roofs or roofs at different levels, which can accumulate drifting snow. The estimated snow loads from the energy balance model with snow drift will thus only be representative for exposed parts of a structure. In the Norwegian standard NS-EN-1991-1-3 (2008) snowdrift on a step roof can increase the ground snow load four times. The overall snow load will thus be higher than estimated from the energy balance with drift.

It is difficult to recommend an optimal value for number of accumulation days in the x-day snowfall model. On exposed parts of a platform, the extreme snow events can be expected to happen within a few days, and it can be tempting to choose two or three days to accumulate. However, the ability of hindcast data to replicate single events is not very reassuring. Further, wind drift can increase the snow load on shielded parts of a structure, but snow drift will reduce the total load on a structure as

at least some snow will drift off the platform. The data in the present report suggest that choosing a shorter or equal accumulation period than 5 days will underestimate the possible extreme snow loads on a structure. The wind drift model presented in the present report can give some estimates of wind drift on exposed parts of the structure, but validation of the model in an offshore environment is needed before the model can be trusted fully. Because of uncertainties in both the precipitation from the hindcast and the snow drift model, we recommend to use a 10 day accumulation period without drifting snow to estimate possible extreme snow loads.

5.4 Comparison of return values from the SGEV model and the Threshold model

As seen in Figure (4.10, 4.14, 4.16, 4.17), both the SGEV model and the threshold excess model work well and are able to accurately fit the data. The SGEV model shows some deviation from the data at the Barents South-East location, but not enough to throw away the model. In the case of Johan Castberg, the two models display different behavior: The predicted ξ in both models are negative, but ξ is very close to zero in the SGEV model. This implicates that the SGEV model estimates the snow load to be very close to unbounded, while in the threshold model, the snow load is bounded. The estimated 100-year values are almost identical. The difference in 10 000 year values can largely be attributed to different estimates of the ξ parameter. It is hard to tell which model represents the truth most accurately; both models seems to fit the data, however their behavior is quite different. Because the models use different input data (the threshold model uses more events than the SGEV model), it is not straightforward to compare the models using the estimated maximum likelihood.

The negative ξ parameter estimated at Barents South-East and Johan Castberg is also found in the rest of the Barents Sea with the exception of three areas. That the extreme values of snow load are bounded by a maximum possible value is at first thought reasonable. However, both theoretical studies (Koutsoyiannis, 2004), and studies of observed precipitation (Koutsoyiannis, 2004; Papalexiou and Koutsoyiannis, 2013; Serinaldi and Kilsby, 2014) indicates that daily extreme precipitation follows an unbounded distribution, that is $\xi \geq 0$. No such studies have been done for longer precipitation periods like 10 days precipitation, but the tail should be thinner (smaller ξ) than for 1 day precipitation.

Comparing the 100-year values in the Barents Sea from the SGEV model and the threshold model in Figure 4.22, we can see that the values are very similar. This suggests that the time period of 58 years is sufficient to estimate the return values, and the extra data points used by the threshold model does not change the results significantly.

The advantage of the threshold model is that we can use more of the data available than only the yearly maxima. In these two case studies, 166 and 160 of the events were over the selected threshold and used in the further analysis at Barents South East and Johan Castberg respectively, compared to 59 yearly maxima using the GEV model. This can be especially valuable if only shorter time series are available. However,

declustering events and selecting a threshold can lead to unknown biases which are not easily diagnosable. This is not an issue when using the GEV model, and it can be easier to set up automated routines to do the statistical analysis.

Consequences of including snow drift

As seen in Figure 4.15, including a simple empirical formula for snow drift significantly decreases the snow load, and also the 100-year return value is reduced. Interestingly, the estimated 10 000 year return value is larger using the yearly maxima of snow load with drift, than without drift. This is due to the different shape parameter, $\xi = 0.087$ using snow drift, and $\xi = -0.16$ without snow drift, which leads to an unbounded distribution and a bounded distribution, respectively. The difference should not be viewed as a weakness of the GEV-model, but rather as part of the uncertainties when extrapolating to long return periods.

As discussed in Chapter 3.2.3, there is no universal empirical formula for transport rate of snow drift, and the current models yield very different rates for a given wind speed. There is no field data of snow drift transport rate in an marine environment, which makes validation of the formula difficult. The snow loads estimated for the helicopter deck, and with the drift model in general, are only representative for very exposed parts of a platform.

The prevailing wind direction leading up to a yearly maximum snow load without snow drift is from north-northeast. When including snow drift the prevailing wind direction is from the southeast, associated with warmer air from the south. Because wet snow does not drift in the model, it is expected that temperatures around 0 °C is favorable to accumulate snow in the drifting model. This is seen as the mean temperature in the 10 days before a yearly maximum is -5.0 °C without snow drift and only -0.3 °C with snow drift. This means that probably a large part of the snow loads with the wind drift model turned on is wet snow. Wet snow can stick to vertical surfaces, effectively increasing the area of snow accretion. Appendix B presents a short study on wet snow in the Barents Sea. With the wind drift model turned on, the yearly maxima are much more dependent on single storms lasting a couple of days than continuous accumulation over a longer period as seen in Chapter 4.2. This has the consequence that the yearly maxima can occur in every month from October to June, compared to the yearly maxima without snow drift which only occur in November through April, with a majority in December to February.

5.5 Extreme snow loads in the Barents Sea

Fig. 4.22 shows that the estimated 100-year snow load in the part of the Barents Sea that is opened for petroleum activity is higher than 70 kg/m^2, which corresponds to a total load of 63 ton on a 30 m helicopter deck. The maximum estimated 100-year snow load in the Barents Sea is 127 kg/m^2 using the SGEV model, and is located at 72.5° N, 28° E, which is about half way between mainland Norway and Svalbard and inside the area opened for petroleum activity. Both the SGEV model and the

threshold model estimate very similar return values, both in magnitude and spatial pattern, which increases our trust in the results. However, the return values from the extreme value distributions are only as accurate as the input time series of snow load. We note that the 100-year snow loads estimated using observed precipitation and temperature were much higher at Fruholmen Fyr and Hopen, but lower at Bjørnøya, than 100-year snow loads estimated using the NORA10 hindcast, which can indicate that extreme values estimated using the NORA10 hindcast may be non-conservative..

The mean yearly precipitation in the Barents Sea is on average around 700 to 1000 mm w.e., a large fraction of this is snow. The amount of precipitation decreases closer to, and north of the ice edge. This results in a maximum of mean yearly snow in the middle to eastern part of the Barents Sea, where the balance between cold temperatures yielding a higher fraction of solid-to-wet precipitation and amount of total precipitation is optimal. Interestingly, the 100 year return values are also very high further south along the Norwegian coast, where the mean of the yearly maxima is smaller. This is because the variation is much higher here, with some years having very high snow loads, while others barely have snow at all. This will lead to a thicker tail of the SGEV distribution, increasing the estimates of return values.

The contour maps show a large spatial variation of the calculated extreme snow loads which are present using both types of extreme value models. The fact that the 100-year snow load is varying 50 % within a couple of tens of km does not seem reasonable. A very high value (> 0.3) of the estimated ξ-parameter, indicating an unbounded distribution, is common for the very high extreme snow loads. This shows some of the difficulties encountered when extrapolating extreme values; slight changes of the input data can yield notably different results. In the case of e.g. Johan Castberg, we can see that the estimated 100-year snow load at the location is 85 kg/m^2, while 120 km to the west the estimated 100-year snow load is 126 kg/m^2. The mean yearly maxima is however very similar at the two locations (see Fig. 4.21a). The main reason for the difference in extreme values is therefore less variation in the yearly maxima at the location of Johan Castberg and a different estimated shape parameter. This shows that investigations of snow loads at a specific location should study multiple grid points in the vicinity of the desired location.

5.6 Cause of decreasing extreme snow loads in the Barents Sea

Trying four different models at the Johan Castberg location, we found that a NSGEV with a μ parameter varying linearly with time explained most of the variance in the data. The negative slope indicates that the extreme values have decreased in the observation period, which can have numerous complex and coupled explanations, however with the simple 10-day snowfall model it is reduced to less precipitation within 10 days and fewer days under 1.5 °C. To explain why the yearly snow loads have declined, correlation between the yearly maximum snow load and four selected proxies were studied. The parameters of interest were the sum of winter precipitation, the number of 3-hour intervals with precipitation larger than 3 mm during the winter,

the mean of the winter temperature and the number of days with temperatures below 1.5 °C. A winter is defined as the time between November 1 and May 1, which is the time period when all winter maxima were observed without wind drift. Correlation plots between all the parameters are found in Figure 5.4. The figure shows that the yearly maximum snow load shows the strongest correlation with the sum of winter precipitation, with a correlation coefficient of 0.47. The yearly snow load also shows some correlation with temperature, both with mean temperature (-0.37) and number of days with temperatures under 1.5 °C (0.41). Interestingly, the sum of winter precipitation does not correlate with mean winter temperatures.

At the Johan Castberg location, the 2 m temperature in NORA10 has a linear trend of +0.2 °C per decade. This has further decreased the yearly number of days with temperatures below 1.5 °C by an average of 8 days per decade. In Figure 5.4 there is a weak correlation between the yearly number of days with temperatures below 1.5 °C and the maximum snow load in the same year. This indicates that part of the reduced snow load can be explained by a decreased number of cold days due to an increase in air temperatures. There is also a correlation between both the sum of total winter precipitation and number of large precipitation events with maximum yearly snow load. However, the precipitation does not show any trends during the time studied, and a decrease in precipitation is thus not a probable explanation of the reduced extreme snow loads at the Johan Castberg locations.

The decreasing trend at Johan Castberg is also found throughout the southern parts of the Barents Sea. The estimated trend in the μ parameter in Figure 4.23 shows a decrease of the return levels in the southern Barents Sea of around 2 to 4 kg/m^2 per decade . This decrease in extreme snow loads does not come from increasing temperatures alone; the highest temperature increase is in the northern Barents Sea (not shown) and a much slower temperature increase further south. This is opposite of the trend in extreme snow loads. However, further north in the Barents Sea, the air temperatures are much colder than 0 °C most of the year, and an increased temperature from, e.g. -10 °C to -8 °C will not have a large impact on the amount of snow. An increase from 0 °C to 2 °C will have a more profound effect. A better proxy for the decreasing trend in extreme snow loads is the number of days in a season with daily temperatures below 1.5 °C. This trend matches much closer the spatial trend in snow loads as seen in Figure 5.5a. As seen earlier, there was a correlation between the yearly maxima and the number of days with sub-zero temperatures at Johan Castberg. With further increase in temperatures, and thereby less days with possibility of solid precipitation, a decrease in snow loads can be expected.

The northern parts of the Barents Sea has seen a large decrease in the number of days with temperatures below 1.5 °C without having a decrease in extreme snow loads, which indicates other mechanisms are also driving the extreme snow loads. At Johan Castberg we showed a correlation between the winter precipitation and extreme snow load. An area southwest of Svalbard and an area south of 74° N and east of 20° E has seen a decrease in winter precipitation of around -1 to -2 mm/year as seen in Figure 5.5b. The decrease in extreme snow loads can thus probably be related to a change in precipitation in addition to fewer days with sub-zero temperatures. It is important to note that the trends here are based on NORA10. Observational precipita-

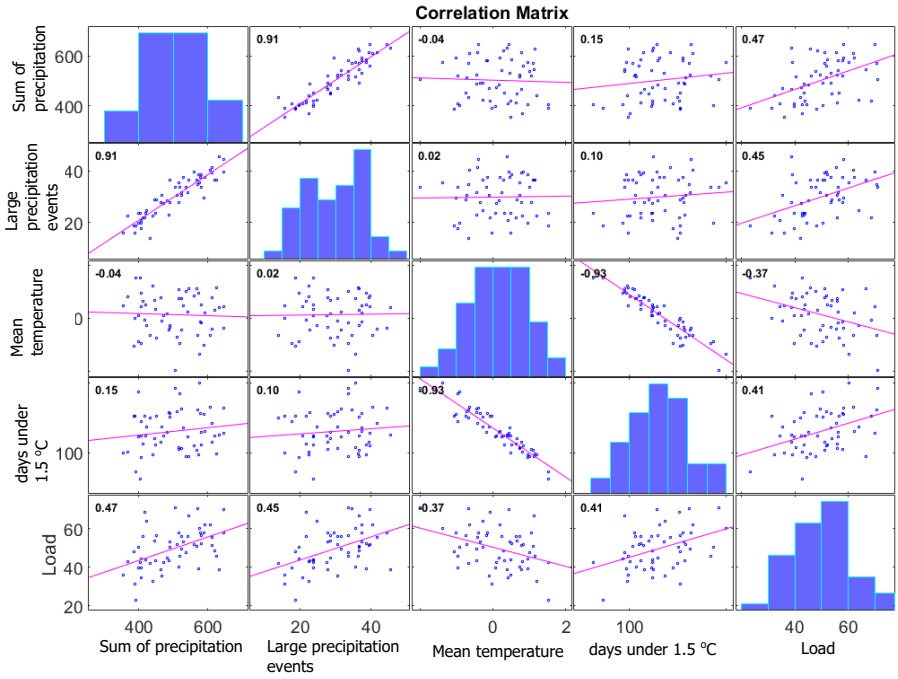

Figure 5.4: Correlation between different parameters at the Johan Castberg location. Sum of precipitation is the the sum of winter precipitation, large precipitation events is the number of time steps with precipitation larger than 3 mm, mean temperature is the mean winter temperature, days under 1.5 °C is the number of days with temperatures below 1.5 °C and Load is the yearly maximum snow load calculated with the 10-day snowfall model

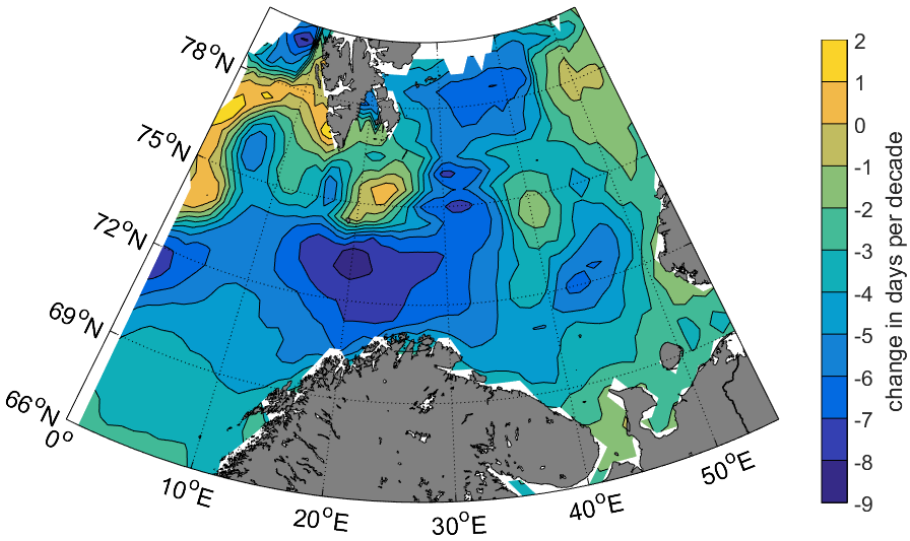

(a) Linear trend in number of days with cold temperatures

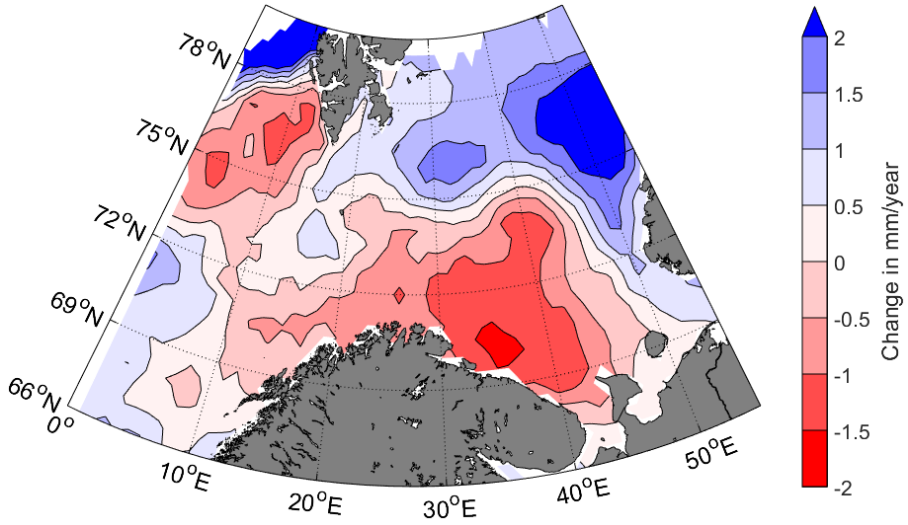

(b) Linear trend in winter precipitation

Figure 5.5: Linear trend in number of days with air temperature below 1.5 °C in (**a**) and linear trend in the winter precipitation (accumulated precipitation from November 1st to May 1st) in (**b**).

tion has been found to increase in the period at Bjørnøya when NORA10 estimated an increase in precipitation. An increasing trend in precipitation has also been observed at meteorological stations on Svalbard (Førland et al., 1997; Førland and Hanssen-Bauer, 2000) and models have predicted an increase in winter precipitation over the Arctic due to higher atmospheric vapor content and poleward water transport due to increasing air temperatures (Serreze et al., 2000). It is not clear how the combination of increasing temperatures (lower solid to liquid fraction of precipitation) and more precipitation will affect extreme snow loads. Depending on the relative magnitude of the trends, both increasing or decreasing snow loads can be expected in different regions.

5.7 Uncertainties in the snow model

Even assuming the meteorological data are correct there are some simplifications and uncertainties in the snow model. The energy balance melt model is pieced together from a parameterization to model the energy flux of the Arctic Ocean. Different parameterizations lead to different estimated heat flux. In a study of 90 different parameterizations, Simonsen and Haugan (1996) found the total yearly heat loss of the Barents sea in the range from 42 to 162 TW based on identical climatological data. Another concern is that the turbulent heat fluxes are bulk formulas which assumes a very large snow surface. In reality, can turbulence induced by the offshore structure lead to a higher sensible and latent heat flux than estimated by the chosen parameterization. This is however a problem dependent on the geometry of the structure and is hence neglected in this study in favor of more general results. Measurements of heat fluxes from a snow pack on an offshore structure are not available in the literature, which makes it currently impossible to validate any parameterization of heat fluxes without further field studies.

Sensitivity of snow loads to assumed threshold temperature for solid precipitation

In the snow model, a threshold temperature decides if the precipitation falls as snow or rain. Rain-on-snow events, which can both add weight and melt the snow pack, are ignored as mentioned in the theory. To estimate how sensitive the extreme snow loads are to the choice of threshold temperature, we estimated 100-year values in the Barents Sea for a range of threshold temperatures, $T_t = (0,\ 0.5,\ 1.5,\ 2.0)$ using the 10-day snowfall model without snowdrift. The mean difference in 100-year value of using a threshold temperature of 0 °C and 2.0 °C was 16 %, however there is a strong spatial pattern. In the area east of 20° E, the 100-year return levels are much less sensitive to the threshold snow temperature, with a mean difference of 11 %. This shows that most of the analysis in the present study is not very sensitive the the choice of the selected threshold temperature, however, further south along the Norwegian coast the 100-year values are more sensitive to when precipitation falls as snow or rain due to air temperatures during winter often vary around 0 °C. In these areas a

more sophisticated model which accounts for atmospheric conditions should be used to select precipitation events as liquid or solid.

Sensitivity of snow driftability assumptions

Snow drift is only possible if the wind speed is over the threshold wind speed, which depends on the properties of the snow. In the model in the present study, a single threshold wind speed of 4.5 m/s is used. Empirical investigations have found a majority of threshold wind speeds in the range 4 m/s to 11 m/s for dry snow (Li and Pomeroy, 1997). We therefore estimated extreme snow loads with a 10-day snowfall model including snow drift, but with five different threshold wind speeds of $(4.0,\ 6.0,\ 8.0,\ 10,\ 11)$ m/s. The results showed that the 100-year return level changed very little: The maximum 100-year return level was around 7 % higher than the minimum 100- year return level. This is not a surprise as high wind speeds are frequent in the Barents Sea, e.g. at Johan Castberg, NORA10 estimates wind speed above 11 m/s in 20 % of the model time steps. Lowering the threshold wind speed from 11 m/s to 4.5 m/s will result in more time intervals where the snow can drift, but as seen in Equation 3.10, a doubling of the wind speed leads to a 14-fold increase in transport rate. So even if lowering the threshold wind speed increases the number of time intervals in which the snow pack can drift, the snow transport during these intervals is small.

The snow is allowed to drift for 3 days in the present study. To estimate the sensitivity of extreme snow loads to this assumption, we calculated 100-year return levels with the snow allowed to drift in 1 day and 10 days. The results showed a marginal impact on return levels. The 100-year return levels using drift in 1 day were around 2 % higher than return levels were the snow is allowed to drift for 10 days.

The snow drift model also assumes that the snow pack is unable to drift if the air temperatures exceeds 0 °C. In reality, snow drift at higher temperatures is possible, DeGaetano and O'Rourke (2004) found around 1 % of drifting events occurred with air temperatures over 0 °C. Because of high cohesive forces the threshold wind speed will be higher for this wet snow, and the transport rate will probably be affected. However, as seen in the last paragraph, the return levels are not too affected by threshold wind speed, and there is no data available to estimate the transport rate in a wet cohesion regime. We therefore assumed a constant threshold speed of 4.5 °C and the transport rate in Equation 3.10 as before and estimated 100-year snow loads using the 10-day snowfall model including wind drift, but varied the temperature at which drift can occur from 0 °C to 5 °C. This shows that the return levels are more sensitive to change in temperature than threshold wind speed; changing the temperature from 0 °C to 1.5 °C, yields a decrease of 50 % to 70 % of the 100-year return value. For higher lock-off temperatures, the return levels stays around the same level as 1.5 °C. The decrease from 0 °C to 1.5 °C can be explained by that precipitation falls as snow below 1.5 °C. Thus, when selecting a lower lock-off temperature, snow can accumulate without a chance of blowing off, which significantly increases the snow loads.

6 Conclusions and further work

The snow conditions in the Barents Sea have been studied, with emphasis on extreme snow loads on offshore structures to develop recommendations for design loads. Snow loads offshore are largely unquantified, even though accumulated snow will add weight to a platform, can reduce stability, block equipment and valves, and reduce operability of the structure. The present study aimed to

- Estimate 100-year snow loads for the entire Barents Sea
- Characterize how quickly extreme snow loads accumulate in order to select a long enough accumulation period for the x-day snowfall model.
- Investigate if the hindcast archive NORA10 is applicable to estimate extreme snow loads offshore.

Time series of snow load for the entire Barents Sea were found by using a 10-day snowfall model with precipitation and temperature from NORA10 as input. With the use of two extreme statistics models we found 100-year return levels of snow loads. Large variation in the 100-year return levels were found. The area opened to petroleum activity has the largest return levels which are between 70 kg/m^2 (0.68 kPa) and 120 kg/m^2 (1.17 kPa). This is 40 % to 140 % higher than the current recommended value (0.5 kPa) in NORSOK (NORSOK N-003, 2007), which based the snow load on a 2-day accumulation period. Further north in the Barents Sea the extreme snow loads are as low as 50 kg/m^2 (0.49 kPa) to 60 kg/m^2 (0.59 kPa) because of less precipitation, even though the solid-to-wet ratio of precipitation type is higher. There is also large variations in the estimated 100-year return levels over relatively short distances which shows that future studies of snow conditions at a specific location should check several NORA10 grid points in a larger area. This is further supported by the fact that NORA10 underestimates 100-year return levels of 10-day snowfall compared to observed 10-day snowfall at Fruholmen and Hopen, but slightly overestimates the return levels at Bjørnøya.

The estimated snow loads using a 10-day snowfall model should be looked at as operational snow loads where snow is actively removed off the platform by personnel and wind drift. As seen when using an energy balance model to estimate snow loads, there is very little melting during the winter in the Barents Sea, and if not artificially removed, snow loads on sheltered parts of a structure can accumulate over several weeks or months. The snow load on exposed parts of a platform is significantly reduced by wind drift. A 5-day snowfall model estimates similar yearly maximum snow

loads as the energy balance with drift, which are representative for exposed parts of a structure. However, due to the possibility of NORA10 underestimating extreme precipitation events, a longer accumulation period should be used.

Two methods to calculate extreme values have been implemented; using block maxima to fit the stationary generalized extreme value distribution (SGEV) and using the generalized Pareto distribution to model threshold excess. Both methods yield similar results, but the SGEV-model is simpler and by utilizing yearly maxima we do not have to worry about variables being dependent. The threshold model can have an advantage if the data available do not span enough years to make meaningful inferences using the GEV-model, as the threshold model can make use of more than only block maxima. However, if the data is dependent on short time scales, which is the case of snow loads, a declustering algorithm is needed to select independent events. This declustering can lead to unknown biases which are not easily diagnosable.

A non-stationary GEV (NSGEV) model was used to investigate any trends in the extreme snow loads, which is the first time this methodology has been used on snow in an offshore environment. The study assumed linear trends in the location parameter of the GEV distribution, and found that the extreme snow loads in the southern part of the Barents Sea has decreased by around 3 to 5 kg/m^2 per decade, which corresponds to a 20 % to 30 % decrease in 100-year return level of snow load from the beginning of the period of study (1957) to the end (2015). We found that this decrease can be related to increasing temperatures, which has decreased the number of days with temperatures below 1.5 °C by around 8 days per decade in the region around Johan Castberg, and also a decreasing trend in winter precipitation. The results should be looked at with care, as the trends are based on data from NORA10 and both observational evidence and model simulations have shown increasing precipitation in the Arctic while NORA10 shows decreasing precipitation.

We have used the hindcast archive NORA10 (Reistad et al., 2011) for key input meteorological data as there is a sparse network of meteorological stations in the Arctic. The uncertainty in hindcast precipitation is not well understood even though it is common to use hindcasts to investigate precipitation offshore (Syversen et al., 2015). To investigate this uncertainty, a comparison with observations at Fruholmen Fyr, Bjørnøya and Hopen was done.

We found that time series of precipitation from the NORA10 hindcast do not match the time series from the observations, and thus, the hindcast cannot be used to study a particular historical event. The hindcast also has a higher number of wet days, but this does not affect the extreme 10-day precipitation much, which has a similar distribution in NORA10 and the observations. The combination of undercatch and blowing snow, however, makes the observed precipitation uncertain. Correcting for undercatch makes the tail of the observed precipitation distribution thicker, which will increase the extreme values compared to NORA10. Thus, it is probable that NORA10 underestimates extreme precipitation, but an investigation in how blowing snow affects the observations at Bjørnøya and Hopen is necessary to make definite conclusions.

The main concern throughout the present study is how accurate the precipitation from the NORA10 hindcast is. We have investigated this based on comparison with

standard meteorological observations, but the uncertainties of these are poorly quantified. This shows the importance of new offshore field data. Further studies should especially examine how undercatch and wind drift affects observation of extreme precipitation at the Arctic stations of Bjørnøya and Hopen. Controlled precipitation measurements and snow observations from offshore structures would also contribute with very valuable information. Snow transport offshore by blowing snow is another poorly understood mechanism which requires more data to better understand the limitations of the current model and provide validation for new, more complex models.

Snow loads offshore in the Barents Sea have not been granted much attention in the open literature and records of snow events on offshore structures have not been systematically collected over time. Based on NORA10 hindcast data, the present study has established a regional picture of design snow loads in the Barents Sea which can be valuable for planning of new field developments in the region. We have also shown that users of the NORA10 should be aware of a wet bias in the hindcast, and a possible underestimation of extreme precipitation.

7 Acknowledgements

I would especially like to thank my supervisor Sigurd Henrik Teigen at Statoil for his help and guidance throughout the entire work on this thesis. Also thanks to Jon Andreas Støvneng at NTNU for practical arrangement and administrative support during the thesis. Eirik Schrøder Hansen at Statoil deserves thanks for fruitful discussions on extreme value statistics and bootstrapping methods and general feedback throughout this thesis, and thanks to Kenneth Eik from Statoil for providing information on the new NORSOK standard under development. I would likewise like to thank the Norwegian Meteorological Institute (MET) for providing the excellent database of meteorological observations at eKlima. Magnar Reistad from MET deserves thanks for being very helpful and providing extra parameters from NORA10. Finally I would like to thank Inger Hanssen-Bauer, from MET, for thoughtfully answering questions regarding her paper and undercatch of observed precipitation.

Bibliography

Akaike, H., 1974. A new look at the statistical model identification. Automatic Control, IEEE Transactions on 19 (6), 716–723.

Beguería, S., Angulo-Martínez, M., Vicente-Serrano, S. M., López-Moreno, J. I., El-Kenawy, A., 2011. Assessing trends in extreme precipitation events intensity and magnitude using non-stationary peaks-over-threshold analysis: a case study in northeast Spain from 1930 to 2006. International Journal of Climatology 31 (14), 2102–2114.

Budd, W., Dingle, W., Radok, U., 1966. The byrd snow drift project: outline and basic results. Studies in Antarctic Meteorology, 71–134.

Changnon, D., Changnon, S. A., 2007. Snowstorm Dimensions Across the Central and Eastern United States. Physical Geography 28 (3), 218–232.
URL http://www.tandfonline.com/doi/abs/10.2747/0272-3646.28.3.218

Coles, S., 2001. An introduction to statistical modeling of extreme values. Vol. 208. Springer.

Cooley, D., 2009. Extreme value analysis and the study of climate change. Climatic change 97 (1-2), 77–83.

Dee, D. P., Uppala, S., Simmons, A., Berrisford, P., Poli, P., Kobayashi, S., Andrae, U., Balmaseda, M., Balsamo, G., Bauer, P., et al., 2011. The ERA-Interim reanalysis: Configuration and performance of the data assimilation system. Quarterly Journal of the Royal Meteorological Society 137 (656), 553–597.

DeGaetano, A. T., O'Rourke, M. J., 2004. A climatological measure of extreme snowdrift loading on building roofs. Journal of applied meteorology 43 (1), 134–144.

Eik, K. J., February 2016. Representative from Statoil working with the development of the new NORSOK standard. Personal communication.

eKlima, 2016. Climate database for all present and past weather stations of the Norwegian Meteorological Institute. [Online; accessed: April 2016].
URL eklima.met.no

Engineering Toolbox, 2016. [Online; accessed April 2016].
URL http://www.engineeringtoolbox.com/

Førland, E., Hanssen-Bauer, I., 2002. Climate variations and implications for precipitation types in the Norwegian Arctic. Norwegian Meteorological Institute Report Number 24/2002.
URL http://met.no/Forskning/Publikasjoner/MET_report/2002/filestore/klima-02-24.pdf

Førland, E., Hanssen-Bauer, I., Nordli, P., 1997. Climate statistics and longterm series of temperature and precipitation at Svalbard and Jan Mayen. Norwegian Meteorological Institute Report number 21/1997.

Førland, E. J., Hanssen-Bauer, I., 2000. Increased precipitation in the Norwegian Arctic: True or false? Climatic Change 46 (4), 485–509.

Gautier, D. L., Bird, K. J., Charpentier, R. R., Grantz, A., Houseknecht, D. W., Klett, T. R., Moore, T. E., Pitman, J. K., Schenk, C. J., Schuenemeyer, J. H., et al., 2009. Assessment of undiscovered oil and gas in the Arctic. Science 324 (5931), 1175–1179.

Gill, A. E., 1982. Atmosphere-ocean dynamics. Vol. 30. Academic press.

Hamilton, C. D., Kovacs, K. M., Lydersen, C., 2015. Year-round haul-out behaviour of male walruses Odobenus rosmarus in the Northern Barents Sea. Mar Ecol Prog Ser 519, 251–263.
URL http://www.int-res.com/abstracts/meps/v519/p251-263/

Hansen, E. S., Teigen, S. H., 2015. An efficient numerical model for marine icing. In: Proceedings of the International Conference on Port and Ocean Engineering under Arctic Conditions (POAC), Trondheim.

Hanssen-Bauer, I., April 2016. Senior researcher at the Norwegian Meteorological Institute. Personal communication.

Hanssen-Bauer, I., Førland, E., Nordli, P. Ø., 1996. Measured and true precipitation at Svalbard. Norwegian Meteorological Institute Report number 31/1996.
URL http://met.no/filestore/31_96.pdf

Hosler, C. L., Jensen, D., Goldshlak, L., 1957. On the aggregation of ice crystals to form snow. Journal of Meteorology 14 (5), 415–420.

Hundecha, Y., St-Hilaire, A., Ouarda, T., El Adlouni, S., Gachon, P., 2008. A nonstationary extreme value analysis for the assessment of changes in extreme annual wind speed over the Gulf of St. Lawrence, Canada. Journal of Applied Meteorology and Climatology 47 (11), 2745–2759.

ISO 19906, 2010. Petroleums- og naturgassindustri - Arktiske offshorekonstruksjoner.

Johnsen, J. E., February 2016. Consultant at the Norwegian Meteorological Institute. Personal communication.

Katz, R. W., 2010. Statistics of extremes in climate change. Climatic Change 100 (1), 71–76.

Koutsoyiannis, D., 2004. Statistics of extremes and estimation of extreme rainfall: II. Empirical investigation of long rainfall records. Hydrological Sciences Journal 49 (4).

Kulyakhtin, A., 2014. Numerical modelling and experiments on sea spray icing. Ph.D. thesis, NTNU.

Kyle, H. L., Hurley, E. J., Ardanuy, P. E., 1985. The status of the nimbus-7 earth-radiation-budget data set. Bulletin of the American Meteorological Society 66 (11), 1378–1388.

Large, W., Pond, S., 1982. Sensible and latent heat flux measurements over the ocean. Journal of Physical Oceanography 12 (5), 464–482.

Lehning, M., Löwe, H., Ryser, M., Raderschall, N., 2008. Inhomogeneous precipitation distribution and snow transport in steep terrain. Water Resources Research 44 (7).

Li, L., Pomeroy, J. W., 1997. Estimates of threshold wind speeds for snow transport using meteorological data. Journal of Applied Meteorology 36 (3), 205–213.

Liston, G. E., Elder, K., 2006. A meteorological distribution system for high-resolution terrestrial modeling (micromet). Journal of Hydrometeorology 7 (2), 217–234.

Loeng, H., 1991. Features of the physical oceanographic conditions of the Barents Sea. Polar research 10 (1), 5–18.

Makkonen, L., 1989. Estimation of wet snow accretion on structures. Cold Regions Science and Technology 17 (1), 83–88.
URL http://www.sciencedirect.com/science/article/pii/S0165232X89800187

Makkonen, L., 2000. Models for the growth of rime, glaze, icicles and wet snow on structures. Philosophical Transactions of the Royal Society of London A: Mathematical, Physical and Engineering Sciences 358 (1776), 2913–2939.

Marty, C., Blanchet, J., 2012. Long-term changes in annual maximum snow depth and snowfall in Switzerland based on extreme value statistics. Climatic Change 111 (3-4), 705–721.

Maslowski, W., Marble, D., Walczowski, W., Schauer, U., Clement, J. L., Semtner, A. J., 2004. On climatological mass, heat, and salt transports through the Barents

Sea and Fram Strait from a pan-Arctic coupled ice-ocean model simulation. Journal of Geophysical Research: Oceans 109 (C3), n/a–n/a, c03032.
URL http://dx.doi.org/10.1029/2001JC001039

Matsuo, T., Sasyo, Y., Sato, T., 1981. Relationship between types of precipitation on the ground and surface meteorological elements. Journar of the Meteorological Society of Japan 59, 462–476.

Maykut, G. A., 1982. Large-scale heat exchange and ice production in the central Arctic. Journal of Geophysical Research: Oceans 87 (C10), 7971–7984.

Nakaya, U., Matsumoto, A., 1954. Simple experiment showing the existence of liquid water film on the ice surface. Journal of Colloid Science 9 (1), 41–49.

Nordli, P., Hanssen-Bauer, I., Førland, E., 1996. Homogeneity analyses of temperature and precipitation series from Svalbard and Jan Mayen. Vol. Report number 16/1996. Norske meteorologiske institutt.
URL http://met.no/filestore/16_96.pdf

NORSOK N-003, 2007. Actions and actions effects.

NPD, 2016. Nye ressurstall for Barentshavet sørøst og norsk havområde ved Jan Mayen. [Online; Accessed April 2016].
URL http://www.npd.no/Nyheter/Nyheter/2013/Nye-ressurstall-for-Barentshavet-sorost-og-Jan-Mayen/

NS-EN-1991-1-3, 2008. Eurokode 1: Laster på konstruksjoner - del 1-3: Allmenne laster - snølaster.

Nygaard, B. E. K., Seierstad, I. A., Veal, A. T., 2014. A new snow and ice load map for mechanical design of power lines in great britain. Cold Regions Science and Technology 108, 28–35.

Overland, J., Pease, C., Preisendorfer, R., Comiskey, A., 1986. Prediction of vessel icing. Journal of climate and applied meteorology 25 (12), 1793–1806.

Papalexiou, S. M., Koutsoyiannis, D., 2013. Battle of extreme value distributions: A global survey on extreme daily rainfall. Water Resources Research 49 (1), 187–201.

Parkinson, C. L., Washington, W. M., 1979. A large-scale numerical model of sea ice. Journal of Geophysical Research: Oceans 84 (C1), 311–337.

Pomeroy, J., Gray, D., 1990. Saltation of snow. Water resources research 26 (7), 1583–1594.

Reistad, M., Breivik, Ø., Haakenstad, H., Aarnes, O. J., Furevik, B. R., Bidlot, J.-R., 2011. A high-resolution hindcast of wind and waves for the North Sea, the Norwegian Sea, and the Barents Sea. Journal of Geophysical Research: Oceans (1978–2012) 116 (C5).
URL http://onlinelibrary.wiley.com/doi/10.1029/2010JC006402/full

Ryerson, C. C., 2011. Ice protection of offshore platforms. Cold Regions Science and Technology 65 (1), 97–110, anti-Icing and De-Icing Techniques.
URL http://www.sciencedirect.com/science/article/pii/S0165232X10000327

Sagerup, T., 2015. Snow modeling as tool for topside design. Tech. rep., Aker Solutions.

Serinaldi, F., Kilsby, C. G., 2014. Rainfall extremes: Toward reconciliation after the battle of distributions. Water resources research 50 (1), 336–352.

Serreze, M., Walsh, J., Chapin Iii, F., Osterkamp, T., Dyurgerov, M., Romanovsky, V., Oechel, W., Morison, J., Zhang, T., Barry, R., 2000. Observational evidence of recent change in the northern high-latitude environment. Climatic Change 46 (1-2), 159–207.

Serreze, M. C., Barry, R. G., 2005. The Arctic climate system. Vol. 22. Cambridge University Press.

Simonsen, K., Haugan, P. M., 1996. Heat budgets of the Arctic Mediterranean and sea surface heat flux parameterizations for the Nordic Seas. Journal of Geophysical Research: Oceans 101 (C3), 6553–6576.

Smedsrud, L. H., Esau, I., Ingvaldsen, R. B., Eldevik, T., Haugan, P. M., Li, C., Lien, V. S., Olsen, A., Omar, A. M., Otterå, O. H., et al., 2013. The role of the Barents Sea in the Arctic climate system. Reviews of Geophysics 51 (3), 415–449.

Smith, S. D., Katsaros, K. B., Oost, W. A., Mestayer, P. G., 1996. The impact of the hexos programme. In: Boundary-Layer Meteorology 25th Anniversary Volume, 1970–1995. Springer, pp. 121–141.

Steffensen, E., Nordli, P., Hanssen-Bauer, I., 1996. Stasjonshistorie for norske meteorologiske młinger i Arktisk. Tech. Rep. 17, Det Norske Meterologiske Institutt.

Sundsbø, P.-A., 1997. Numerical modelling and simulation of snow drift. Doctoral Dissertation Norwegian University of Science and Technology, Trondheim, Norway.

Syversen, T., Dinessen, F., Paaske, B. J., Ekeberg, O.-C., Hughes, N., Kråkenes, T., 2015. Kartlegging av is- og snøforekomst i Barentshavet, inkludert risikovurderinger relatert til petroleumsaktivitet. Tech. rep., Sintef.
URL http://www.ptil.no/getfile.php/PDF/Rapporter/102012290-00004%20Rapport%20sn%C3%B8%20og%20isforekomst%20321443_2_1.pdf

Tabler, R. D., 1991. Snow transport as a function of wind speed and height. In: Cold Regions Engineering. ASCE, pp. 729–738.

Tabler, R. D., 1994. Design guidelines for the control of blowing and drifting snow. No. SHRP-H-381. Strategic Highway Research Program, National Research Council.

Takeuchi, M., 1980. Vertical profile and horizontal increase of snow-drift. Journal of Glaciology 29, 481–492.

Teigen, S. H., Hansen, E. S., Roth, J. C., 2015. Marine icing severity in the Barents Sea. In: Proceedings of the International Conference on Port and Ocean Engineering under Arctic Conditions (POAC), Trondheim.

Thériault, J., Stewart, R., Milbrandt, J., Yau, M., 2006. On the simulation of winter precipitation types. Journal of Geophysical Research: Atmospheres 111 (D18).

Tominaga, Y., Okaze, T., Mochida, A., 2011. CFD modelling of snowdrift around a building: An overview of models and evaluation of a new approach. Building and environment 46 (4), 899–910.
URL http://www.sciencedirect.com/science/article/pii/S0360132310003124

Turner, J., Hosking, J. S., Phillips, T., Marshall, G. J., 2013. Temporal and spatial evolution of the Antarctic sea ice prior to the September 2012 record maximum extent. Geophysical Research Letters 40 (22), 5894–5898.

Vaudrey, K., 1987. 86 Ice Motion measurements in Camden Bay, AOGA Project 328, Vaudrey & Associates. Inc. San Luis Obispo, CA.

Wolff, M., Isaksen, K., Ødemark, K., Pettersen-Øverleif, A., Reitan, T., Brækkan, R., 2013. Vindkorreksjon av nedbør, et Energi Norge prosjekt. MET report 22/2013, Norwegian Meteorological Institute.

Appendices

A Algorithms to calculate time series of snow load

Figure A.1 and Figure A.2 show flowcharts of the algorithm used to estimate time series of snow load using the energy balance melt model and x-day snowfall model, respectively. The energy balance model is fairly simple. If the temperature is lower than 1.5 °C, the model will add precipitation as snow. Then the model estimates the melt rate according to Equation 3.2. The total amount of snow in the time step will then be $M^i \Delta t$, where Δt is the time step in seconds.

In the x-day snowfall model, we need to do a check if snow drift is turned on. If it is, we need to adjust the amount of precipitation to remove to compensate for snow which already has drifted off the platform. This is done by estimating drift from Equation 3.11, based on when snow is allowed to drift or not.

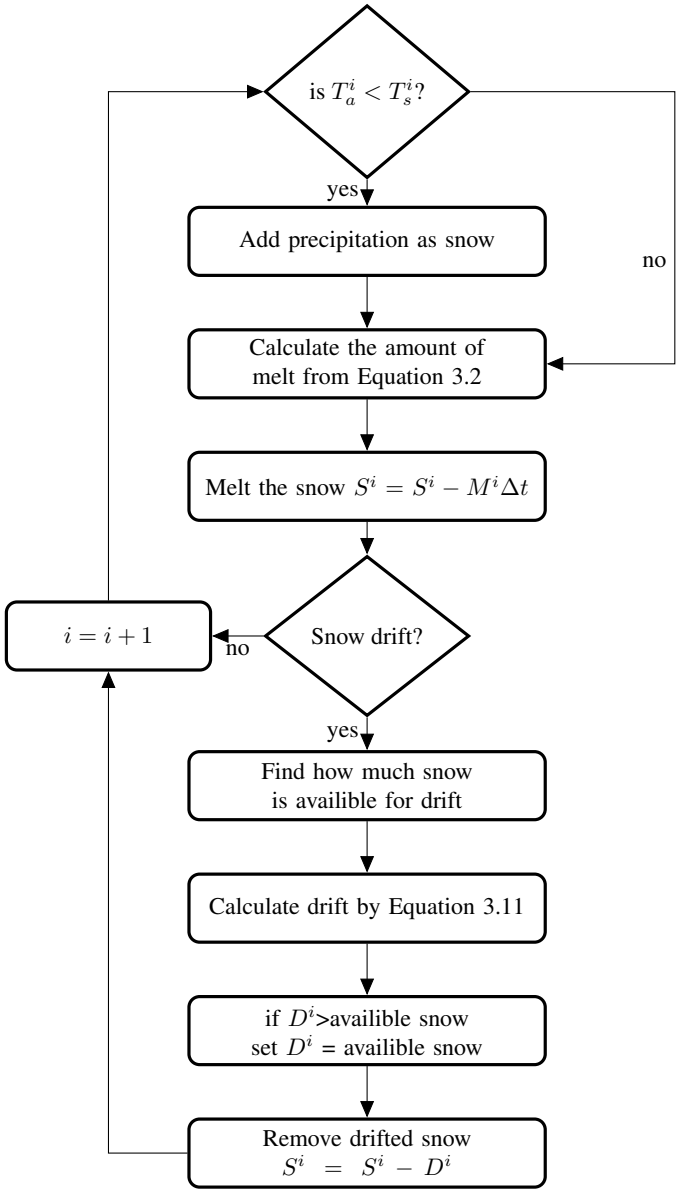

Figure A.1: Diagram showing the algorithm used to calculate snow loads when using the energy balance melt model. See the text for description of variable names.

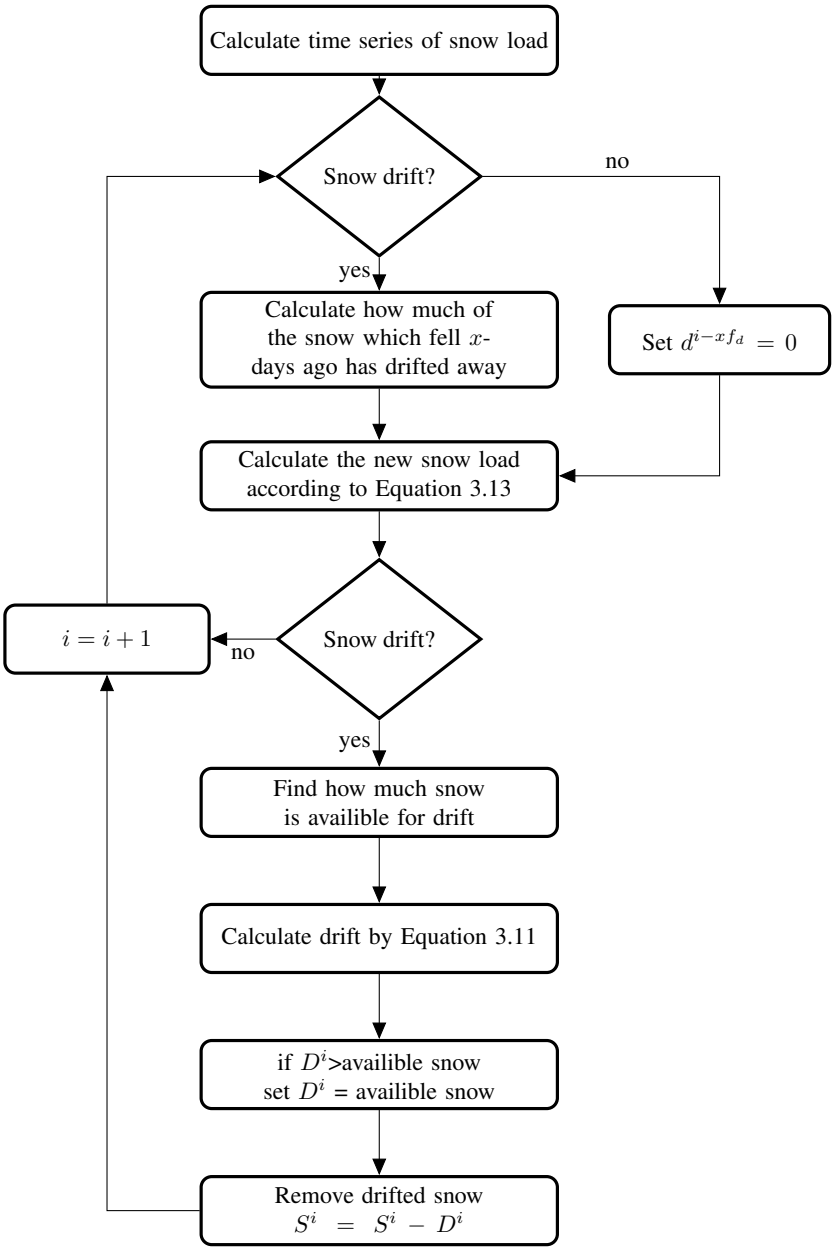

Figure A.2: Diagram showing the algorithm used to calculate snow loads using a x-day snowfall model. See the text for description of variables.

B A condition for wet snow accretion

When snow is falling when temperatures are higher than 0 °C, the snowflakes can be partially melted. This is characterized as wet snow, and can stick to vertical walls and surfaces and freeze to ice if air temperatures drops. Wet snow storms are often related to an unstable atmospheric boundary layer (Matsuo et al., 1981; Makkonen, 1989) with snow flakes falling from colder air masses at higher altitudes to a warmer layer near the earth's surface. The exact meteorological conditions suggested for wet snow vary in the literature, but based on theoretical considerations and available meteorological parameters, we use an energy balance method based on Makkonen (1989) to estimate when precipitation falls as wet snow. This study only aims to qualitatively investigate wet snow loads, and the extreme snow loads presented here should not be used as possible wet snow loads on vertical faces of structures without first doing a detailed study of aerodynamic effects, sticking efficiency, etc., of the structure in question.

Snow particles will only start melting if there is a heat flux to the snow's surface. Because snowflakes have a low termal inertia and so a positive heat flux will start melting promptly, this is also a sufficient requirement for wet snow (Makkonen, 1989).

Thus, snow will accrete on vertical surfaces as wet snow when the heat balance to the snow particle surface is positive. Using the parameterization in 3.2.2 we can easily calculate

$$Q = Q_{sh} + Q_{lo} + Q_{se} + Q_{la}, \tag{B.1}$$

with the parameters available in NORA10 and check if the heat flux is positive. During a snow storm, radiative heat fluxes are generally small, and if we assume they are negligible compared to the turbulent heat fluxes, the condition for wet snow is

$$Q_{la} + Q_{se} > 0. \tag{B.2}$$

If we assume the snow surface to have temperature 0 °C when melting and use the parameterization in Equation 3.6 and Equation 3.7, we can rewrite the condition to

$$T_a > \frac{0.622 L_w}{c_{p,air}} \left(\frac{611}{p - 231} - \frac{e(T_a)}{p - e(T_a)} \right), \tag{B.3}$$

where the atmospheric pressure p is in Pa. If we note that relative humidity is $rh = e(T_a)/e_s(T_a)$, where $e_s(T_a)$ is the saturated water vapor pressure at temperature T_a, and using appropriate values for the constants the equation becomes

$$T_a > 1.75 \times 10^3 \left(\frac{611}{p - 231} - rh \frac{e_s(T_a)}{p - 0.378 rh\, e_s(T_a)} \right). \tag{B.4}$$

This provides a simple conditions for wet snow based on air temperature and relative humidity. The relative variation of atmospheric pressure is so small that is has negligible effect. Equation B.4 shows that the lower the relative humidity, the higher the temperature at which wet snow can occur.

Using the condition for wet snow in Equation B.4, estimates for mean annual wet snow accumulation in the Barents Sea were calculated with data from NORA10. A contour plot of the annual wet snow is shown in Figure B.1. The annual wet snow is around 10 % compared to the annual accumulated snow of any type. The spatial variations are very similar to the variation in total annual snow. There is also a band of high annual wet snow stretching from the south cape of Spitsbergen to the east and south in the Barents Sea and another maximum off the west coast of Spitsbergen.

Interestingly, there is very little wet snow in the southeastern part of the Barents Sea. Wet snow forms when the temperature is between 0 °C and 1.5 °C with high enough relative humidity. Thus, there is only a narrow set of conditions for which wet snow can form. Southwest in the Barents Sea, the winter is relatively short and therefore there is less chance for the right conditions during a winter.

This is shown in Figure B.1 is the mean number of wet snow events every year. The area between Bjørnøya and Hopen sees the most frequent number of wet snow events, with between 27 to 30 events annually. There is a very high gradient southwest of Bjørnøya, and off the west coast of mainland Norway, south of 72° N there are less than 3 events annually. The spatial variability is very similar to the total annual wet snow accumulation. This shows that wet snow events are frequent in the southern Barents Sea, with over 9 events annually, and more frequent further north and east.

Time series of wet snow load was calculated by a 10-day wet snowfall model, and 100-year return level of wet snow load was calculated with the SGEV model (Figure B.2). The loads are aroun 10 kg/m^2 to 30 kg/m^2 in the area opened for petroleum activity in the Norwegian sector of the Barents Sea. There is a northeasterly gradient with the highest 100-year return values in the northeastern Barents Sea. This is in contrast to the extreme snow loads of any type of snow, which showed highest return levels further south.

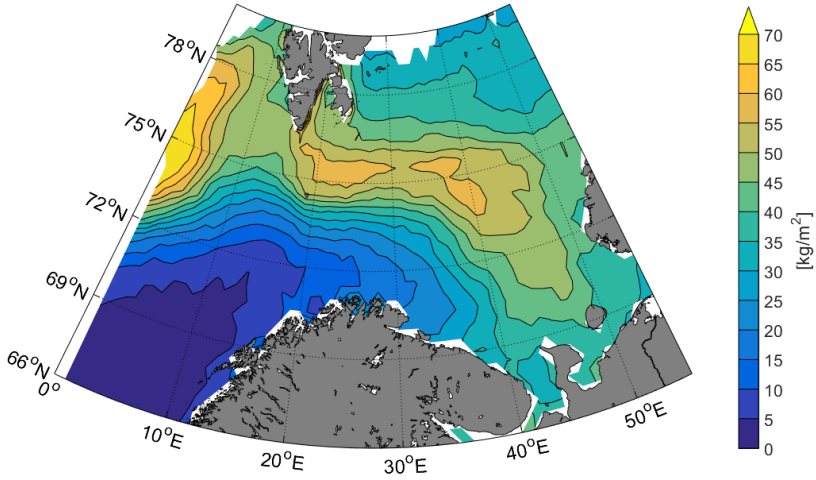

(a) Mean annual accumulated wet snow

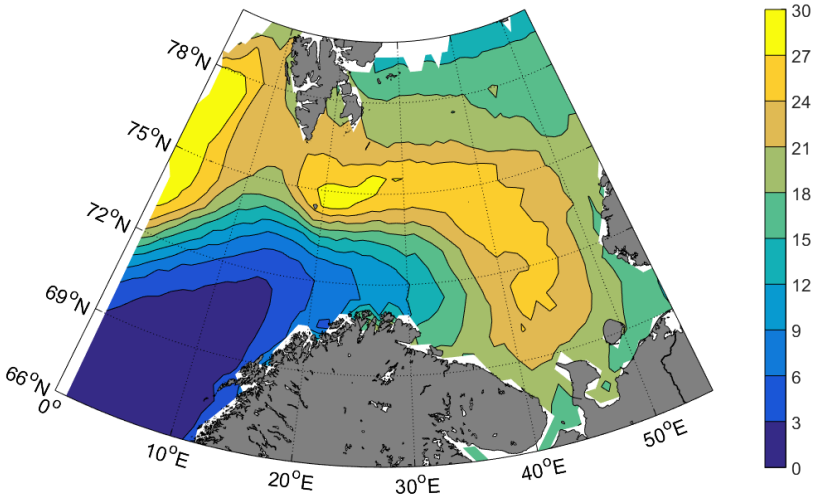

(b) Yearly number of wet snow events

Figure B.1: Mean annual accumulated wet snow (**a**) and mean number of wet snow events per year (**b**). Wet snow is characterized from Equation B.4 with NORA10 as input.

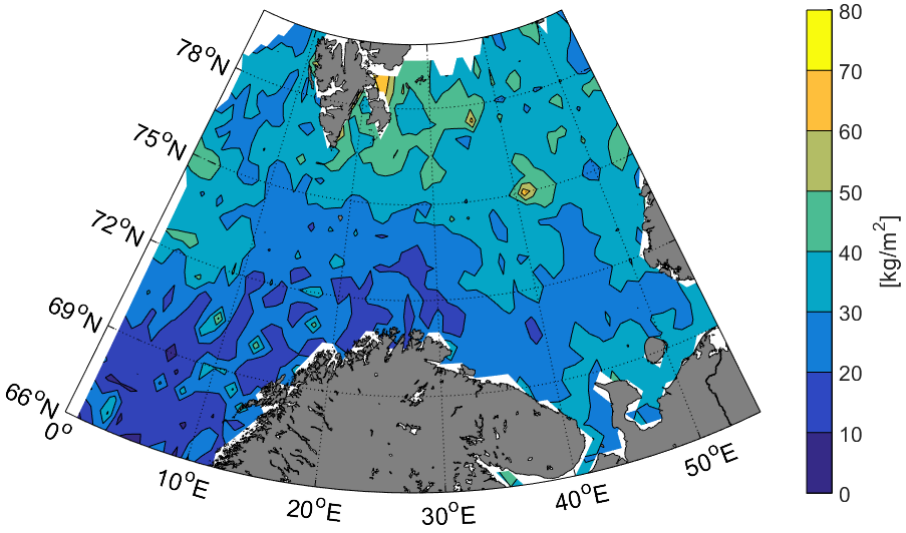

Figure B.2: 100-year values of wet snow load estimated with the SGEV model. Yearly maxima from a 10-day snowfall model for wet snow has been used as input to the SGEV model